AEDC-TR-79-63

C-2

Evaluation of Wind Tunnel Nozzle Afterbody Test Techniques Utilizing a Modern Twin Engine Fighter Geometry at Mach Numbers from 0.6 to 1.2

Ernest J. Lucas
ARO, Inc.

October 1980

Final Report for Period October 1975 through September 1979

Approved for public release; distribution unlimited.

ARNOLD ENGINEERING DEVELOPMENT CENTER
ARNOLD AIR FORCE STATION, TENNESSEE
AIR FORCE SYSTEMS COMMAND
UNITED STATES AIR FORCE

NOTICES

When U. S. Government drawings, specifications, or other data are used for any purpose other than a definitely related Government procurement operation, the Government thereby incurs no responsibility nor any obligation whatsoever, and the fact that the Government may have formulated, furnished, or in any way supplied the said drawings, specifications, or other data, is not to be regarded by implication or otherwise, or in any manner licensing the holder or any other person or corporation, or conveying any rights or permission to manufacture, use, or sell any patented invention that may in any way be related thereto.

Qualified users may obtain copies of this report from the Defense Technical Information Center.

References to named commercial products in this report are not to be considered in any sense as an indorsement of the product by the United States Air Force or the Government.

This report has been reviewed by the Office of Public Affairs (PA) and is releasable to the National Technical Information Service (NTIS). At NTIS, it will be available to the general public, including foreign nations.

APPROVAL STATEMENT

This report has been reviewed and approved.

Russell B. Sorrells III

RUSSELL B. SORRELLS, III
Project Manager
Directorate of Analysis and Evaluation

Approved for publication:

FOR THE COMMANDER

Elton R Thompson

ELTON R. THOMPSON
Acting Director of Analysis
and Evaluation
Deputy for Operations

REPORT DOCUMENTATION PAGE

READ INSTRUCTIONS BEFORE COMPLETING FORM

1 REPORT NUMBER: AEDC-TR-79-63

2 GOVT ACCESSION NO.

3 RECIPIENT'S CATALOG NUMBER

4 TITLE (and Subtitle): EVALUATION OF WIND TUNNEL NOZZLE AFTERBODY TEST TECHNIQUES UTILIZING A MODERN TWIN ENGINE FIGHTER GEOMETRY AT MACH NUMBERS FROM 0.6 TO 1.2

5 TYPE OF REPORT & PERIOD COVERED: Final Report - October 1975 - September 1979

6. PERFORMING ORG. REPORT NUMBER

7 AUTHOR(s): Ernest J. Lucas, ARO, Inc., a Sverdrup Corporation Company

8. CONTRACT OR GRANT NUMBER(s)

9 PERFORMING ORGANIZATION NAME AND ADDRESS
Arnold Engineering Development Center/DOA
Air Force Systems Command
Arnold Air Force Station, Tennessee 37389

10. PROGRAM ELEMENT, PROJECT, TASK AREA & WORK UNIT NUMBERS: Program Element 65807F

11 CONTROLLING OFFICE NAME AND ADDRESS
Arnold Engineering Development Center/DOS
Air Force Systems Command
Arnold Air Force Station, Tennessee 37389

12. REPORT DATE: October 1980

13 NUMBER OF PAGES: 121

14 MONITORING AGENCY NAME & ADDRESS(If different from Controlling Office)

15. SECURITY CLASS (of this report): UNCLASSIFIED

15a DECLASSIFICATION DOWNGRADING SCHEDULE: N/A

16 DISTRIBUTION STATEMENT (of this Report)

Approved for public release; distribution unlimited.

17 DISTRIBUTION STATEMENT (of the abstract entered in Block 20, if different from Report)

18 SUPPLEMENTARY NOTES

Available in Defense Technical Information Center (DTIC)

19 KEY WORDS (Continue on reverse side if necessary and identify by block number)

test methods	exhaust nozzles	flight tests
scale models	plumes	
pressure	simulation	
Reynolds number	transonic flow	
YF-17 aircraft	wind tunnel tests	

20 ABSTRACT (Continue on reverse side if necessary and identify by block number)

Analyses of surface pressure data from wind tunnel tests conducted in the Propulsion Wind Tunnel (16T) on the 0.1- and 0.2-scale models of the YF-17 aircraft and flight tests conducted at the NASA Dryden Flight Research Center with the prototype YF-17 were conducted to substantiate the effectiveness of the subscale wind tunnel test techniques currently used at AEDC to provide data to evaluate throttle-dependent effects. The data were obtained at Mach numbers 0.6, 0.9, and 1.2 at characteristic Reynolds numbers based on fuselage length from 14 x 10^6

DD FORM 1 JAN 73 1473 EDITION OF 1 NOV 65 IS OBSOLETE

20. ABSTRACT (Continued)

to 250 x 10^6. The data obtained at Mach numbers 0.6 and 0.9 indicate that valid techniques are available to obtain subscale wind tunnel data that are directly applicable to aft-end throttle-dependent flight performance prediction. The wind tunnel plume simulation techniques, however, do not provide data for directly predicting the flight vehicle, aft-end, calculated loads at Mach number 1.2. Additional corrections must be applied to the data to compensate for temperature effects associated with afterburning operations, such as that encountered at Mach 1.2.

AFSC
Arnold AFS Tenn

PREFACE

The work reported herein was conducted by the Arnold Engineering Development Center (AEDC), Air Force Systems Command (AFSC), for the Directorate of Analysis and Evaluation (AEDC/DOA) and the Aerospace Propulsion Laboratory, Wright-Patterson Air Force Base, Ohio. The results presented were obtained by ARO, Inc., AEDC Group (a Sverdrup Corporation Company), contract operator of AEDC, AFSC, Arnold Air Force Station, Tennessee. Russell B. Sorrells III was the AEDC project manager for this portion of the program. The work was accomplished under ARO Project Number P43T-06A, and the manuscript was submitted for publication on August 3, 1979.

CONTENTS

ILLUSTRATIONS

Figure Page

Figure | Page

Figure Page

TABLES

APPENDIX

1.0 INTRODUCTION

Subscale design studies, configuration optimization, and, at times, competitive selections are conducted in wind tunnels. In recent years, problems have been encountered in achieving the predicted performance of high-performance aircraft. Since thrust loading for aircraft systems has been steadily increasing, the source of the problem often has been the inability to predict airframe propulsion system interaction effects that are becoming more significant with each new system.

As shown in Refs. 1 and 2, the accurate prediction of full-scale afterbody drag from scale-model wind tunnel test data has been considered (pro and con) to be limited by the inability to achieve full-scale Reynolds numbers in the wind tunnel tests. For economic reasons, the models are generally sized for tests in smaller wind tunnels and are thus smaller in scale than necessary for testing in Propulsion Wind Tunnel (16T) (Ref. 3). Current fighter aircraft models used for most wind tunnel testing are usually one-twentieth to one-tenth and ocassionally two-tenths scale. Limited wind tunnel capability precludes matching the flight environment characteristic Reynolds number (the currently accepted parameter for boundary-layer simulation) when using the smaller models. The use of larger scale models to increase the characteristic Reynolds number causes intolerable interference to be introduced into transonic wind tunnel results. The model contours are eventually scaled to proposed prototype or actual production contours of the full-scale vehicle and, because of many factors, duplication of the model contours is not always accomplished in the full-scale vehicle. Thus, both the Reynolds number and model simulation differences can affect the correlation of wind tunnel and flight data.

The analysis reported herein was conducted to investigate the test techniques currently used to obtain subscale nozzle-afterbody data at the AEDC test facilities. The 0.1- and 0.2-scale models of the YF-17 (Refs. 4 and 5) and one of the full-scale prototype flight aircraft (Ref. 6) were used to obtain the surface pressure data used in this investigation. The main objective of the effort was to substantiate the validity of external surface pressure measurements obtained on the nozzle and afterbody of the subscale models as predictors for the similarly located pressures on the flight vehicle. Approximately 200 surface pressure orifices were installed on the left side of the twin engine 0.1- and 0.2-scale models. Data from the 0.1-scale model tests were used to locate the approximately 70 orifices on the flight vehicle.

The 0.1-scale model, when tested at the upper wind tunnel Reynolds number limit (Ref. 3), simulated only one-half of the full-scale flight vehicle characteristic Reynolds number at the upper altitudes, for the related flight test (Ref. 6). The 0.2-scale model was built

specifically to provide data at the flight Reynolds number and to provide a direct comparison of the pressure data between the wind tunnel and flight programs.

The model results were obtained during wind tunnel tests in the Tunnel 16T (Ref. 3) at Mach numbers from 0.6 to 1.2 at various model attitudes with a cold jet simulation (T_{jet} = T_{amb} ~ 560°R) of the jet exhaust. The flight test program (Ref. 6) was accomplished at Edwards Air Force Base through the cooperation of several governmental agencies and industries. Data for this program were obtained at Mach numbers from 0.6 to 1.2 at altitudes up to 50,000 ft at various load factors necessary to maintain constant aircraft pitch attitudes during Reynolds number excursions.

2.0 TECHNIQUES AND FACILITIES

2.1 WIND TUNNEL

2.1.1 Test Techniques

The basic accounting system used by industry applies to the airframe certain drag values that are obtained during tests conducted with an aerodynamic model with, at best, a flow-through inlet and altered nozzle exhuaust region. Throttle-dependent drag increments correcting for inlet spillage, nozzle closure, and jet plume effects are then estimated from previous experience or defined from tests of an inlet drag model and nozzle-afterbody models.

The present investigation addresses the nozzle afterbody test techniques. Since surface pressure data could be obtained on both the models and the flight vehicle, agreement between the pressure data was selected to define the effectiveness of the current wind tunnel test techniques.

The engine exhaust jet plume was simulated with high-pressure air at ambient temperature (~560°R) ducted through the model supports to the nozzles. Interchangeable nozzles representative of various power settings were used to define the effect of nozzle closure. The engine inlet ducts were sealed. The models were supported by systems that allowed unobstructed jet exhaust simulation. Corrective increments obtained for the support system interference during the previous investigations (Refs. 4 and 5) were applied to the data for the wind tunnel to flight comparisons in this report.

Also investigated was a recently developed technique (Ref. 7) using a sting support with the jet exhaust simulated by an annular jet. This technique allows comparisons to flight without support system corrections.

2.1.2 Facility

Tunnel 16T is a variable-density, continuous-flow tunnel capable of being operated at Mach numbers from 0.20 to 1.60 and stagnation pressures from 120 to 4,000 psfa. The maximum attainable Mach number can vary slightly depending upon the tunnel stagnation pressure ratio requirements with a particular test installation. The maximum stagnation pressure attainable is a function of Mach number and available electrical power. The tunnel stagnation temperature can be varied from about 80 to 160°F depending upon the available cooling-water temperature. The test section is 16 ft square by 40 ft long and is enclosed by 60-deg inclined-hole perforated walls of six-percent porosity. Additional information about the tunnel, its capabilities, and operating characteristics is presented in Ref. 3.

2.1.3 Instrumentation

Model surface pressures were measured with six multiport scanning valves employing 15-psid transducers. The 48 port valves were controlled by a facility computer in a step-pause mode to monitor each pressure to ensure stabilization before advancing to the next port. Jet exhaust flow conditions were monitored by internal duct pressure and temperature rakes.

The model roll and yaw angles were set to zero and were not varied during the wind tunnel tests. The model pitch attitude was obtained with a model-mounted angular position indicator.

2.1.4 Data Acquisition and Reduction Technique

Model surface pressure data were obtained on the 0.1-and 0.2-scale models of the YF-17 aircraft within the Mach number range from 0.6 to 1.2. The data were obtained on several configurations during a multiphase program discussed in Refs. 4 and 5. Surface pressure coefficients were calculated using the free-stream static and dynamic pressures. The nozzle and afterbody integrated pressure loads were calculated by summing the product of the local pressures and the incremental axial and normal projected areas, A_i, assigned to each pressure. The loads were converted to coefficient form based on the wing-fuselage planform area ($S = 350$ ft^2 full scale) and the dynamic pressure. Empennage loads were not included in the calculated loads since pressure instrumentation was not included on the tail surfaces. However, the horizontal and vertical tails were on the models throughout the investigations, thus influencing the measured surface pressures and resultant integrated-pressure loads.

Each model configuration was assembled and the surface pressures leak checked immediately before testing. Data were then obtained at various model-pitch attitudes or nozzle pressure ratios (NPR).

Wing-tip support system interference corrections were defined from data obtained by testing the sting-supported 0.1-scale model with and without the simulated wing-tip supports and with both the simulated wing-tip and horizontal blade supports on the 0.2-scale model. The support interference effects are documented in Refs. 4 and 5. A support interference increment was documented for each orifice, and the integrated values from the two configurations used to determine the interferences were subtracted to determine the overall effect. All the support interference was documented at the nominal test unit Reynolds number of 2.8×10^6/ft within the angle-of-attack range of 0 to 4 deg.

2.2 FLIGHT TEST PROCEDURES

The flight test program (Ref. 6) was conducted with the YF-17 prototype aircraft at Edwards Air Force Base, California. The test matrix was established to provide Reynolds number effects at fixed vehicle angles of attack. The high-altitude level flight ($G_1 = 1.0$) points were obtained first to determine the trim angle of attack for that altitude and vehicle weight. Flight vehicle load factors for Reynolds number excursions at the same angle of attack were then calculated from $G_2/G_1 = (W_1/W_2)/(Q_2/Q_1)$, where G_2 is the load factor for a constant altitude turn to match the pre-established angle of attack (lift coefficient), Q is the dynamic pressure based on the Mach number and the pressure altitude, H, and W is the instantaneous vehicle weight. The aircraft was trimmed in either level flight or a steady-state turn and 30 sec were allowed for systems and surface pressure to stabilize. The data system was then activated and multiple scans of the data taken. Data were obtained at conditions listed in Table 1.

3.0 TEST VEHICLES

The two wind tunnel models shown in Figs. 1 and 2 were scale versions of the prototype YF-17 design. The left-side nacelle and nozzle outer surface of each model was instrumented with approximately 200 surface pressure orifices, as illustrated in Fig. 3. The orifice locations and further model descriptions are presented in the wind tunnel test reports (Refs. 4 and 5). The "as built" surface contours in the vicinity of the nacelle orifices were defined for axial stations indicated in Fig. 4 for the 0.2-scale model and the coordinates are recorded in Table 2. The contours are included herein so that comparison with the actual aircraft contours would be possible when the flight vehicle information is available.

The flight vehicle shown in Fig. 5 was one of two prototype YF-17 aircraft built for the Air Force lightweight fighter competition. The left-side nozzle and nacelle outer skin was instrumented with approximately 70 pressure orifices (see Figs. 6 and 7) at locations selected from the 0.1-scale wind tunnel test results. Several orifice locations on the flight vehicle were in the vicinity of protuberances not simulated on the wind tunnel models, particularly on the bottom nacelle centerline (ϕ = 180 deg). A more detailed description of the aircraft and instrumentation can be found in Ref. 6.

4.0 UNCERTAINTY OF MEASUREMENT

Uncertainties (combination of systematic and random errors) of the basic tunnel parameters, shown in Fig. 8, were estimated from repeat calibrations of the instrumentation and from the repeatability and uniformity of the test section flow during tunnel calibration. Uncertainties in the instrumentation system were estimated from repeat calibration of the systems against secondary standards whose uncertainties are traceable to the National Bureau of Standards calibration equipment. The instrument uncertainties were combined using the Taylor series method of error propagation described in Ref. 8 to determine the pressure coefficient uncertainties at the typical test conditions shown in Table 4. Typical wind tunnel data repeatability is on the order of $\Delta CP \sim \pm 0.005$ as reported in Ref. 5.

The uncertainties of the flight Mach number, altitude, and attitude were determined from repeat airspeed calibration flights and calibration of the onboard instrumentation, as indicated in Ref. 6. The flight vehicle surface pressures were recorded on appropriate transducers with a multiport motor-driven scanning valve located in the engine bay compartment. The transducers were calibrated for variations in the local environment. The reference pressure was applied to both sides of the system to check the transducer zero on each data scan. Check calibrations were made during the test program to verify the transducer sensitivity. The uncertainty for the flight pressure data from Ref. 6 is also presented in Table 4.

5.0 RESULTS AND DISCUSSION

Data have been compiled from wind tunnel investigations of the 0.1- and 0.2-scale models of the YF-17 and flight tests of the full-scale prototype aircraft. The data are used in this report to define the adequacy of the current wind tunnel test techniques used to provide information for prediction of the throttle-dependent effects on afterbody forces.

5.1 MODEL SCALE, REYNOLDS NUMBER EFFECTS

The ability to accurately predict flight performance from scale model wind tunnel test data is the requirement of many subscale investigations. Performance data are generally obtained with models of the size of the 0.1-scale model used in this program. However, previous investigators have observed large differences in pressure drag between wind tunnel and flight measurements that, at times, were attributed to a Reynolds number effect. The 0.2-scale model was tested to provide further information on Reynolds number effects in the range between the 0.1- and full-scale configurations.

Data are presented in Fig. 9 for the 0.1- and 0.2-scale cruise (A8 = 200 in.^{2}) and reheat (A8 ~ 300 in.^{2}) nozzle configurations at Mach numbers 0.6, 0.9, and 1.2. The cruise nozzle configuration (Fig. 9a) is typical for Mach number 0.6 and 0.9 operations, and the reheat nozzle (Fig. 9b) is generally applicable for Mach number 1.2 operation. The region of disagreement in the data for the two wind tunnel models is most evident at Mach number 1.2 with the cruise nozzle configuration since the integrated-pressure loads are larger at this condition. In terms of percent of drag, however, the data differences are approximately the same as those for the cruise nozzle configuration at all three Mach numbers (approximately 10 percent). Differences in the attachment of the wing-tip supports to the tunnel support could produce some of the data differences shown at subsonic conditions. The 0.1-scale model had the "V" support strut (Fig. 1a) in the jet exhaust region, whereas the 0.2-scale model attachment was through a horizontal blade below the jet centerline (Fig. 2a). The blade effect ($\Delta CA \sim 0.0005$ at subsonic Mach numbers) was documented during the 0.2-scale test, and results are presented in Ref. 5.

The results of previous investigations (Ref. 9) have indicated that blockage effects for the 0.2-scale model should not be measurable except very near Mach number 1.0. The reheat nozzle configuration (Fig. 9b) does not indicate the large difference in axial force at Mach number 1.2 that was measured on the cruise configuration. Thus, one would surmise that the data differences are related to a local flow phenomenon associated with the larger expansion over the cruise nozzle ($X/L \gtrsim 0.97$) or to a difference in contour between the 0.1- and 0.2-scale model nozzles.

Pressure data from the 0.1- and 0.2-scale models at nearly matching characteristic Reynolds numbers are presented in Figs. 10 through 14. Agreement between pressure distributions from the two scale models is generally within the data repeatability over the aft end of the vehicles at Mach numbers 0.6 and 0.9. Some differences are evident along the top centerline of the nacelle ($\phi = 0$), particularly on the nozzle at Mach number 0.6 and the nacelle at Mach number 0.9. In addition, the 0.1-scale model had a surface gap at $X/L \sim 0.8$ caused by a metric break associated with its use as a force model, whereas the 0.2-scale model only had a joint line where the afterbody attached to the main forebody support. The

differences in the surface pressure data in the vicinity of the X/L ~ 0.8 probably result from mismatches in model geometry between the two scale models.

The pressure data from the cruise nozzle (A8 ~ 200 in.^{2}) configuration at Mach number 1.2 (Fig. 12) indicate the same differences shown by the integrated loads. The recompression shock or separation location has shifted one orifice location further downstream on the 0.2-scale model nozzle (Fig. 12b), which could possibly have been the result of a slight mismatch in characteristic Reynolds number (Re_ℓ) imposed by aerodynamic loading restrictions. The 0.1-scale model data shown at Mach number 1.2 are similar to the lower Reynolds number data on the 0.2-scale model also included in Fig. 12b. Thus, the differences on the cruise nozzle configuration at Mach number 1.2 were probably caused by the sensitivity of the recompression shock location to Reynolds number variation at the lower Reynolds numbers.

The effect of varying the characteristic Reynolds number by varying the unit Reynolds number from approximately 1.4 x 10^6/ft to 5.6 x 10^6/ft is shown in Figs. 15 through 18 and 19 through 22 for the 0.1- and 0.2-scale models, respectively. The 0.1-scale model local surface pressure distributions are relatively insensitive to changes in Reynolds number. The integrated axial-force coefficients (tabulated in the figure headings) indicated a small change at the lower wind tunnel Reynolds number. However, the differences in the integrated axial force are within the data repeatability of approximately ±0.0003 (three counts). Similar effects are evident in the 0.2-scale data (Figs. 19 through 22) with even larger differences for the low Reynolds number at Mach number 1.2.

Data from Reynolds number variations in flight are presented in Figs. 23 through 25 for Mach numbers 0.6 and 0.9. Although the averaged aircraft attitude, α, was not constant, the variations in the local surface pressure coefficients with characteristic Reynolds number are within the flight data uncertainty at Mach number 0.6. Similar results are evident at the low angles of attack at Mach number 0.9 (Fig. 24). Larger data differences are noted at the higher aircraft attitude at Mach number 0.9 (Fig. 25). Even so, the flight data generally fall within the scatter of the two sets of repeat flight data (Re_ℓ ~ 72 x 10^6) for both the local pressure coefficients and the integrated axial-force coefficients (tabulated in the figure headings). There is little Reynolds number effect on the aft-end pressures or axial loadings, at least for the A8 = 200-in.^{2} configuration. Thus, for each of the 0.1-, 0.2-, and full-scale configurations there are only localized and apparently unrelated effects of characteristic Reynolds numbers at Mach numbers 0.6 and 0.9.

5.2 WIND TUNNEL TO FLIGHT COMPARISON

Because of the limited pressure instrumentation on the flight vehicle it was necessary to integrate flight test pressure data with different orifice-area assignments than were used with

the wind tunnel models. In order to ensure that the flight pressure area integration would provide the same results as the wind tunnel data integrations, the wind tunnel data were integrated using 200 orifices and reintegrating using the wind tunnel data from the 70 orifices at flight locations. As shown in Figs. 26 and 27, the distribution of the axial projected areas corresponding to the limited flight orifices is satisfactory since the differences between the two integrations are within the data repeatability of $\Delta CA = \pm 0.0003$. Thus, the assessment of differences between the wind tunnel data based on the integration of 200 orifices and the flight data based on the integration of only 70 orifices can be made. The area assignments for the pressure integrations of the wind tunnel data are given in Refs. 4 and 5 and in Table 3 for the flight vehicle.

The data obtained on the 0.1- and 0.2-scale models at various Reynolds numbers were acquired with the wing-tip supports for unobstructed jet exhaust simulation. The wind tunnel data were acquired at model attitudes as close to the flight vehicle trim attitudes as possible and have been corrected for support system interference. Both sets of corrected wind tunnel data are shown in Fig. 28 as a function of Reynolds number. The difference between the data from the two scale models at Mach number 0.6 could still be caused by support system interference effects since the horizontal support blade simulation for the 0.2-scale model (Ref. 5) was more prominent at subsonic Mach numbers. At Mach number 0.9 the scatter within each data set is generally within the uncertainty band except at the lowest Reynolds number. It must be noted that for Mach number 0.9 both sets of wind tunnel data were corrected for support system interference using the 0.2-scale data, since insufficient 0.1-scale results were available to determine the effect of the support system on the A8 ~ 200-in.^{2} nozzle data. With the corrections applied, the wind tunnel data at characteristic Reynolds numbers above 30×10^6 agree well with the flight data, which show no appreciable variation with Reynolds number.

Flight data could not be obtained at Mach number 1.2 with the A8 ~ 200-in.^{2} nozzle. Several flight data sets were obtained, however, with the A8 ~ 300-in.^{2} nozzle configuration and are compared to the appropriate wind tunnel data in Fig. 28c. The flight data indicate an appreciable effect of Reynolds number on the integrated axial force. However, examination of the nozzle and afterbody component loads (Fig. 29) indicate that the major part of the apparent Reynolds number sensitivity comes from the nozzle. In addition, the flight vehicle was operating at an NPR above the design value for which the wind tunnel data are presented. Figure 30 shows that in contrast to the data at subsonic Mach numbers the data at Mach number 1.2 are not only very sensitive to NPR but the flight data drag are considerably lower than the wind tunnel data. As shown by Peters (Ref. 10), when the shape-related parameter (NPR) is matched between a hot and cold jet, the different entrainment effects produce a conservative (higher) drag for the cold jet simulation. Thus, the combination of higher NPR and the higher jet exhaust temperature for the afterburning (A8 ~ 300-in.^{2}) flight vehicle causes the flight axial-force coefficient to be lower than that measured in the wind tunnel.

The surface pressure data at the same characteristic Reynolds number and Mach numbers 0.6 and 0.9 are presented in Figs. 31 through 37. The wind tunnel data were obtained with the wing-tip-supported 0.1- and 0.2-scale models and have been interpolated to the flight attitude, α, NPR, and δ_H conditions by procedures outlined in Appendix A. Support system interference corrections previously discussed have also been applied. It should be noted that the orifice-to-orifice "straightline" fairing is included for symbol continuity. The fairing does not follow the actual pressure distribution and often misses the maximum or minimum pressure value because of the limited number of orifices.

The surface pressure variations are similar for all data sets. Areas of significant differences are evident over the nozzle external expansion region (X/L ~ 0.97) and the recompression region between the nozzles (ϕ = 45 and 135 deg). The effect of the engine-bay purge exhaust flow was shown in Refs. 4 and 5 to influence local pressures in the vicinity of the exhaust exits (X/L ~ 0.94, ϕ = 0 and 180 deg on both nacelles) and the ϕ = 45- and 135-deg pressure rows in the nacelle trough. The 0.1-scale data shown in this report do not include the bay-purge effect since only limited bay-purge data were obtained during the wind tunnel test of the 0.1-scale model. The 0.2-scale model simulation was accomplished with an inlet bleed duct and open (top and bottom) flowthrough duct at the bay-purge location. An example of 0.2-scale bay-purge exhaust simulation effect is shown in Fig. 38. The differences between wind tunnel and flight data in the area of the auxiliary exhaust indicate the need for proper simulation of such devices during wind tunnel testing.

The metric break on the modified 0.1-scale model and the afterbody connection joint on the 0.2-scale models were located at X/L ~ 0.8 and probably produced the differences between scale models and the flight vehicle at this axial location. The horizontal tail extends from X/L ~ 0.86 to X/L ~ 0.97. Interpolation of the pressure data to the flight tail angle setting for the 0.1- and 0.2-scale full-jet wind tunnel data would affect the pressures within this region on the outboard rows of orifices (ϕ = 225 and 315 deg). Data at characteristic Reynolds numbers that matched flight data could not be obtained in the wind tunnel at Mach number 1.2. Nevertheless, a comparison of the wind tunnel to flight data is presented in Fig. 40 to illustrate the agreement of the pressure data. The wind tunnel data indicate that the flow over the wind tunnel model nozzle expands more than in flight and recompresses to a lower value at the nozzle exit. This effect is also consistent with the effects of the cold jet exhaust simulation discussed previously.

5.3 ANNULAR-JET PLUME SIMULATION

The annular-jet techniques for afterbody testing, refined by Price (Ref. 7), simulate the full-jet plume by exhausting air at ambient temperature (T_{TJ} ~ 560°R) through the annulus

between an enlarged nozzle throat and a solid support sting (Fig. 2d). The annular-jet nozzle pressure ratio required to yield the same plume diameter as a full jet is generally larger than that of the full jet. The data are presented as a function of the equivalent NPR (Ref. 7) of the full-jet condition being simulated. The advantage of the annular-jet technique is that the wind tunnel data can be obtained with the effects of the sting support system moderated by the exhaust plume. External model contours can also be more easily simulated since support attachment is through the nozzle exits. The 0.2-scale model was tested using this technique to provide the most realistic comparison with flight data.

The bay-purge exhaust was also simulated by flowthrough passages, top to bottom, which was the most realistic simulation for this model.

The integrated axial loads on the afterbody and nozzle are compared to the flight data in Fig. 41 as a function of aircraft attitude. Previous analysis has indicated the data are insensitive to Reynolds number. The wind tunnel data were obtained at the maximum possible characteristic Reynolds number ($Re_f \sim 26 \times 10^6$) for the 0.2-scale model with the small-sting supports required for annular-jet flows. The flight data were obtained at Re_f from $\sim 60 \times 10^6$ to 240×10^6. The agreement between the 0.2-scale annular-jet wind tunnel and flight integrated-loads data is within the wind tunnel data uncertainty at Mach numbers 0.6 and 0.9. The axial force on the nozzle at Mach number 1.2 with the reheat nozzle (A8 ~ 300 in.^{2}), however, is consistently lower in flight than in the wind tunnel (Fig. 41d), whereas the afterbody loading is generally within the uncertainty band for all flight angles of attack and nozzle pressure ratios. The loads on the nozzle portion of the vehicle have been shown to be very sensitive to NPR at the supersonic flow conditions (Fig. 30c and Ref. 5). The wind tunnel nozzle axial loading is also more conservative (higher) than the flight results when compared as a function of the annular-jet equivalent NPR (Fig. 42). Correct simulation of the jet plume seems to be the critical simulation item since the differences between the flight vehicle and 0.2-scale annular-jet axial loadings occur primarily on the nozzle. Although the cold ($TT_j \sim 560°R$) annular jet apparently produced a nearly correct flow-field simulation at Mach numbers 0.6 and 0.9 where the flight jet exhaust is cooler ($TT_j \sim 1{,}400°R$) because of no afterburning, it is probable that improper entrainment resulted in the wind tunnel at Mach number 1.2 because of the inability of the cold jet to simulate the afterburning jet exhaust of the flight vehicle. Either a different cold annular-jet simulation parameter must be used or the effects of hot jet exhaust included for complete jet effect simulation at afterburning conditions.

Typical comparisons of the pressure distributions from wind tunnel annular jet and flight are presented in Figs. 43 through 45 for the same conditions at which the full-jet data comparisons were made. The pressure distributions on the afterbody and nozzle agree

within the data repeatability except in the trough region between the nozzles (ϕ = 45 and 135 deg) where the wind tunnel data at the nozzle exit indicate more separated flow and lower pressure recovery caused by the incomplete simulation of the bay-purge exhaust flow in the wind tunnel. At Mach number 1.2 (Fig. 45) the 0.2-scale surface pressures consistently show less recovery on the nozzle exit, probably as a result of improper jet entrainment simulation previously discussed.

With the annular-jet plume simulation and the relative insensitivity of the current test article to Reynolds number at subsonic speeds, the wind tunnel data acquired with the present test techniques provide a sound base to predict full-scale aircraft loads or throttle-dependent effects. There still exist conditions at which the annular-jet technique may not be applicable, e.g., nonaxisymmetric, thrust vectoring and variable plug nozzle designs. For these configurations, the full-flowing cold jet simulation technique with appropriate support system interference corrections should provide data representative of flight.

Comparisons of typical differences between the wind tunnel and flight pressure distributions for both the annular and corrected full-jet wind tunnel configurations are presented in Fig. 46 for Mach numbers 0.6, 0.9, and 1.2. Although pressure data obtained with the annular jet are closer to the flight results, the integrated force coefficients (tabulated at the top of each figure) of both wind tunnel methods agree within the data uncertainty at Mach numbers 0.6 and 0.9. The pressure differences between both sets of wind tunnel and flight data are larger at Mach number 1.2; but the annular-jet integrated axial loads are somewhat closer to the flight results, indicating that additional support system corrections may be needed at Mach number 1.2 for wing-tip-supported models.

6.0 CONCLUDING REMARKS

An investigation was conducted with the 0.1- and 0.2-scale wind tunnel models and the YF-17 flight vehicle to define the adequacy of the current subscale test techniques used at AEDC to provide data to evaluate throttle-dependent effects on afterbody forces. The surface pressure data were acquired at Mach numbers 0.6, 0.9, and 1.2 for several afterbody configurations corresponding to various throttle settings. The analysis of the wind tunnel and flight data indicated:

1. Subscale wind tunnel test techniques are adequate to provide reliable data for predictions of nozzle afterbody, throttle-dependent axial forces at Mach numbers 0.6 and 0.9. However, support system interference corrections must be defined and applied.

2. Both the full- and annular-jet plume simulations are valid at Mach numbers 0.6 and 0.9 for the nonafterburning nozzle configurations. However, hot jet effects (entrainment) must be included for the afterburning configurations at Mach number 1.2 to obtain valid wind tunnel-to-flight comparisons.

3. No appreciable Reynolds number effect was evident in the pressure or axial-force data at Mach numbers 0.6 and 0.9 over the Reynolds number range from 9 to 30 x 10^6, 15 to 60 x 10^6, and 50 to 250 x 10^6 for the 0.1-scale, 0.2-scale, and full-scale test vehicles, respectively.

4. The vehicle auxiliary exhaust or purge flows should be simulated during wind tunnel testing if local flow conditions are of interest.

7.0 RECOMMENDATIONS

As a result of the analyses performed during this investigation, the following recommendations are made relative to nozzle afterbody type test:

- The current Mach number 1.2 investigations indicate that correlation between wind tunnel and flight would be improved with hot jet effects included. Test techniques are needed to allow simulation or correction to a hot jet exhaust when jet exhaust tempertures are significant.

- The effects of the engine installation can be defined with a sufficient number of surface pressure orifices on the nozzle region of a model.

- When balances are used for engine installation effect definition, surface pressures should also be measured to verify the balance data by a comparison with the pressure times integrated forces.

- Results from this type of wind tunnel test can be configuration dependent. Thus, both the effect of Reynolds number and support system interference should be incorporated into the test schedule for early definition.

- Care should be exercised in selection of the model support system. A sting-support system with the sting centered in the nozzle, if possible, should be used rather than a strut or wing tip support-type system.

REFERENCES

1. Chamberlin, Robert and Blahs, Bernard J. "Flight and Wind Tunnel Investigation of the Effects of Reynolds Number on Installed Boattail Drag at Supersonic Speeds." AIAA 11th Aerospace Sciences Meeting, Washington, D.C., January 10-12, 1973, AIAA Paper 73-139.

2. Reubush, David E. "The Effect of Reynolds Number on Boattail Drag." AIAA 13th Aerospace Sciences Meeting, Pasadena, California, January 20-22, 1975. AIAA Paper 75-63.

3. *Test Facilities Handbook* (Eleventh Edition). "Propulsion Wind Tunnel Facility, Vol. 4." Arnold Engineering Development Center, June 1979.

4. Lucas, Ernest J. "Wind Tunnel Results from a Nozzle Afterbody Test of a 0.1-Scale Fighter Aircraft in the Mach Number Regime of 0.6 to 1.6." AEDC-TR-78-25 (AD-B028240), April 1978.

5. Lucas, Ernest J. "Wind Tunnel Results from a Nozzle Afterbody Test of a 0.2-Scale Fighter Aircraft in the Mach Number Regime of 0.6 to 1.5." AEDC-TR-79-10, Vol. 1 (AD-B036406), April 1979, Vol. 2 (AD-B037421), May 1979.

6. Steers, Louis L. "Flight Measured Afterbody Pressure Coefficients from an Airplane Having Twin Side-by-Side Jet Engines for Mach Numbers from 0.6 to 1.6." NASA-TP-1549, 1979

7. Price, Earl A., Jr. "A Parametric Investigation of the Annular Jet Concept for Obtaining Afterbody Drag Data at Transonic Mach Numbers." AEDC-TR-77-104 (AD-A050891), February 1978.

8. Abernethy, R. B. and Thompson, J. W., Jr. "Handbook - Uncertainty in Gas Turbine Measurements." AEDC-TR-73-5 (AD755356), February 1973.

9. Reichenau, David E. A. "An Investigation of Model Scaling Effects at Mach Numbers from 0.60 to 1.40." AEDC-TR-73-202 (AD915551), December 1973.

10. Peters, William L. "An Evaluation of Jet Simulation Parameters for Nozzle Afterbody Testing at Transonic Mach Numbers." AEDC-TR-76-109 (AD-A031525), October 1976.

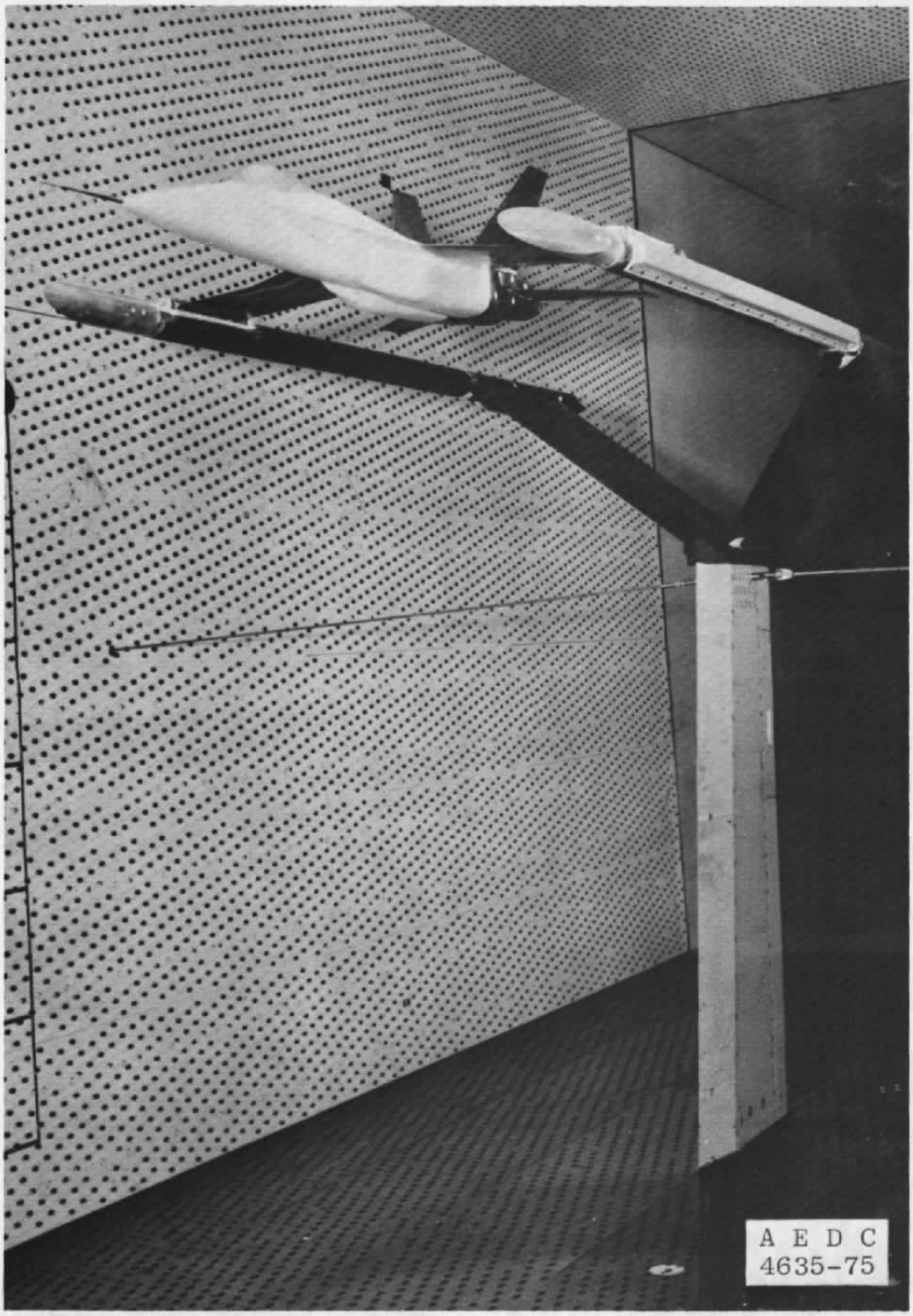

a. Model installation
Figure 1. 0.1-scale model.

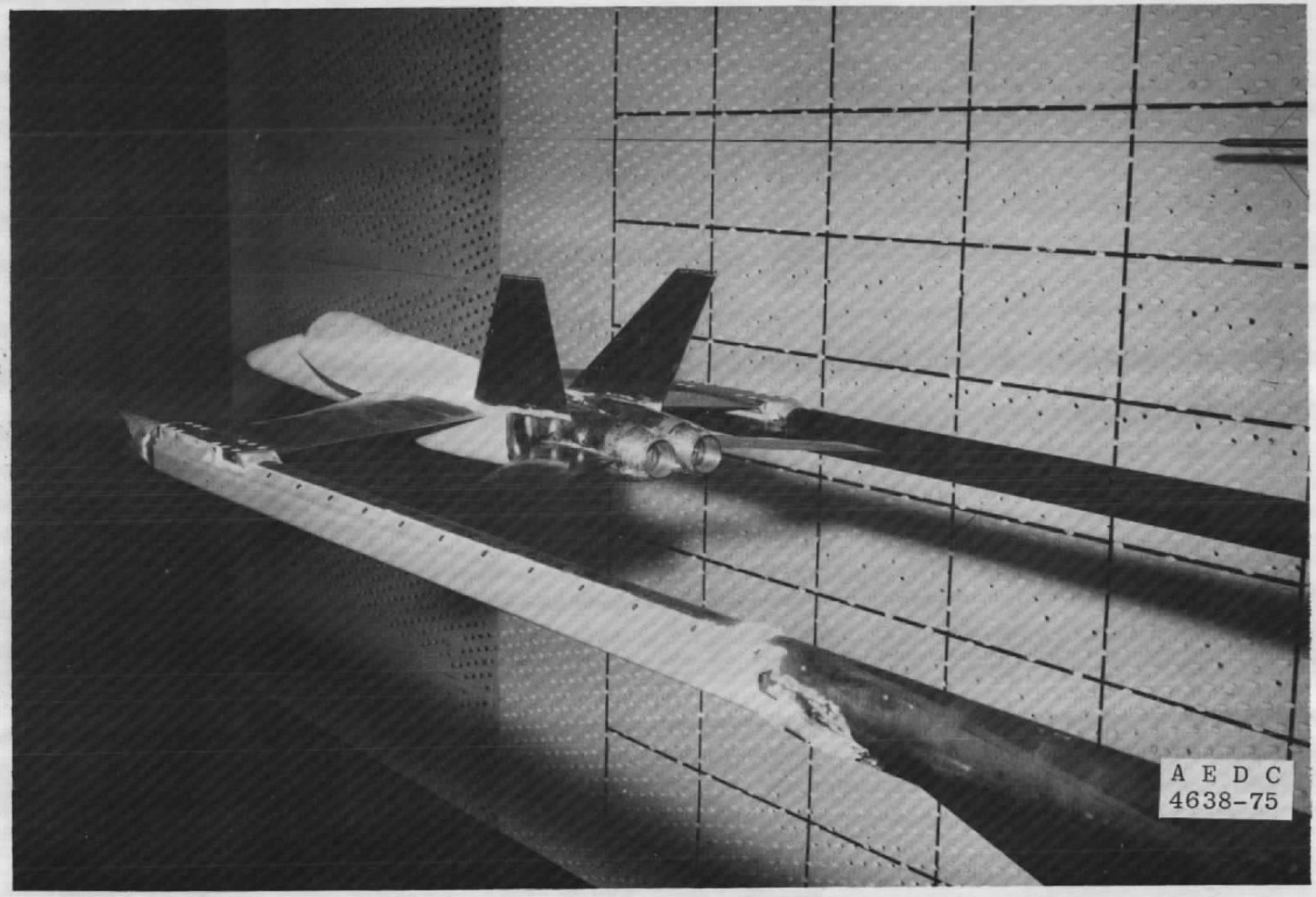

b. Aft 3/4-view of model
Figure 1. Continued.

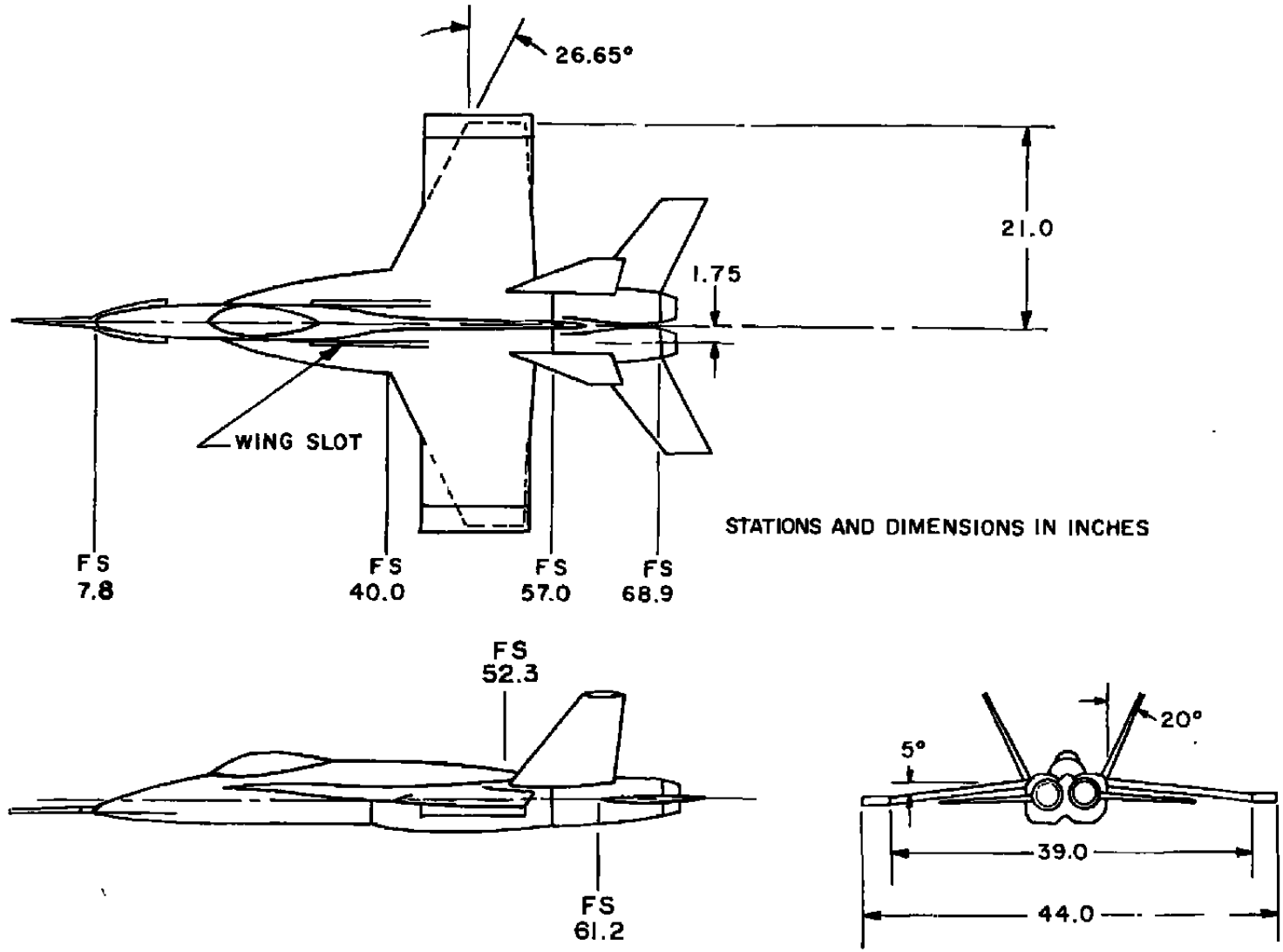

c. Major dimensions of the model

Figure 1. Concluded.

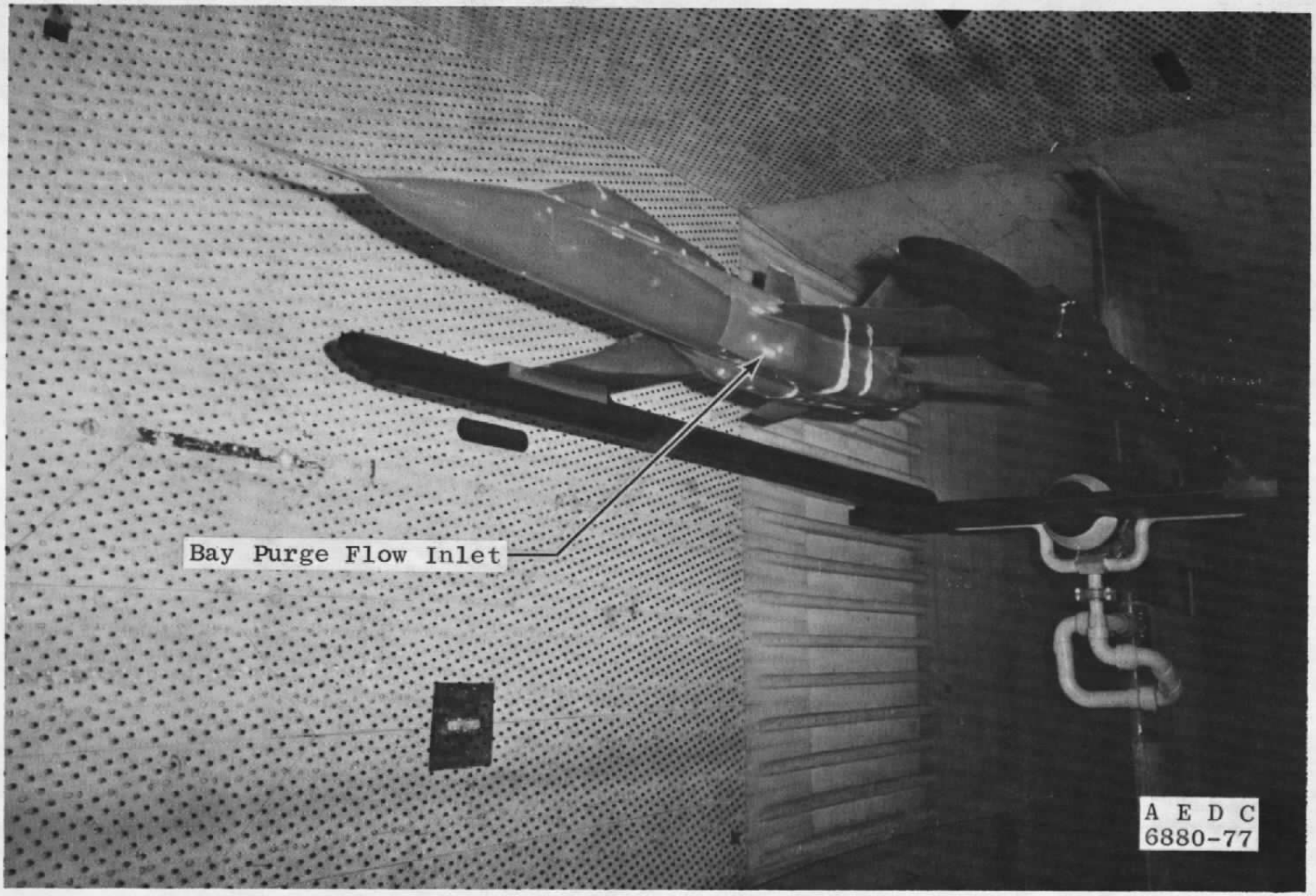

a. Model installation

Figure 2. 0.2-scale model.

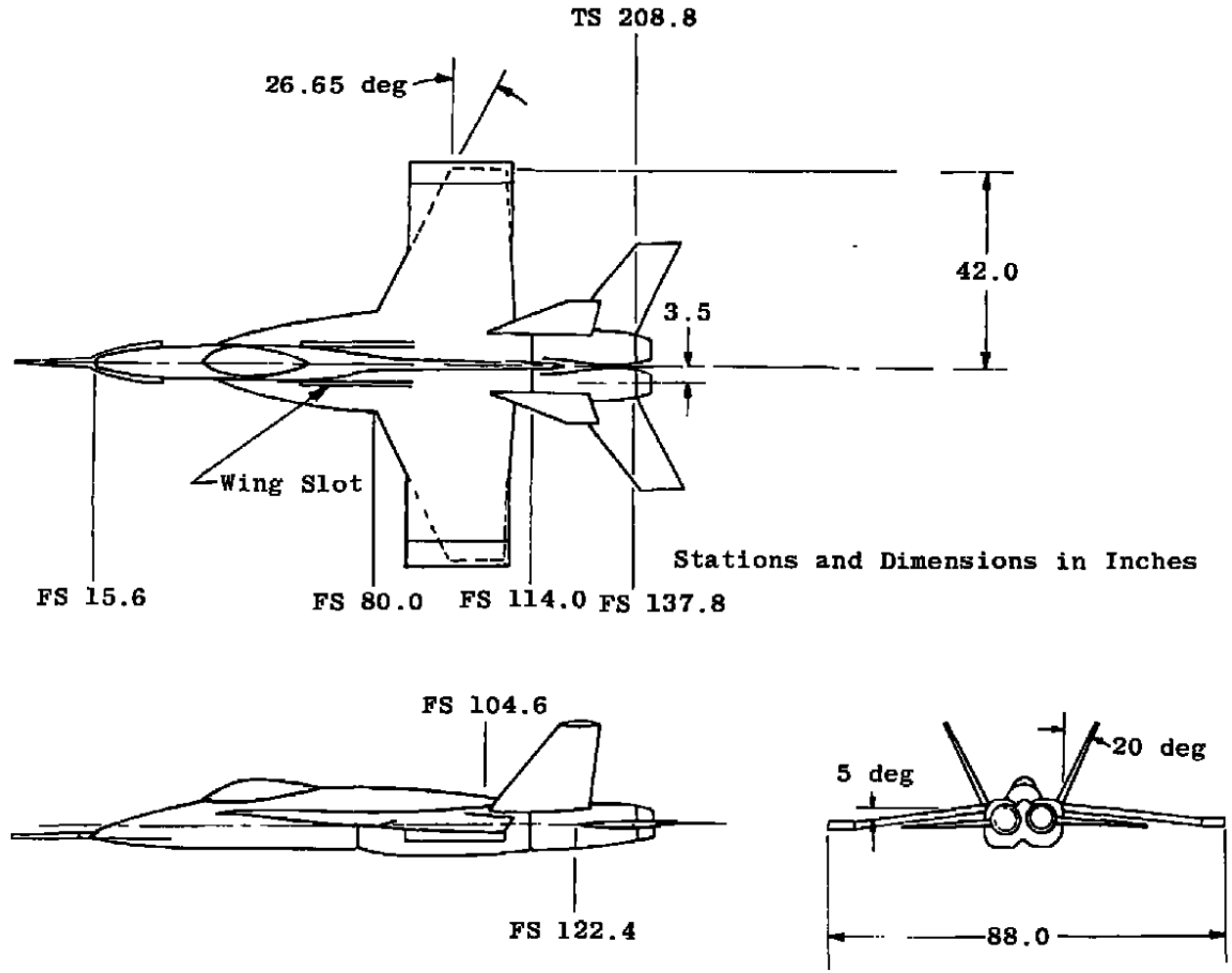

b. Major dimensions of the model

Figure 2. Continued.

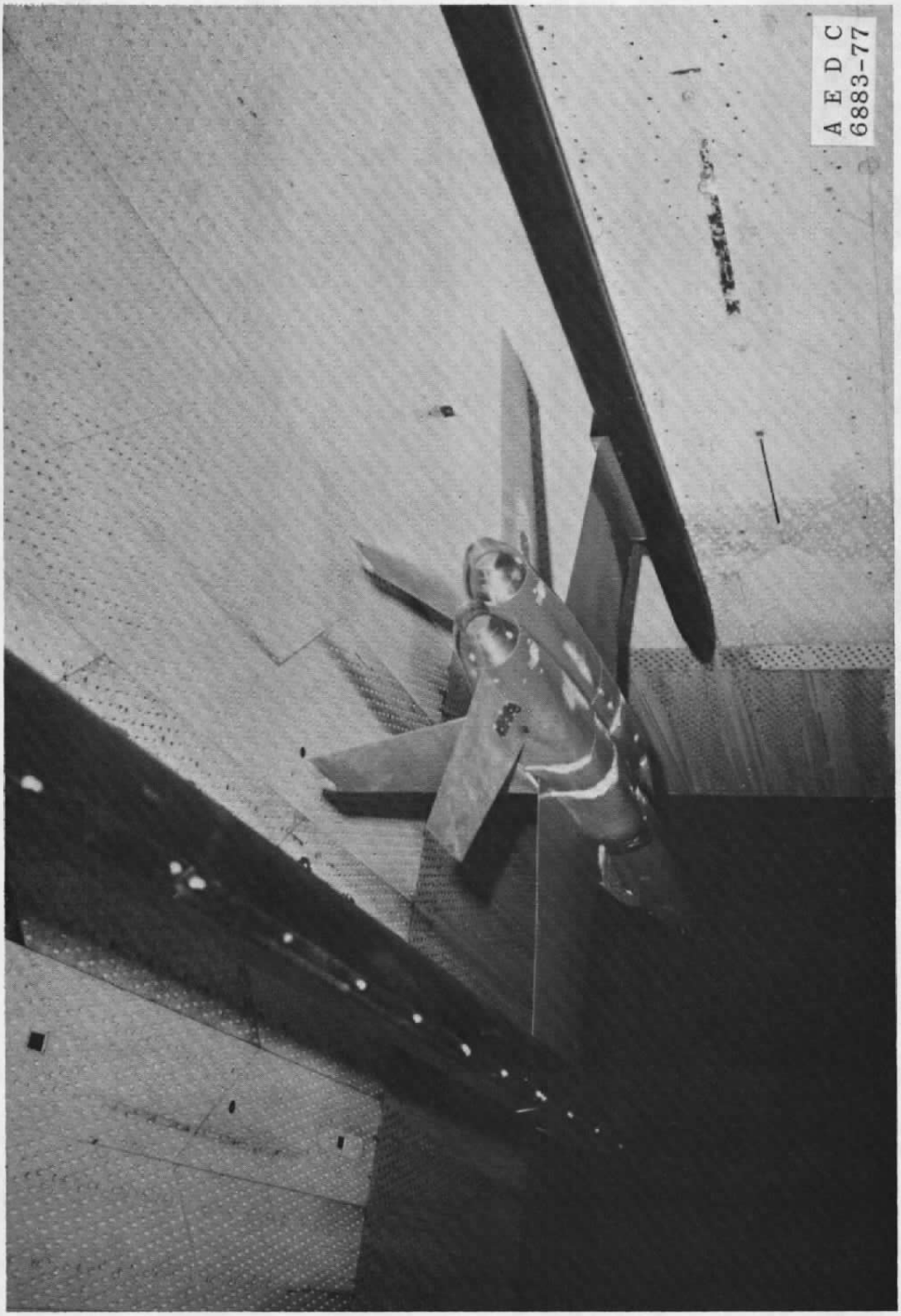

c. Aft 3/4-view of model
Figure 2. Continued.

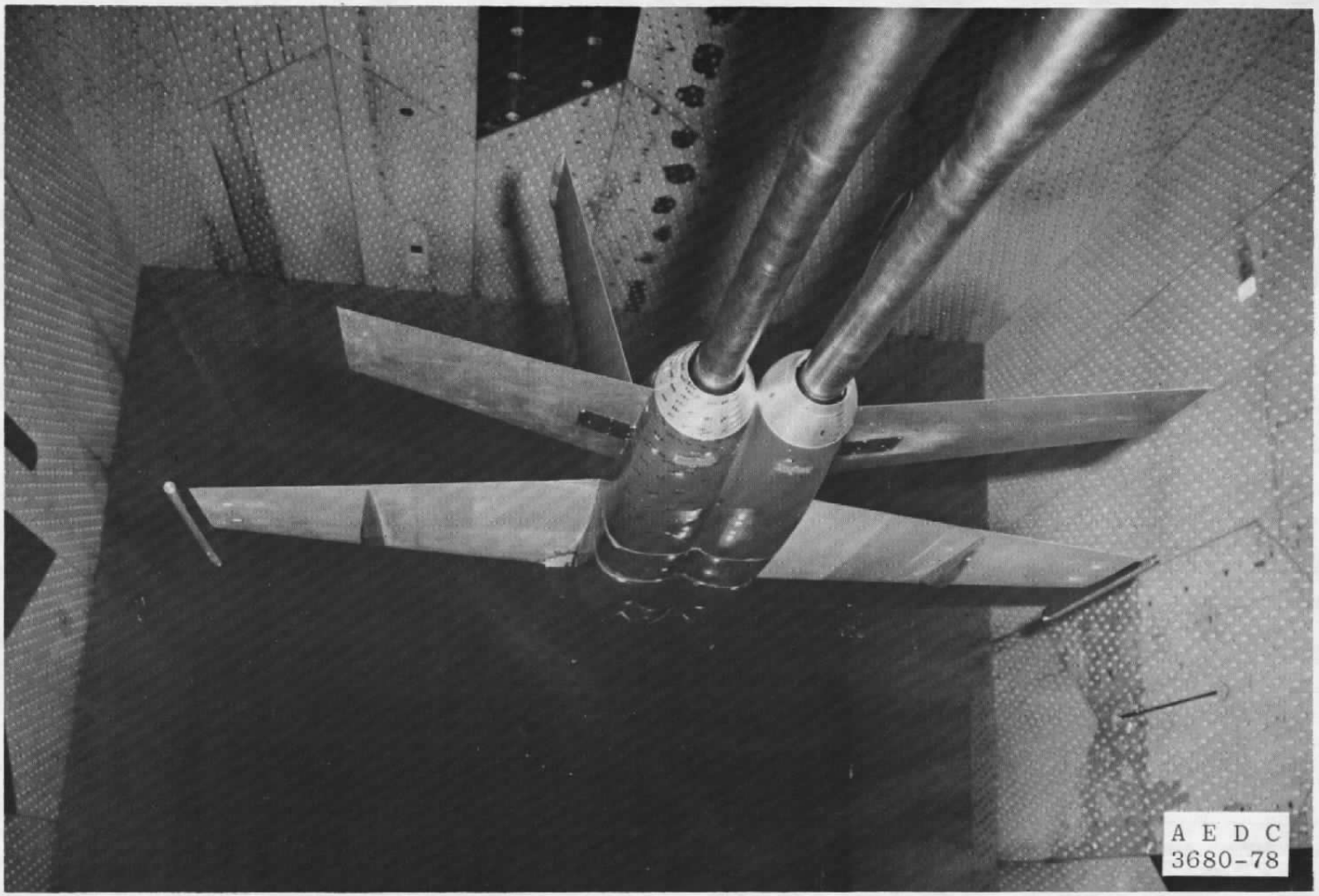

d. Underwing fairing and wingtip missile simulation
Figure 2. Concluded.

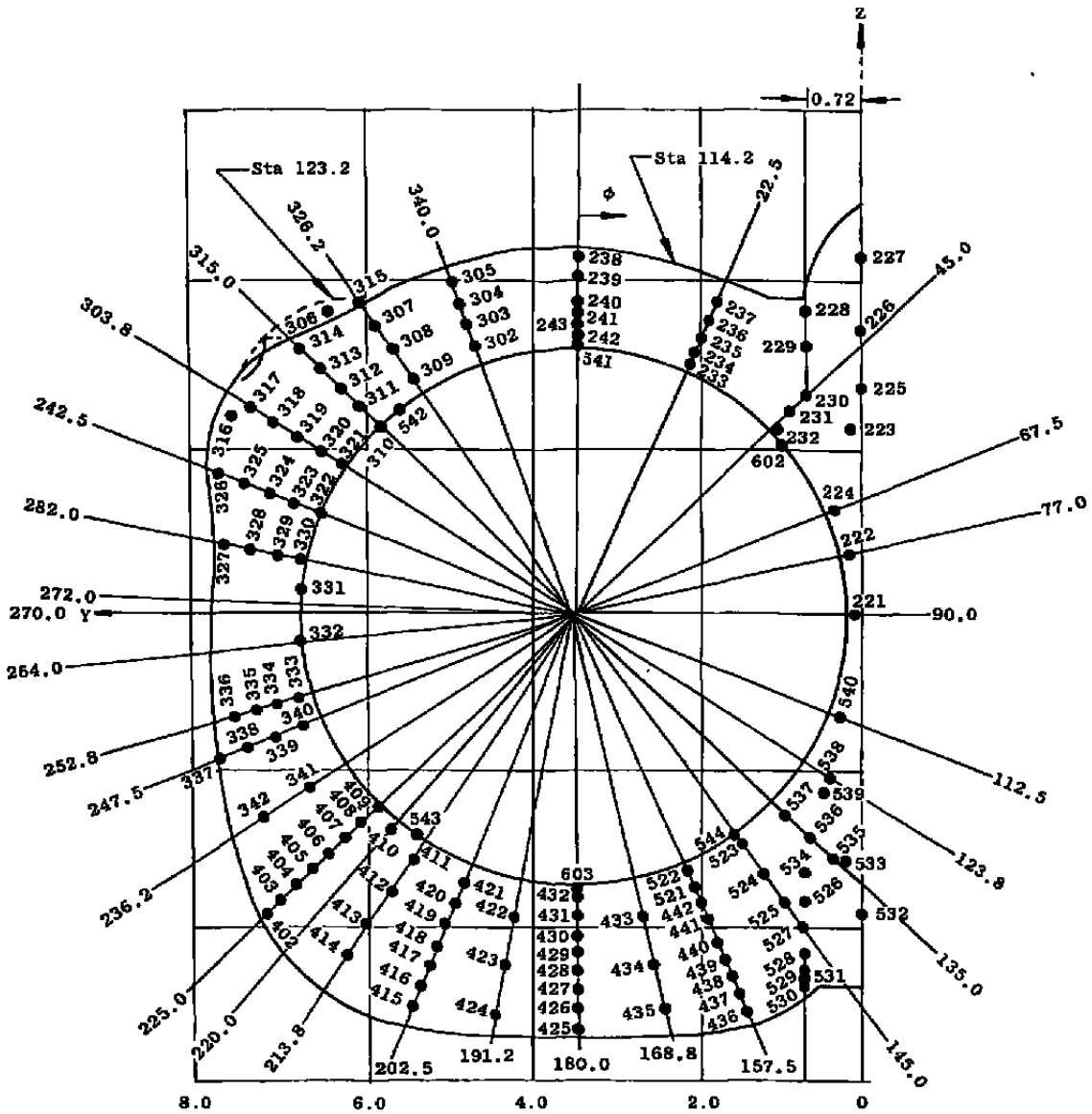

a. 0.2-scale model afterbody

Figure 3. Model surface pressure orifice distribution.

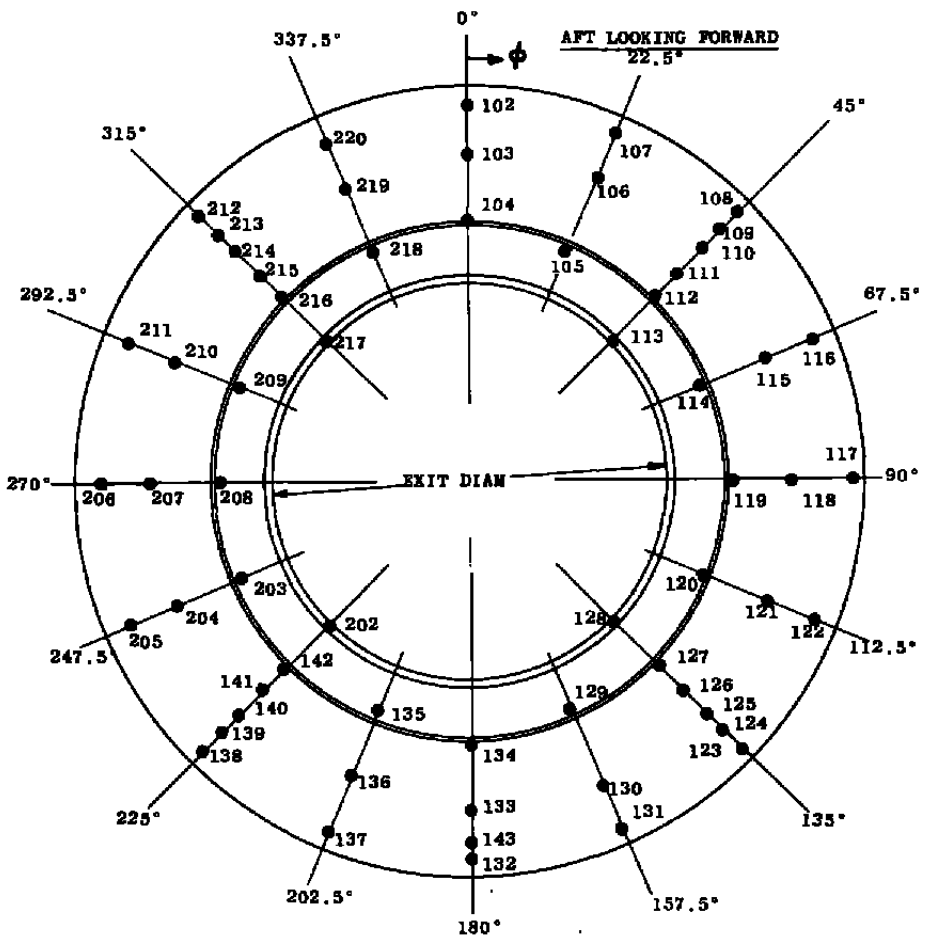

b. 0.2-scale model typical nozzle
Figure 3. Concluded.

Section	Full-Scale Station	X/L
AA	689.15	0.970
BB	687.30	0.967
CC	681.15	0.959
DD	672.15	0.946
EE	659.65	0.928
FF	644.65	0.907
GG	619.65	0.872
HH	595.65	0.838
II	570.65	0.803
JJ	528.65	0.744

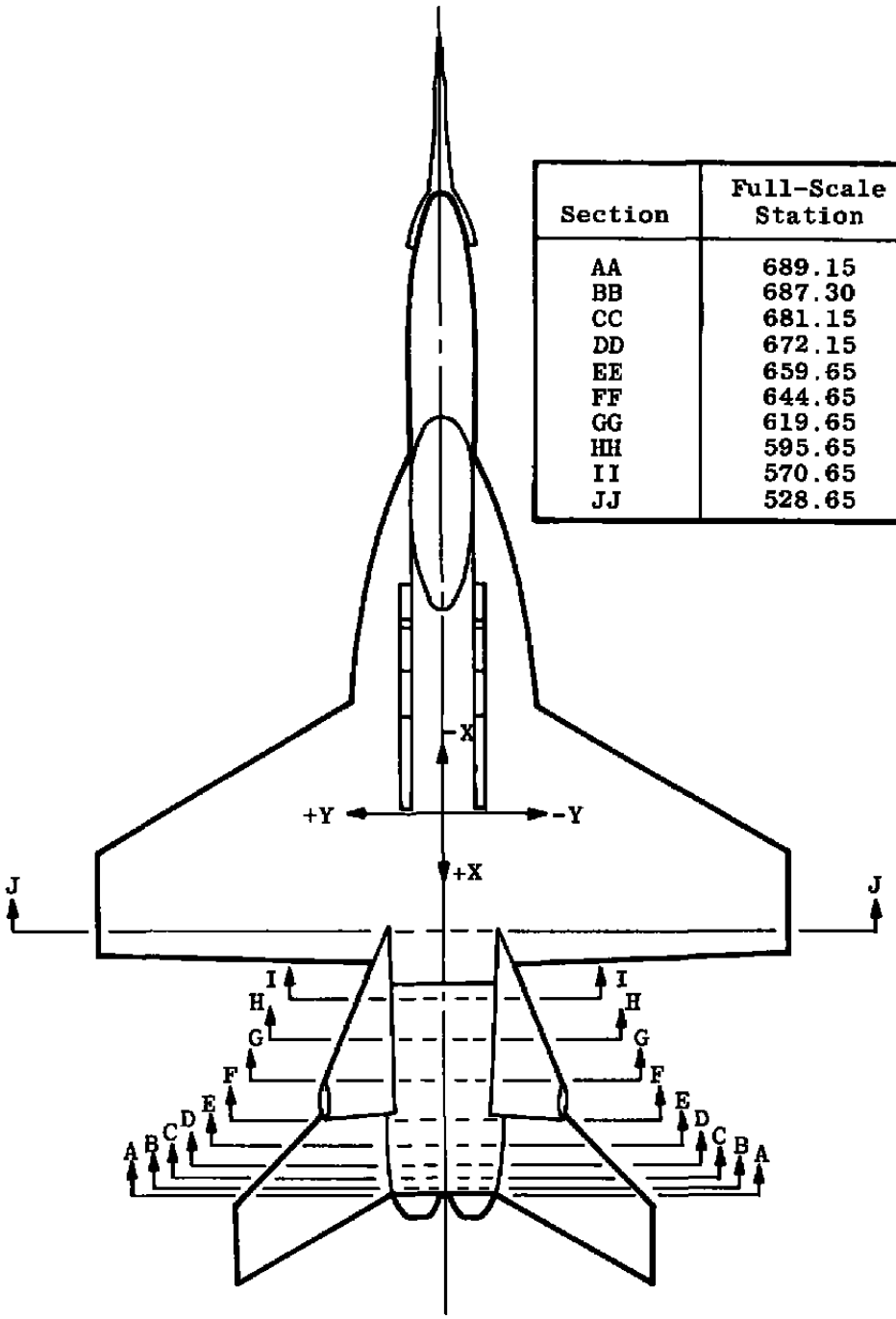

See Table 2 for Coordinates

Figure 4. 0.2-scale model contour stations.

a. YF-17 prototype

Figure 5. Full-scale flight vehicle.

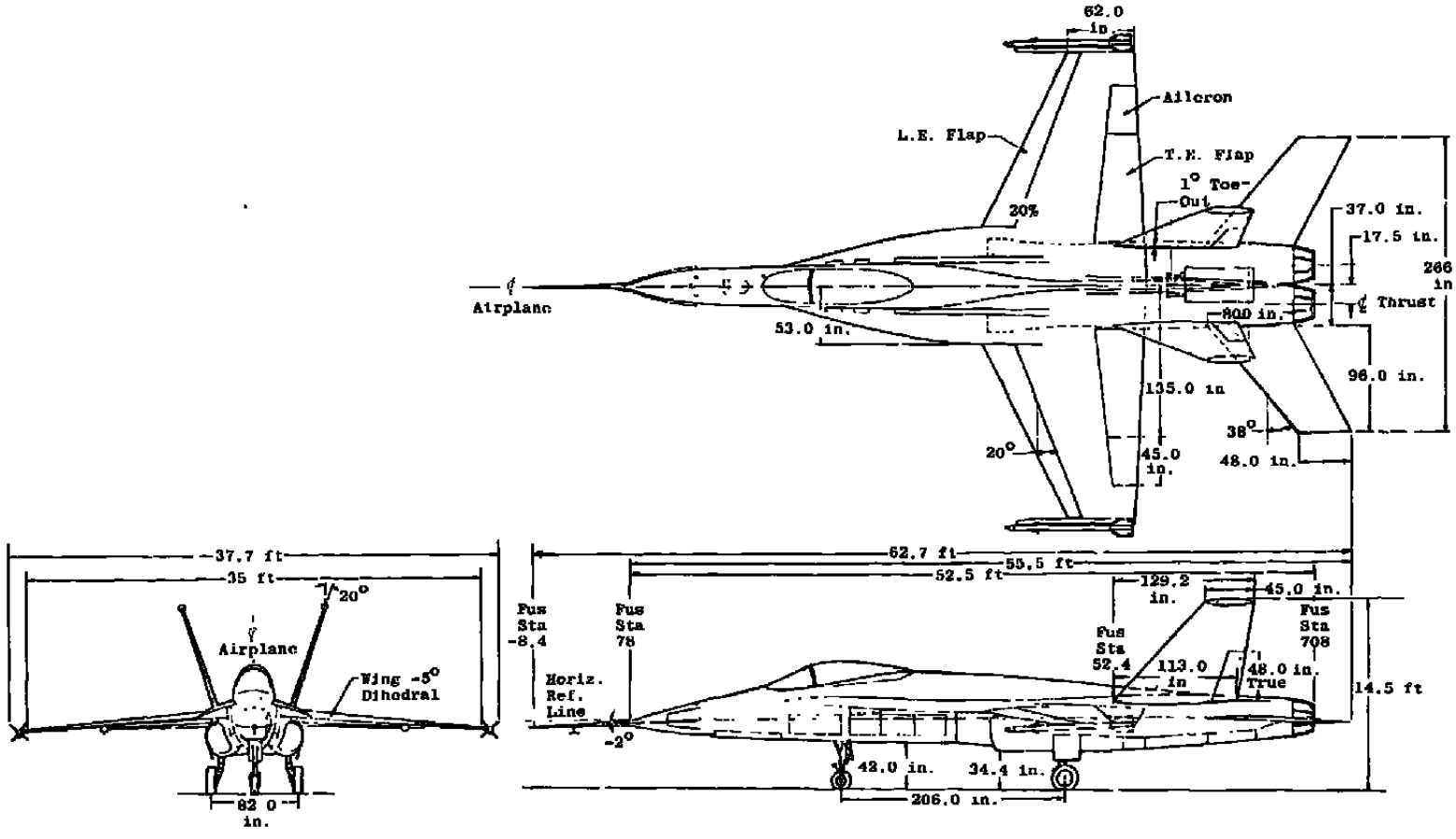

b. Major dimensions

Figure 5. Concluded.

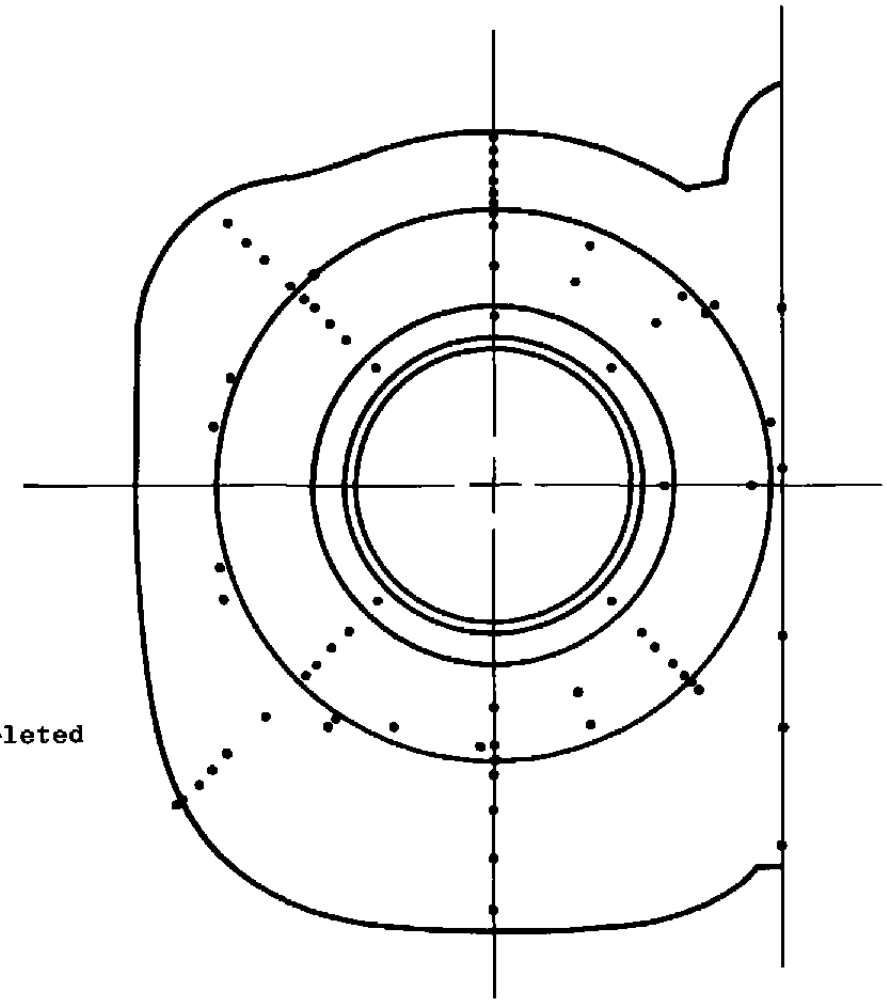

Figure 6. Flight test instrumentation location.

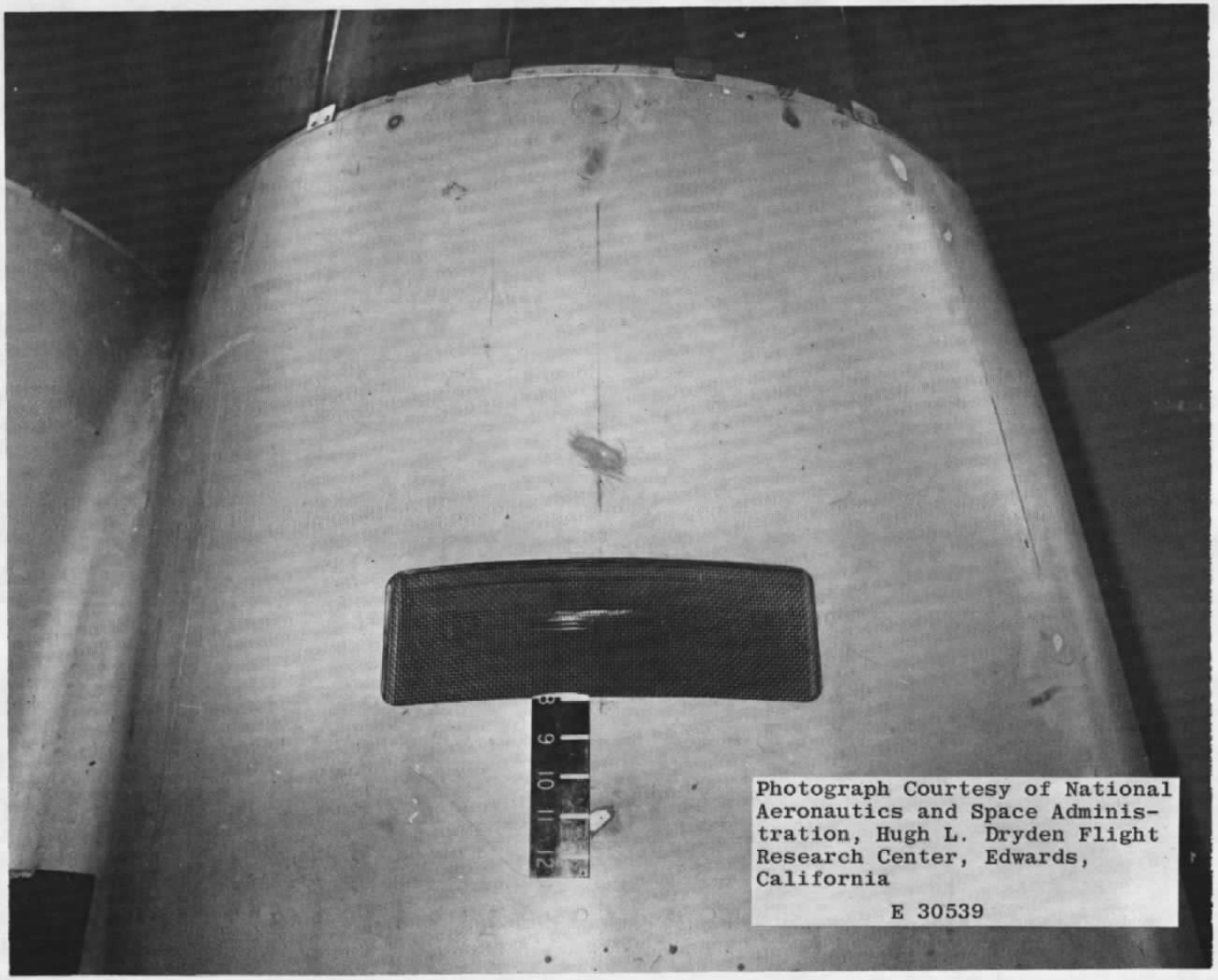

Figure 7. Flight vehicle surface orifice installation.

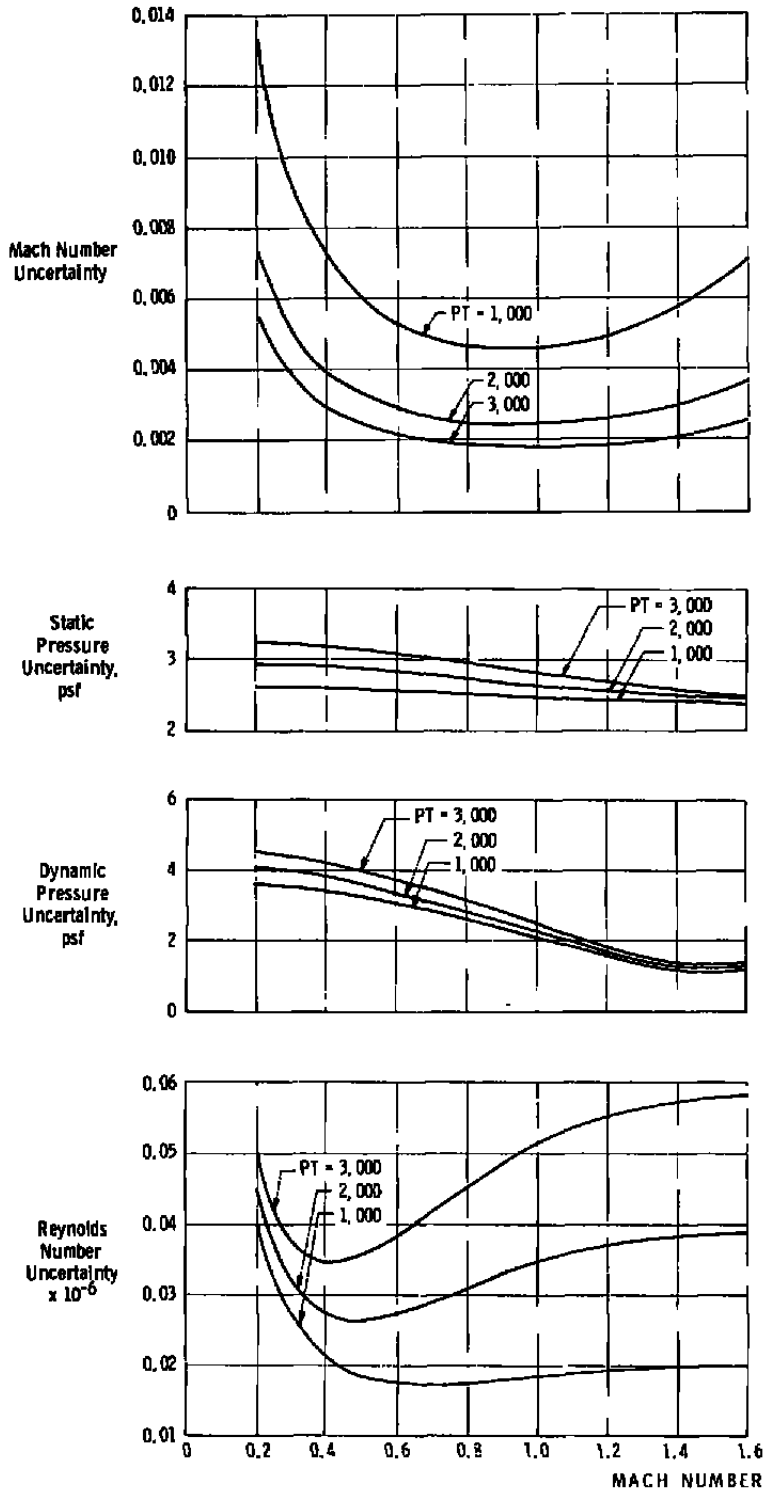

Figure 8. Estimated uncertainties in wind tunnel parameters.

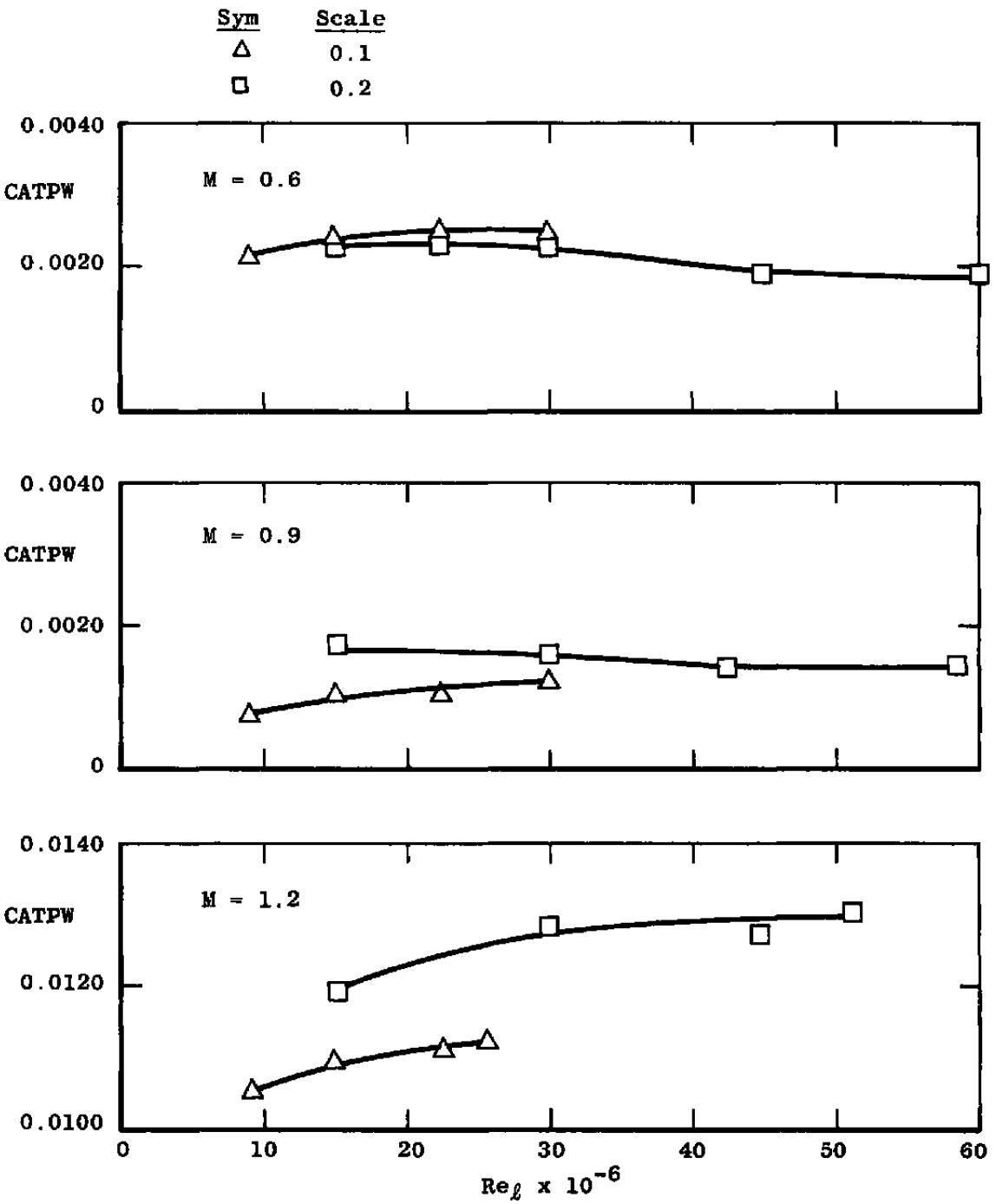

a. Cruise nozzle, NPR ~ 3.4, α ~ 4 deg

Figure 9. Wind tunnel-model scaling effect.

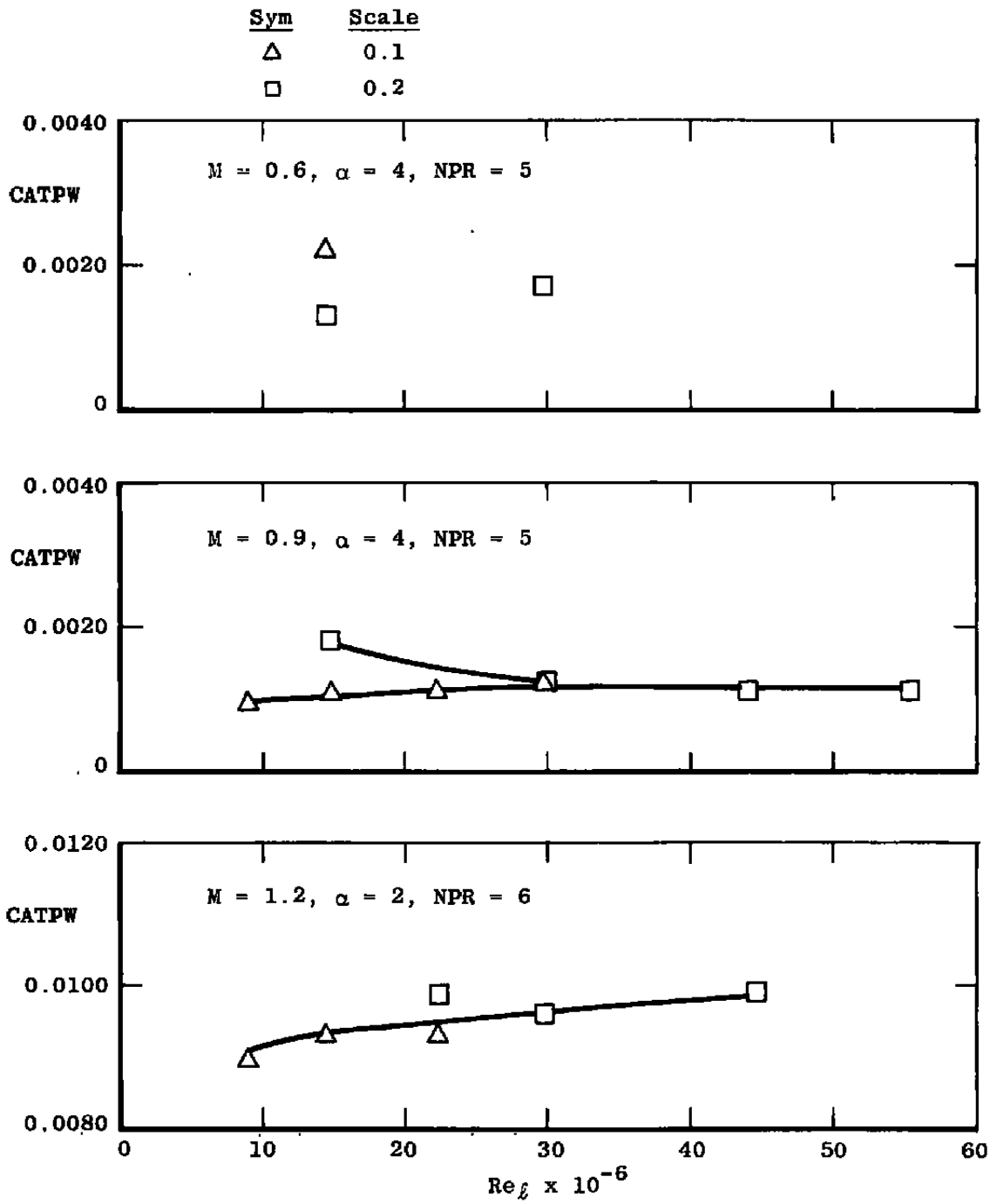

b. Reheat nozzle

Figure 9. Concluded.

SYM	M	Re_ℓ	A8	NPR	α	δ_H	CATPW	PN/PT	SCALE
△	0.60	29.7	200.	3.0	4.0	0.0	0.0025	142.04	0.1
□	0.60	29.8	200.	3.4	4.1	0.0	0.0023	511.04	0.2

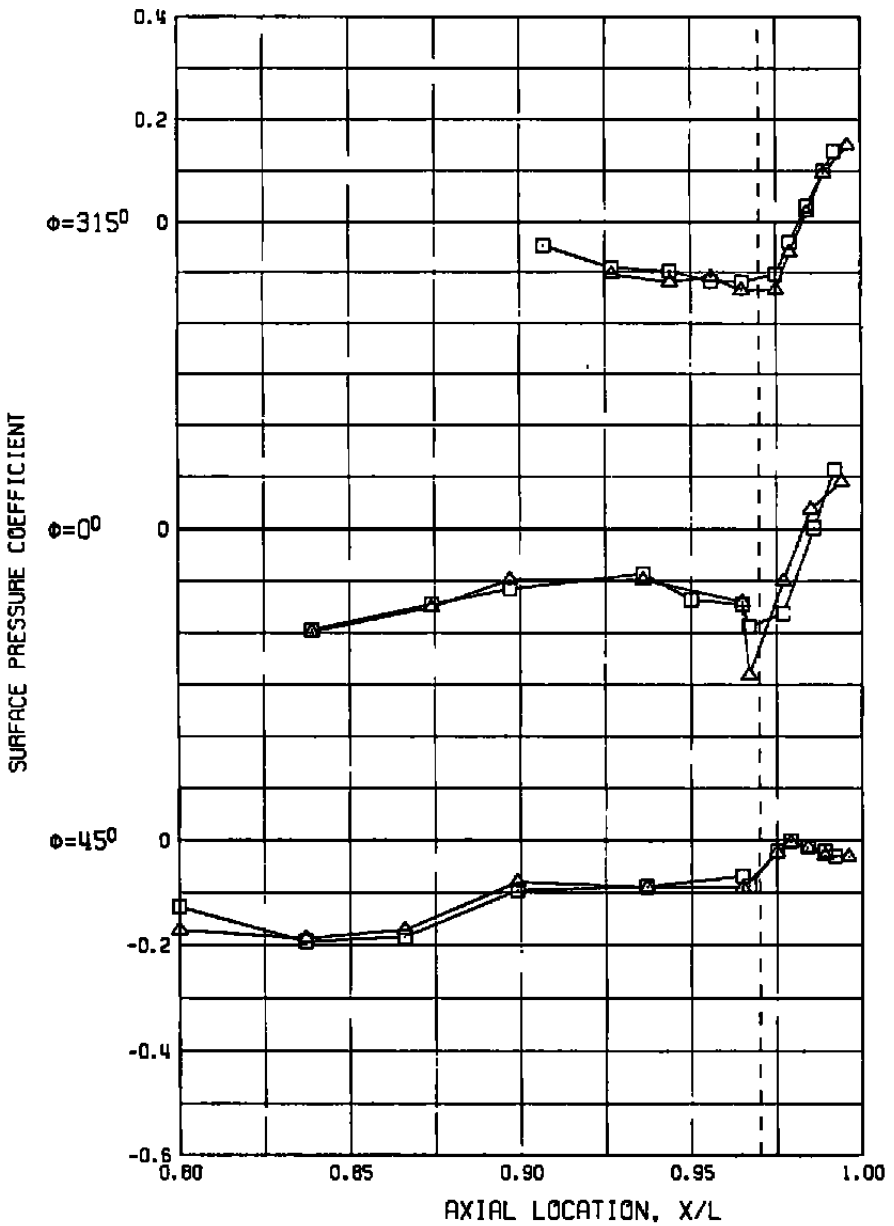

a. Lee-side pressures

Figure 10. Effect of model scale on the surface pressure distribution at matched Re_ℓ, M = 0.6, A8 = 200 in.^{2}, α = 4 deg, and NPR ~ 3.0

SYM	M	Re_{ℓ}	AB	NPR	α	δ_H	CATPW	PN/PT	SCALE
△	0.60	29.7	200.	3.0	4.0	0.0	0.0025	142.04	0.1
□	0.60	29.8	200.	3.4	4.1	0.0	0.0023	511.04	0.2

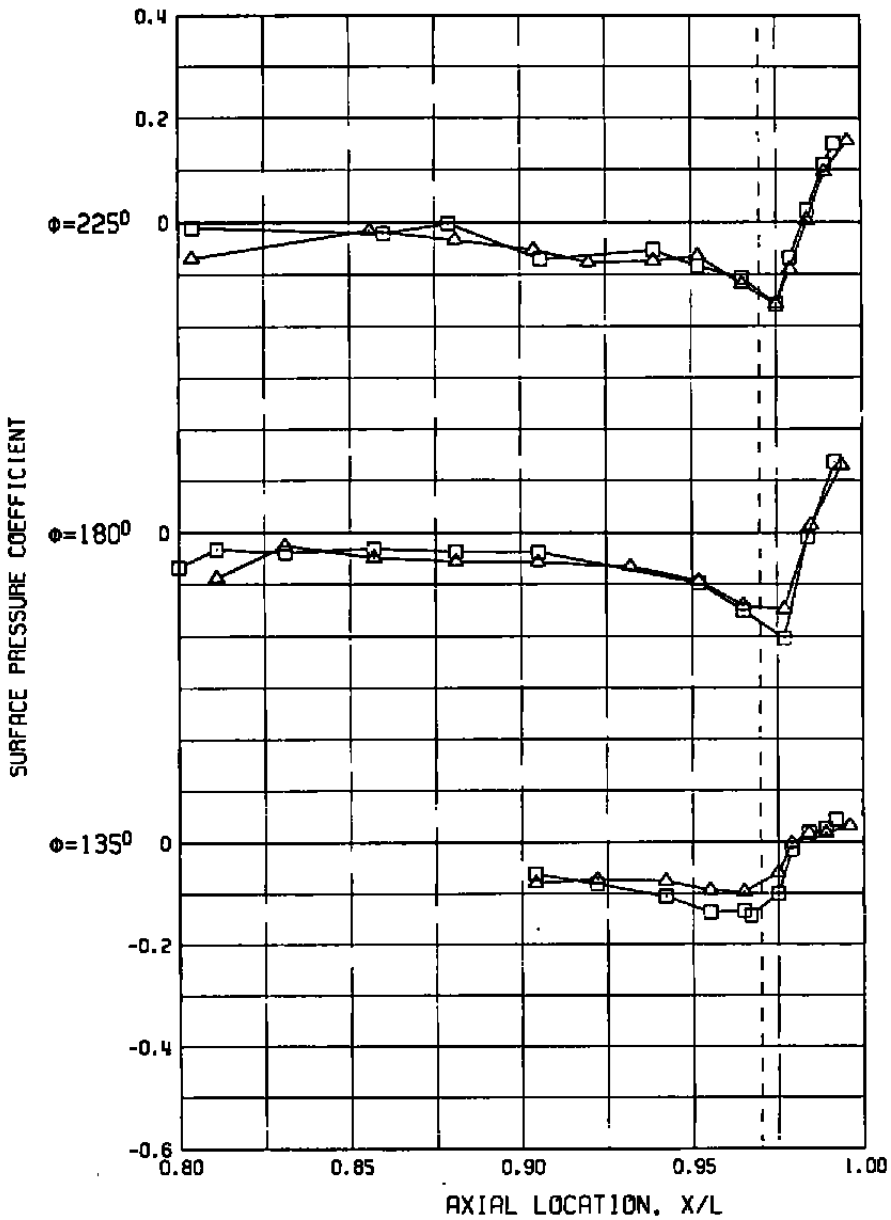

b. Windward-side pressures

Figure 10. Concluded.

SYM	M	Re_ℓ	A8	NPR	α	γ	CATPW	PN/PT	SCALE
·	0.90	29.7	200.	3.4	4.1	0.0	0.0012	30.04	0.1
⊡	0.90	29.9	200.	3.4	4.1	0.0	0.0016	522.06	0.2

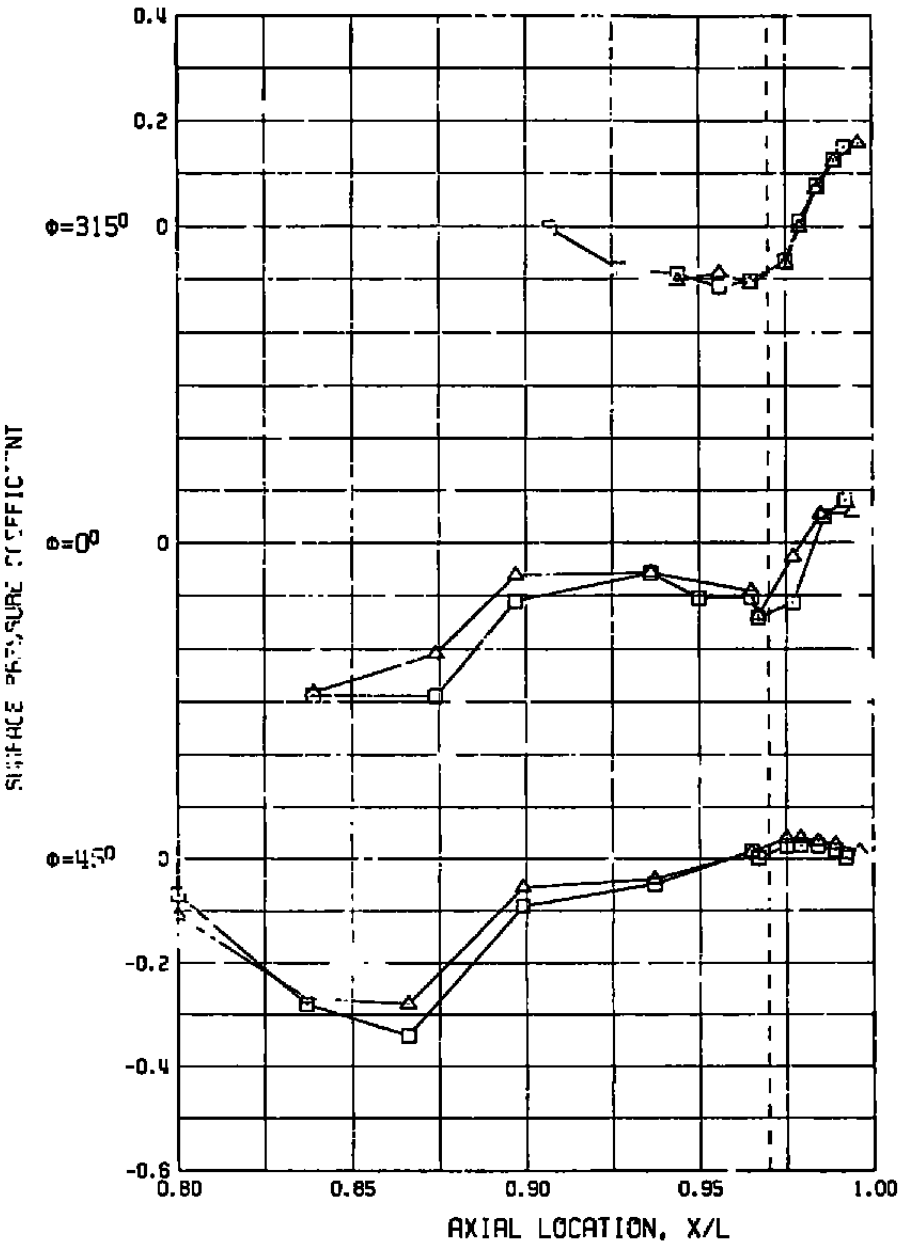

a. Lee-side pressures

Figure 11. Effect of model scale on the surface pressure distribution at matched Re_ℓ, M = 0.9, A8 = 200 in.^{2}, α = 4 deg, and NPR = 3.4.

SYM	M	Re_L	AB	NPR	α	δ_H	CRTPW	PN/PT	SCALE
△	0.90	29.7	200.	3.4	4.1	0.0	0.0012	30.04	0.1
⊡	0.90	29.9	200.	3.4	4.1	0.0	0.0016	522.06	0.2

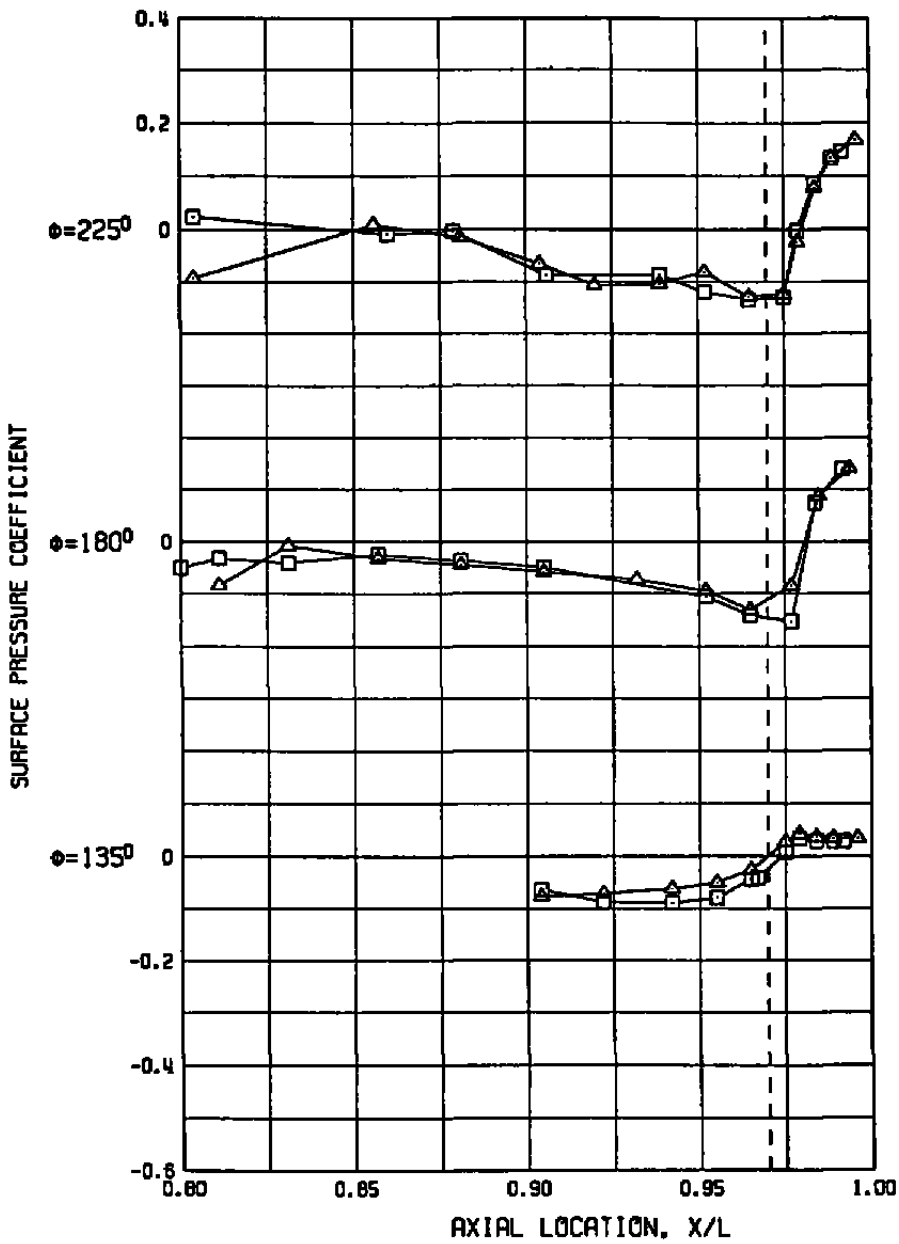

b. Windward-side pressures

Figure 11. Concluded.

SYM	M	Re_ℓ	AB	NPR	α	δ_H	CATPW	PN/PT	SCALE
△	1.20	25.4	200.	3.4	4.1	-2.0	0.0112	174.03	0.1
□	1.20	29.7	200.	3.4	4.0	-2.0	0.0128	562.02	0.2
◇	1.20	14.9	200.	3.3	4.0	-2.0	0.0119	560.02	0.2

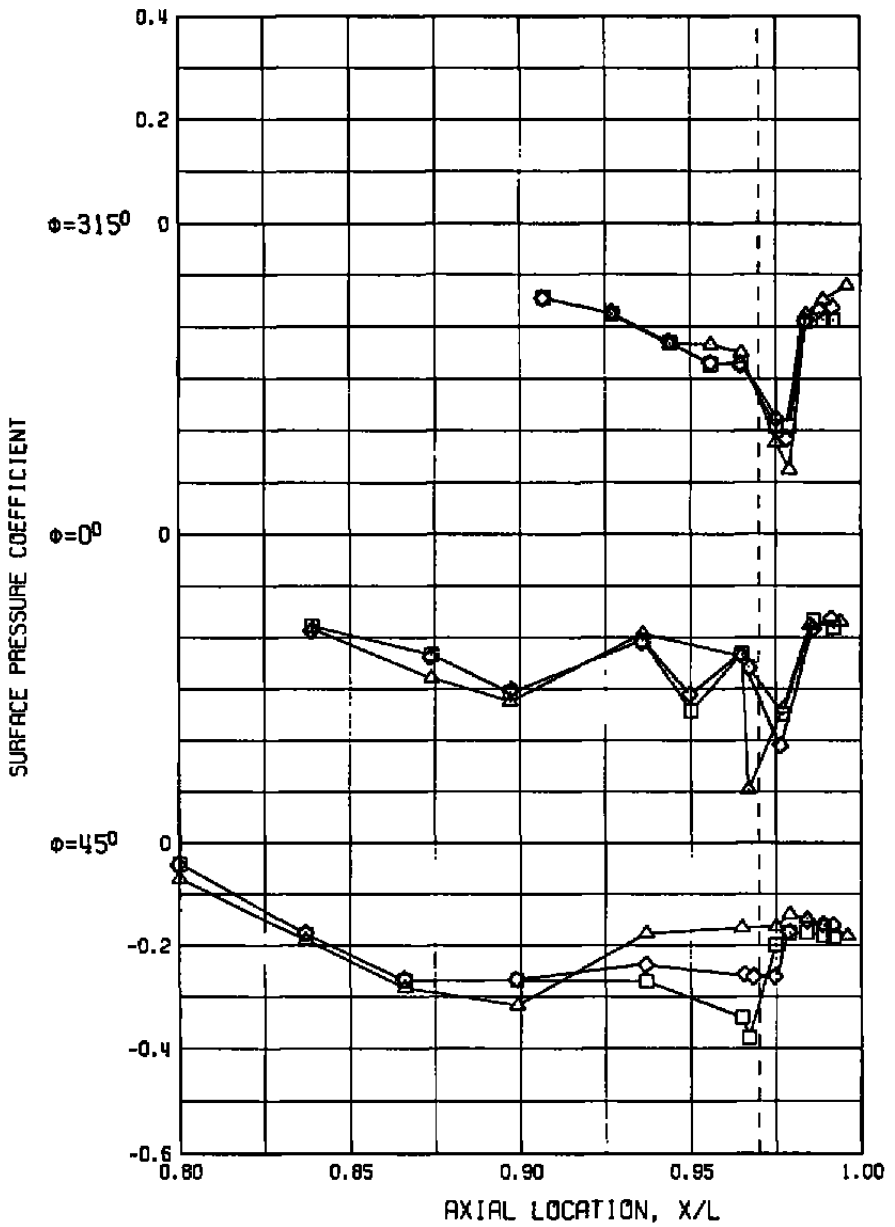

a. Lee-side pressures

Figure 12. Effect of model scale on the surface pressure distribution at matched Re_ℓ, M = 1.2, AB = 200 in.^{2}, $\alpha \sim 4$ deg and NPR = 3.4.

SYM	M	Re_ℓ	AB	NPR	α	δ_H	CATPW	PN/PT	SCALE
△	1.20	25.4	200.	3.4	4.1	-2.0	0.0112	174.03	0.1
⊡	1.20	29.7	200.	3.4	4.0	-2.0	0.0128	562.02	0.2
◇	1.20	14.9	200.	3.3	4.0	-2.0	0.0119	560.02	0.2

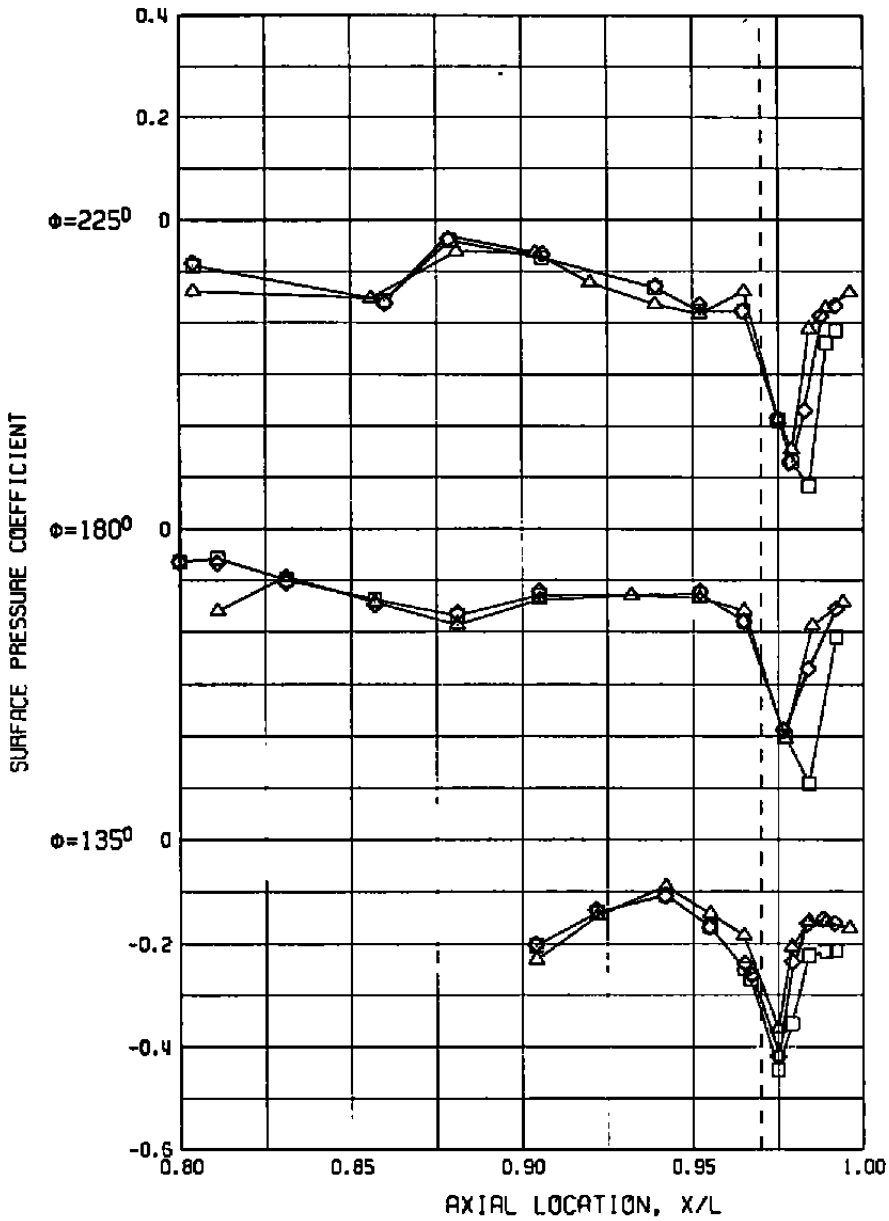

b. Windward-side pressures

Figure 12. Concluded.

SYM	M	Re_{ℓ}	A8	NPR	α	δ_H	CATPW	PN/PT	SCALE
△	0.90	29.7	286.	5.0	4.2	0.0	0.0012	75.02	0.1
□	0.90	29.9	300.	5.0	4.1	0.0	0.0011	694.03	0.2

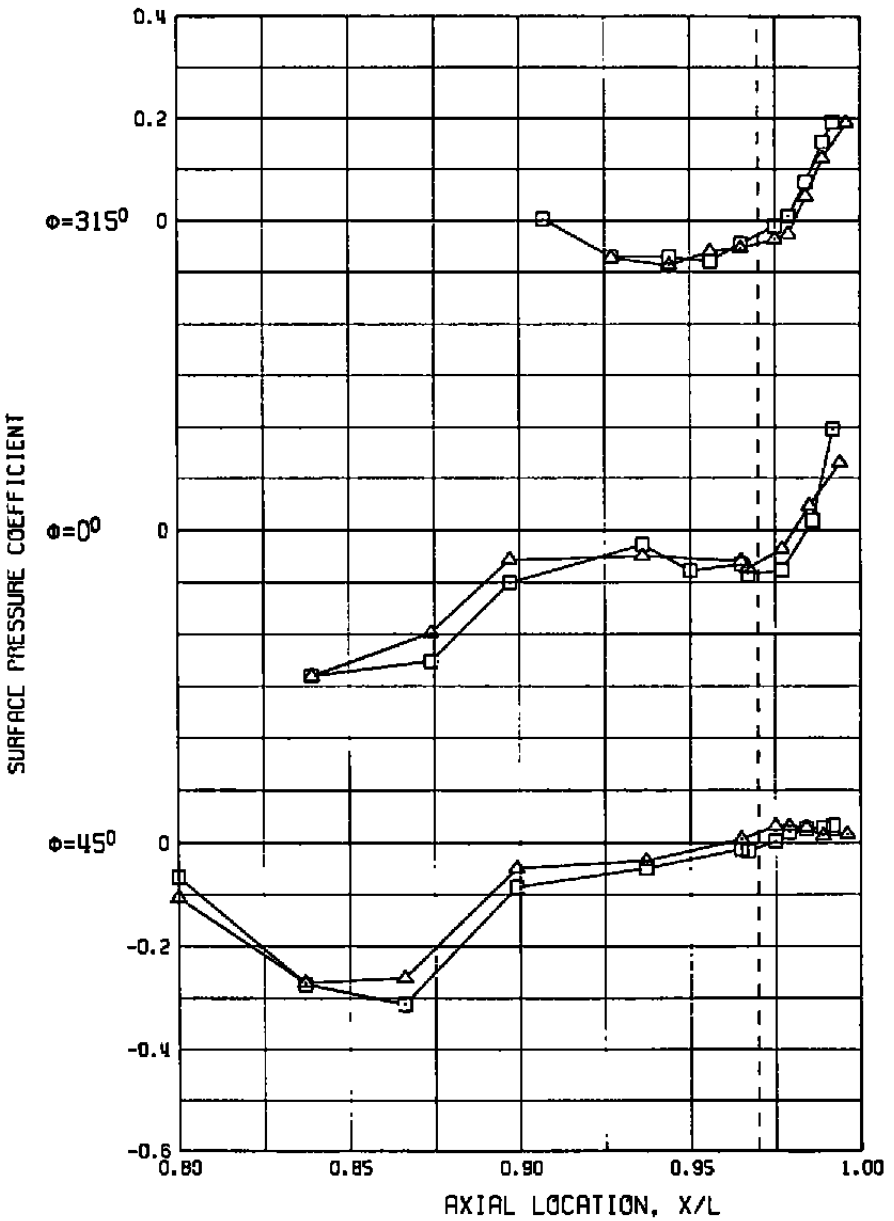

a. Lee-side pressures

Figure 13. Effect of model scale on the surface pressure distribution at matched Re_{ℓ}, M = 0.9, A8 ~ 300 in.², α ~ 4 deg, and NPR = 5.0.

SYM	M	Re_{ℓ}	AB	NPR	α	δ_H	CATPW	PN/PT	SCALE
△	0.90	29.7	286.	5.0	4.2	0.0	0.0012	75.02	0.1
□	0.90	29.9	300.	5.0	4.1	0.0	0.0011	694.03	0.2

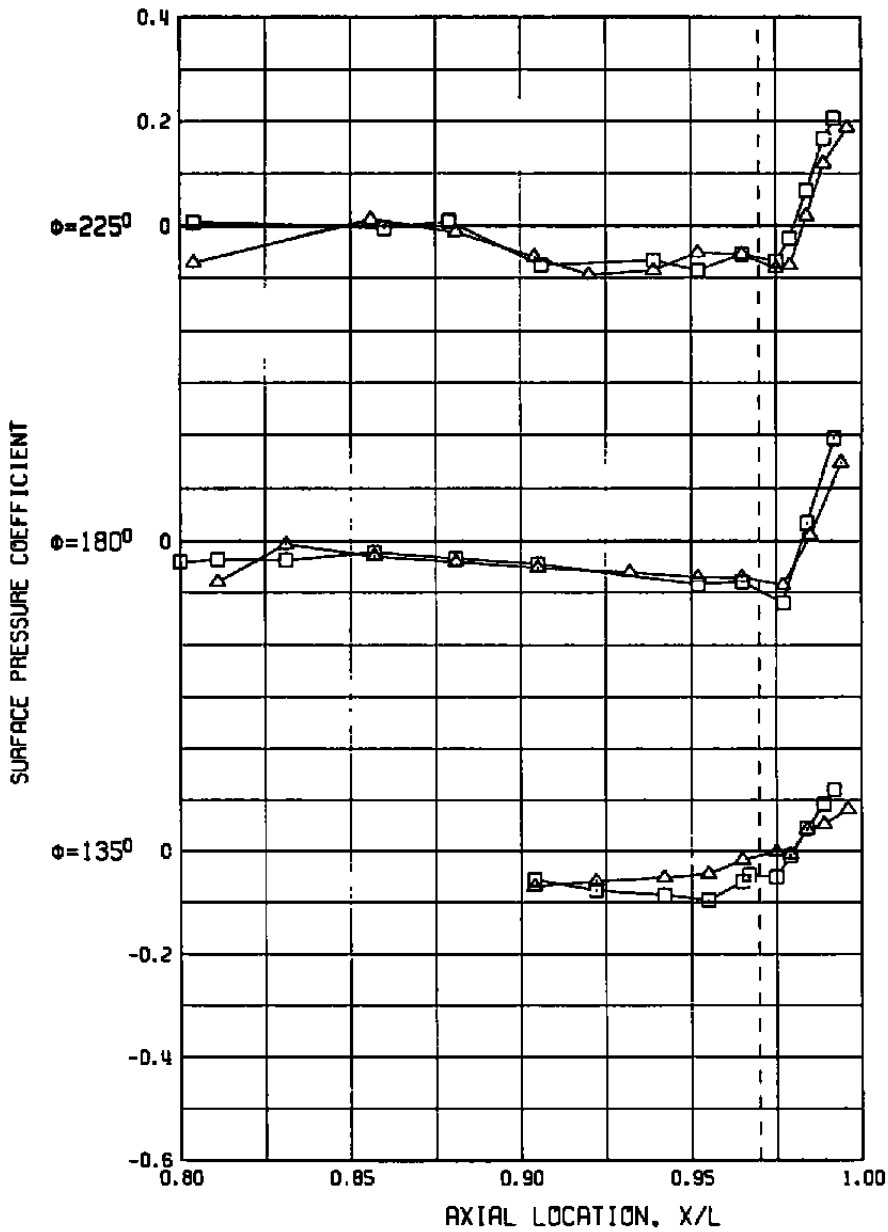

b. Windward-side pressures
Figure 13. Concluded.

SYM	M	Re_ℓ	AB	NPR	α	δ_H	CRTPN	PN/PT	SCALE
△	1.20	22.2	286.	6.1	2.1	0.0	0.0093	76.02	0.1
□	1.20	22.2	300.	6.3	2.1	0.0	0.0099	678.01	0.2

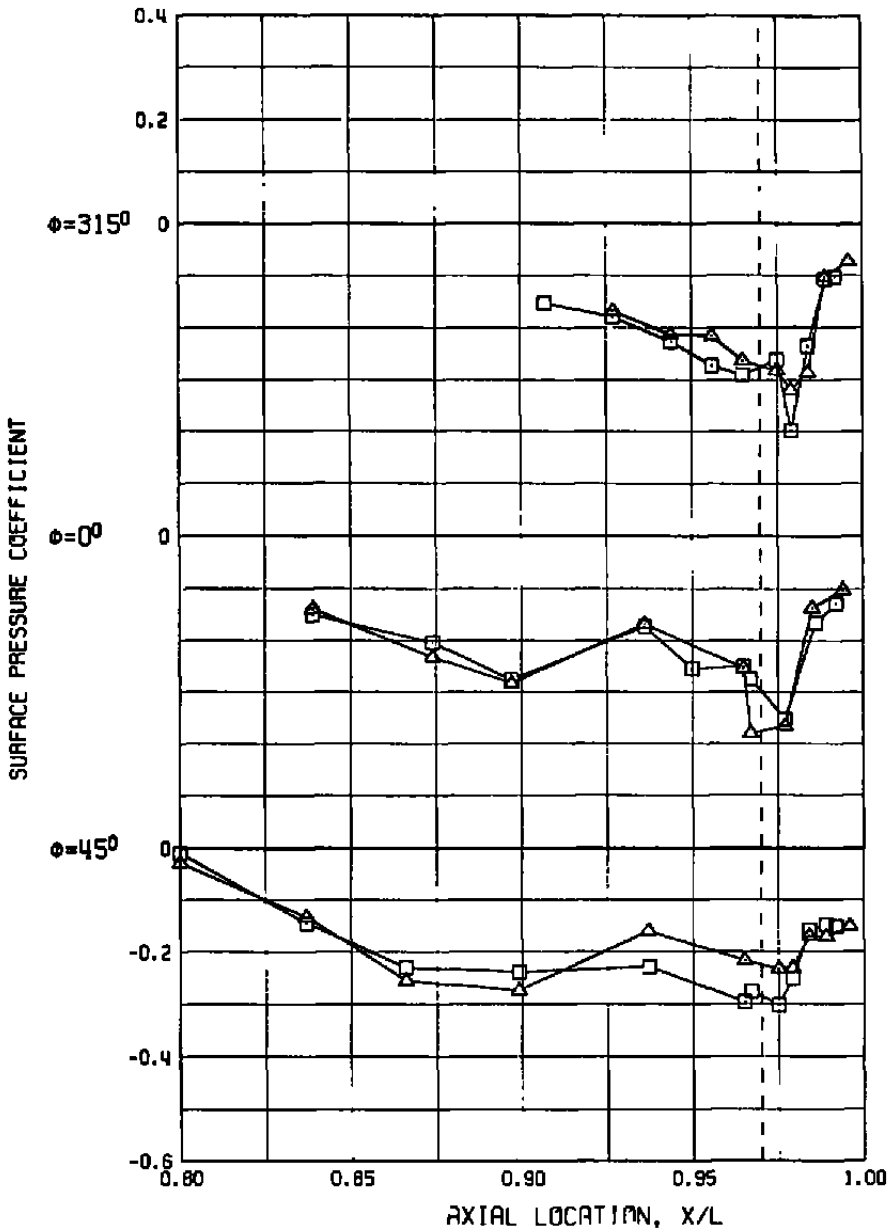

a. Lee-side pressures

Figure 14. Effect of model scale on the surface pressure distribution at matched Re_ℓ, M = 1.2, AB ~ 300 in.^{2}, α ~ 2 deg, and NPR ~ 6.0.

SYM	M	Re_ℓ	AB	NPR	α	δ_H	CATPW	PN/PT	SCALE
△	1.20	22.2	286.	6.1	2.1	0.0	0.0093	76.02	0.1
□	1.20	22.2	300.	6.3	2.1	0.0	0.0099	678.01	0.2

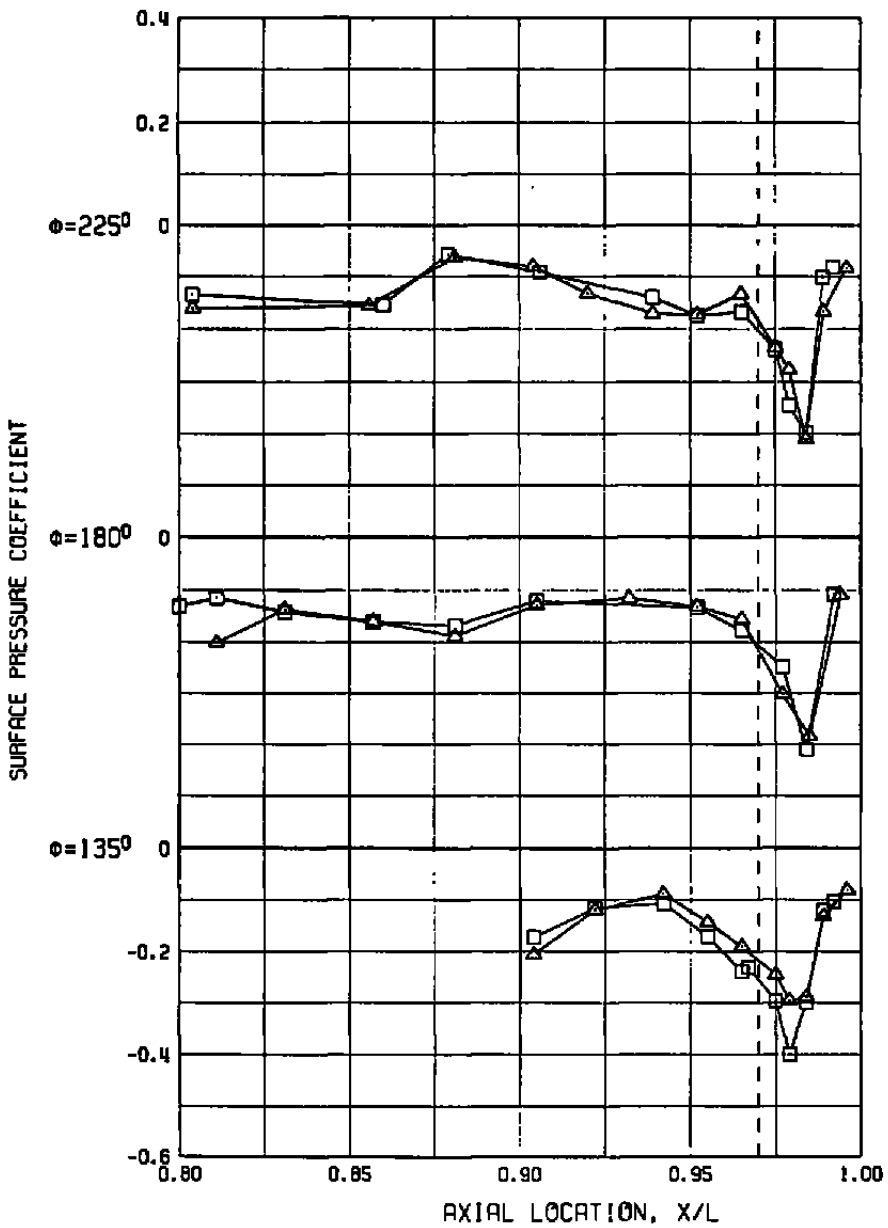

b. Windward-side pressures
Figure 14. Concluded.

SYM	M	Re_{ℓ}	A8	NPR	α	δ_H	CATPW	PN/PT
◇	0.60	9.0	200.	3.0	4.2	0.0	0.0021	24.02
○	0.60	14.9	200.	3.0	4.2	0.0	0.0024	26.02
□	0.60	22.3	200.	3.0	4.2	0.0	0.0025	29.04
△	0.60	29.7	200.	3.0	4.0	0.0	0.0025	142.04

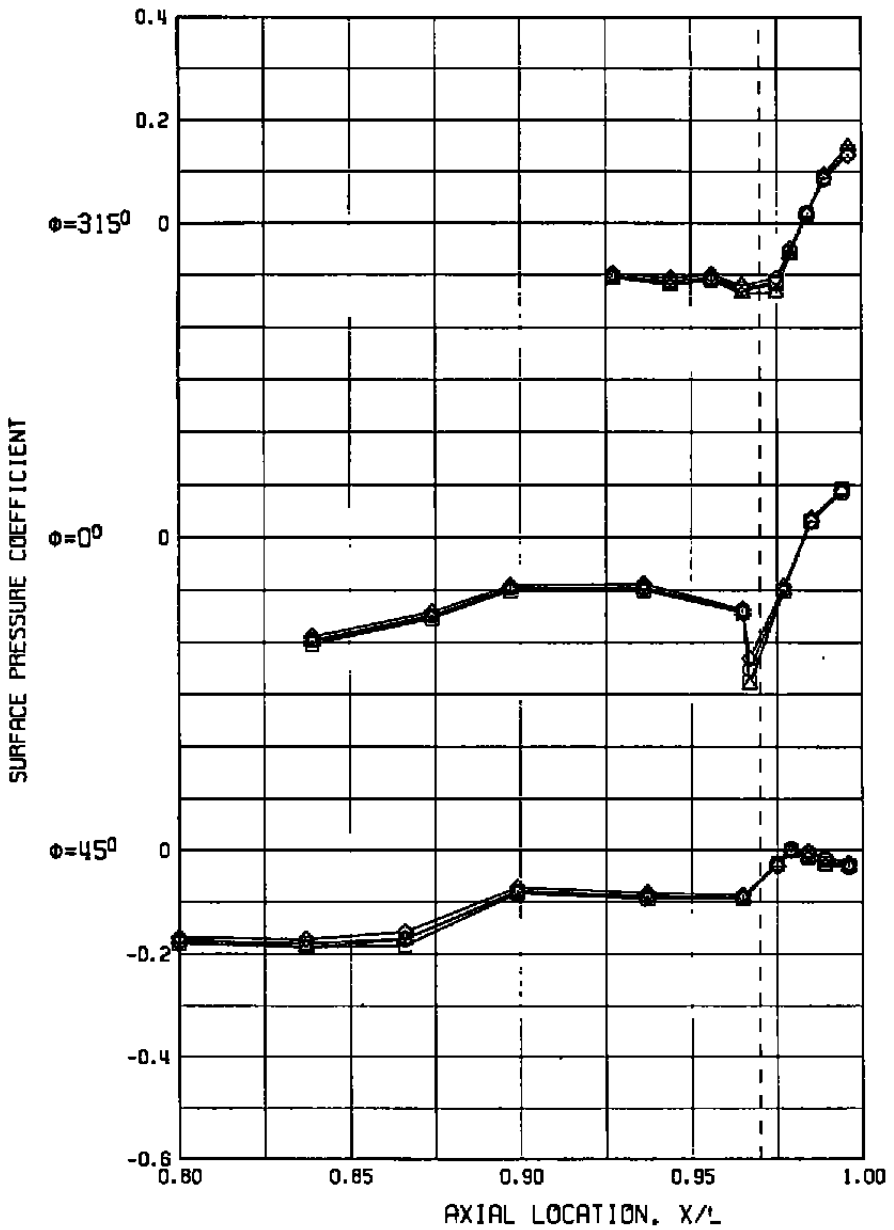

a. Lee-side pressures

Figure 15. Effect of Reynolds number on the 0.1-scale model surface pressure distribution at M = 0.6, A8 = 200 in.², $\alpha \sim 4$ deg, and NPR ~ 3.4.

SYM	M	Re_{ℓ}	AB	NPR	α	δ_H	CATPW	PN/PT
◇	0.60	9.0	200.	3.0	4.2	0.0	0.0021	24.02
○	0.60	14.9	200.	3.0	4.2	0.0	0.0024	26.02
□	0.60	22.3	200.	3.0	4.2	0.0	0.0025	29.04
△	0.60	29.7	200.	3.0	4.0	0.0	0.0025	142.04

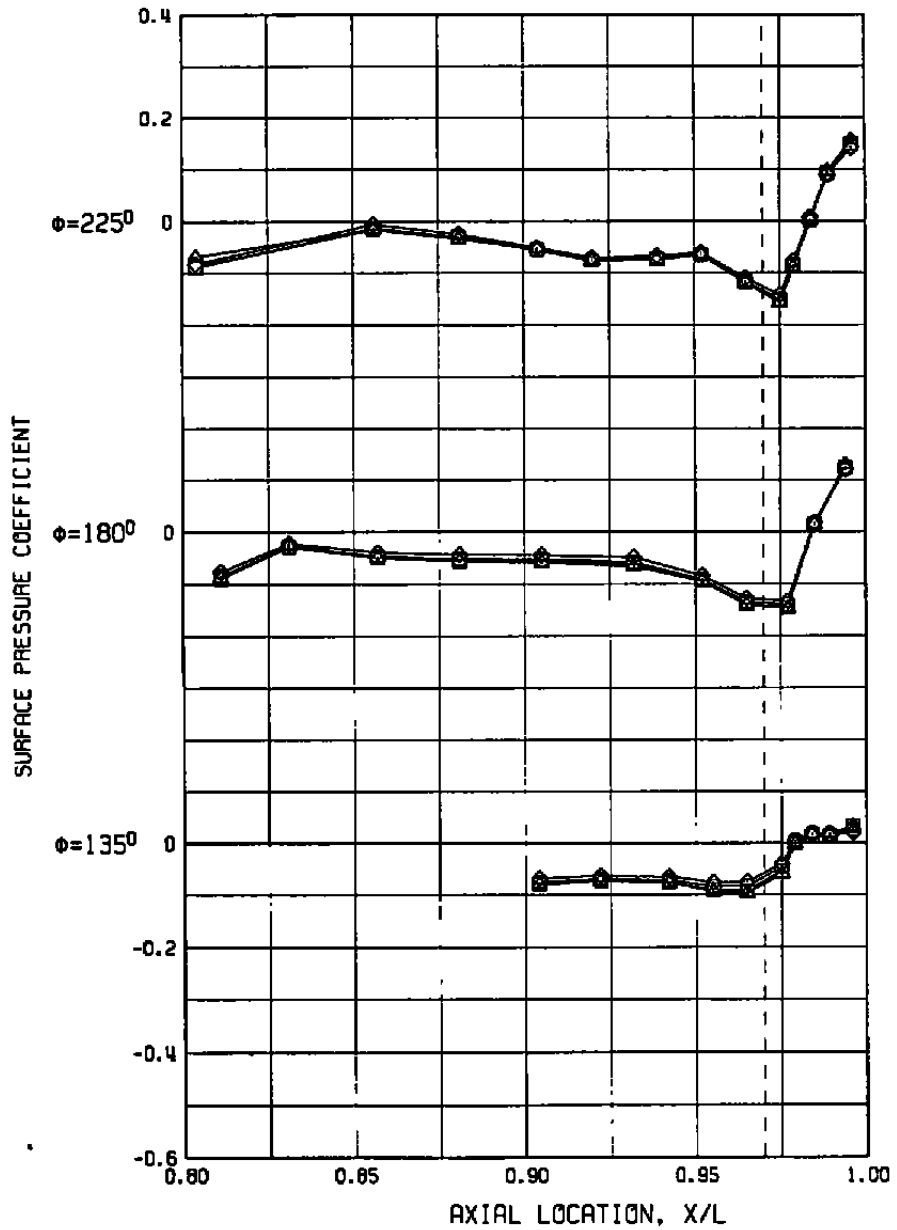

b. Windward-side pressures
Figure 15. Concluded.

SYM	M	Re_ℓ	A8	NPR	α	δ_H	CATPW	PN/PT
◇	0.90	9.0	200.	3.4	4.0	0.0	0.0007	139.04
○	0.90	14.9	200.	3.5	4.1	0.0	0.0010	35.05
□	0.90	22.2	200.	3.4	4.1	0.0	0.0010	31.03
△	0.90	29.7	200.	3.4	4.1	0.0	0.0012	30.04

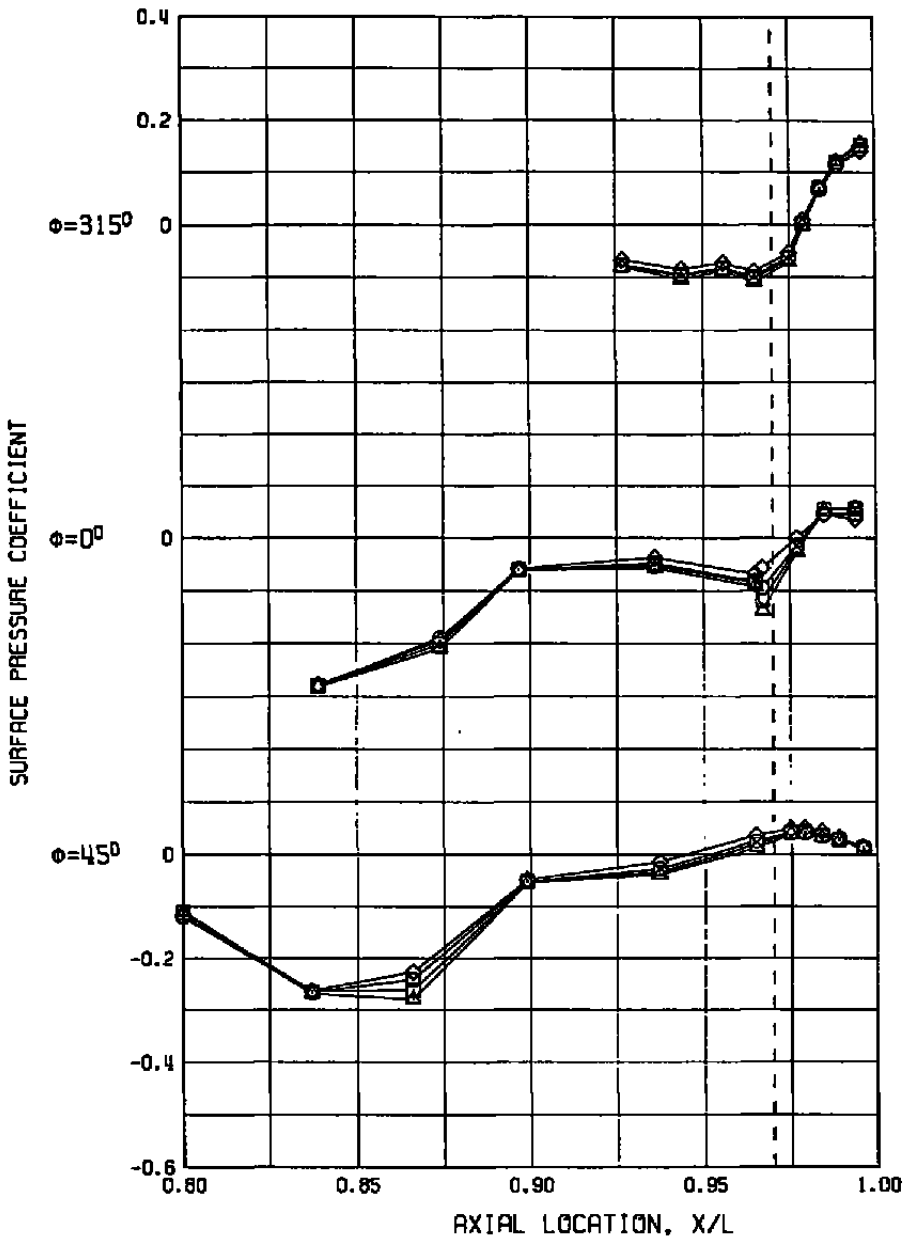

a. Lee-side pressures

Figure 16. Effect of Reynolds number on the 0.1-scale model surface pressure distribution at M = 0.9, A8 = 200 in.^{2}, $\alpha \sim 4$ deg, and NPR ~ 3.4.

SYM	M	Re_ℓ	AB	NPR	α	δ_H	CATPW	PN/PT
◇	0.90	9.0	200.	3.4	4.0	0.0	0.0007	139.04
⊙	0.90	14.9	200.	3.5	4.1	0.0	0.0010	35.05
⊡	0.90	22.2	200.	3.4	4.1	0.0	0.0010	31.03
△	0.90	29.7	200.	3.4	4.1	0.0	0.0012	30.04

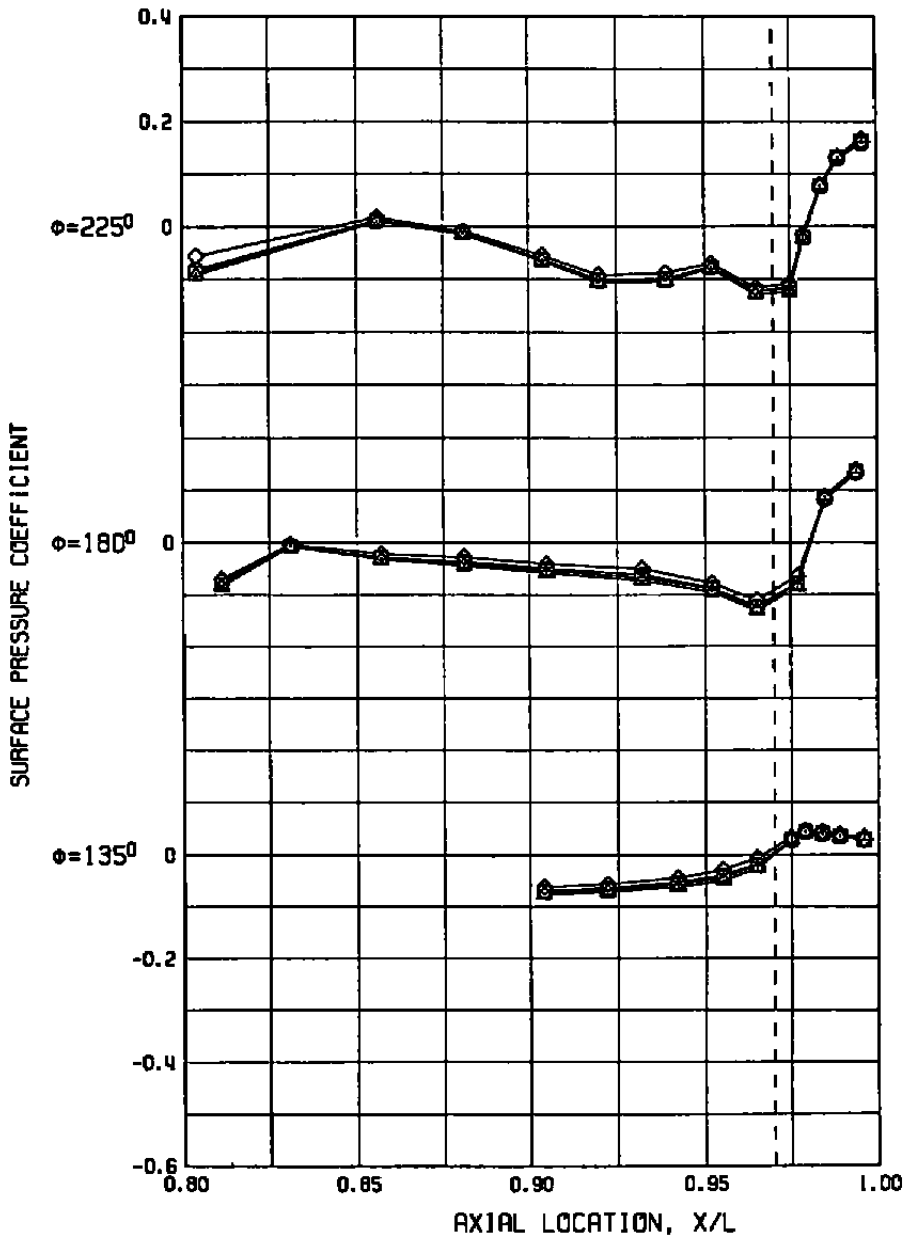

b. Windward-side pressures

Figure 16. Concluded.

SYM	M	Re_ℓ	A8	NPR	α	δ_H	CATPW	PN/PT
◇	0.90	9.0	286.	5.0	4.2	0.0	0.0009	59.03
○	0.90	14.9	286.	5.1	4.2	0.0	0.0011	62.01
□	0.90	22.3	286.	5.1	4.2	0.0	0.0012	74.04
△	0.90	29.7	286.	5.0	4.2	0.0	0.0012	75.02

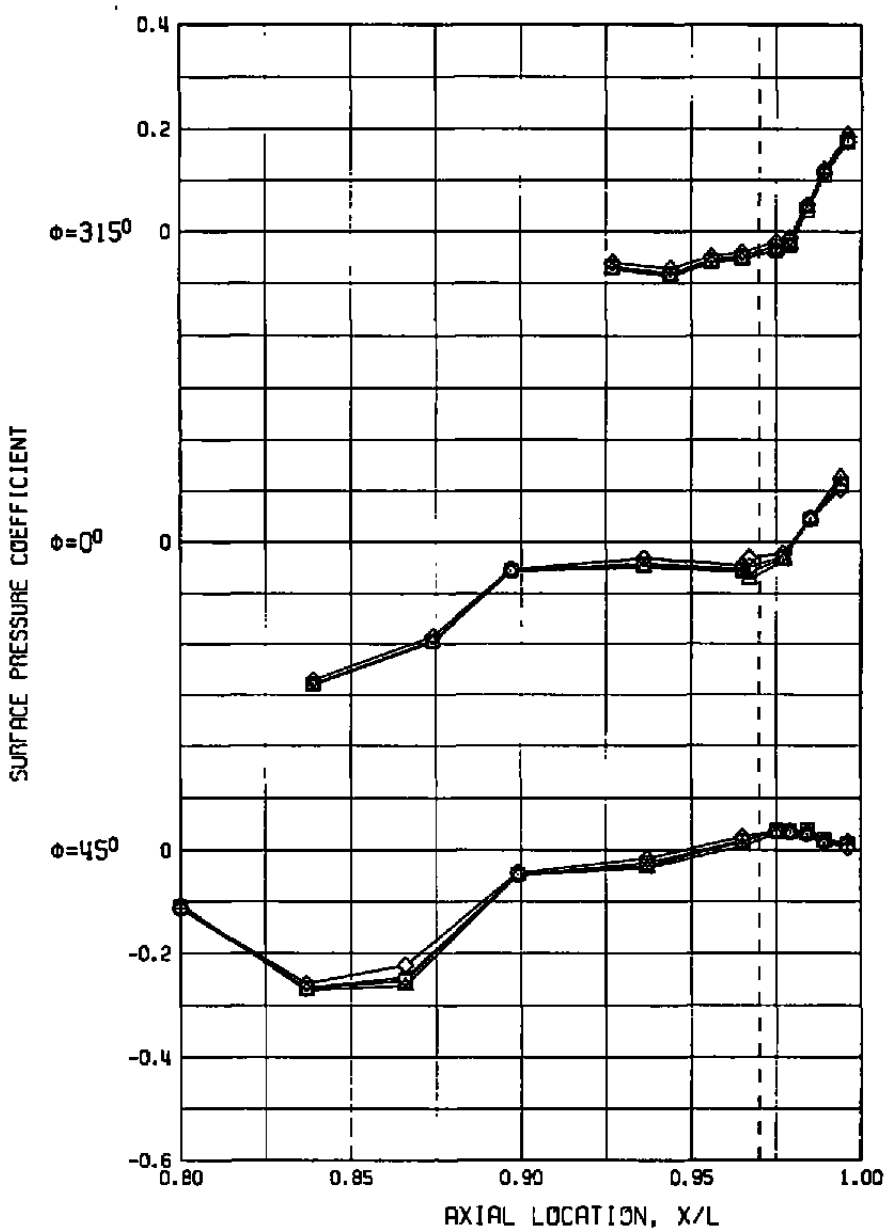

a. Lee-side pressures

Figure 17. Effect of Reynolds number on the 0.1-scale model surface pressure distribution at M = 0.9, A8 = 286 in.^{2}, $\alpha \sim 4$ deg, and NPR ~ 5.0.

SYM	M	Re_ℓ	AB	NPR	α	δ_H	CATPW	PN/PT
◇	0.90	9.0	286.	5.0	4.2	0.0	0.0009	59.03
⊙	0.90	14.9	286.	5.1	4.2	0.0	0.0011	62.01
□	0.90	22.3	286.	5.1	4.2	0.0	0.0012	74.04
△	0.90	29.7	286.	5.0	4.2	0.0	0.0012	75.02

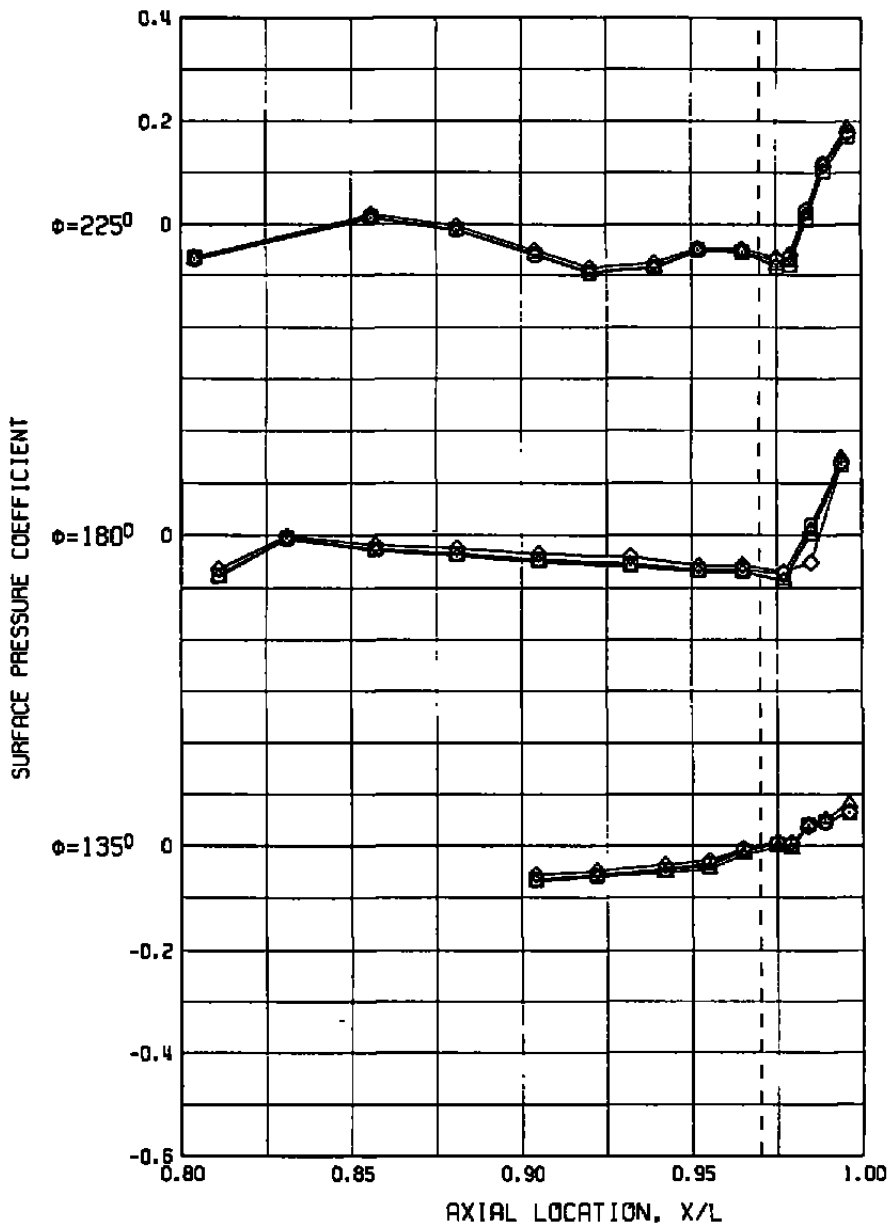

b. Windward-side pressures

Figure 17. Concluded.

SYM	M	Re_ℓ	A8	NPR	α	δ_H	CATPW	PN/PT
◇	1.20	9.0	200.	3.4	4.0	-2.0	0.0105	176.04
○	1.20	14.8	200.	3.4	4.1	-2.0	0.0109	172.01
□	1.20	22.3	200.	3.5	4.0	-2.0	0.0111	175.01
△	1.20	25.4	200.	3.4	4.1	-2.0	0.0112	174.03

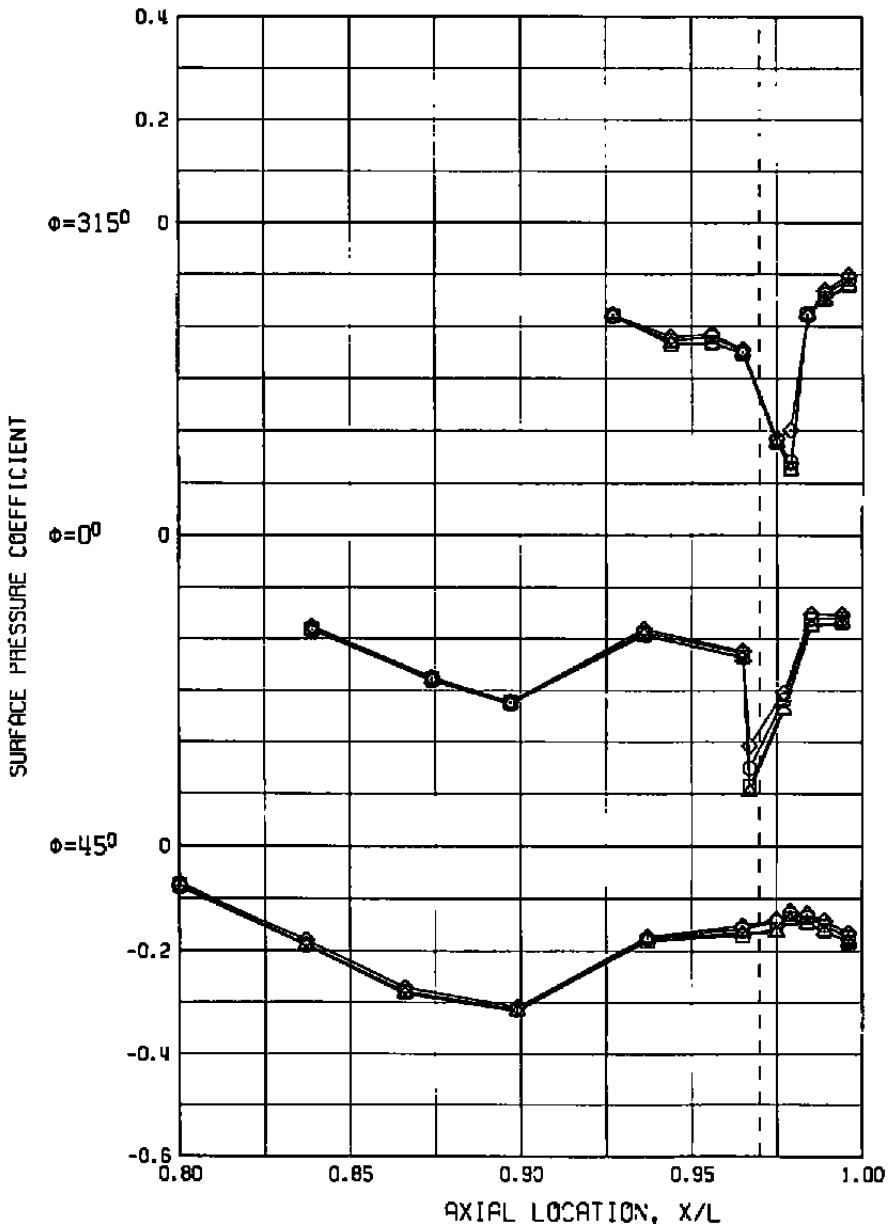

a. Lee-side pressures

Figure 18. Effect of Reynolds number on the 0.1-scale model surface pressure distribution at M = 1.2, A8 - 200 in.², α ~ 4 deg, and NPR ~ 3.4.

SYM	M	Re_ℓ	AB	NPR	α	δ_H	CATPW	PN/PT
◇	1.20	9.0	200.	3.4	4.0	-2.0	0.0105	176.04
⊙	1.20	14.8	200.	3.4	4.1	-2.0	0.0109	172.01
□	1.20	22.3	200.	3.5	4.0	-2.0	0.0111	175.01
△	1.20	25.4	200.	3.4	4.1	-2.0	0.0112	174.03

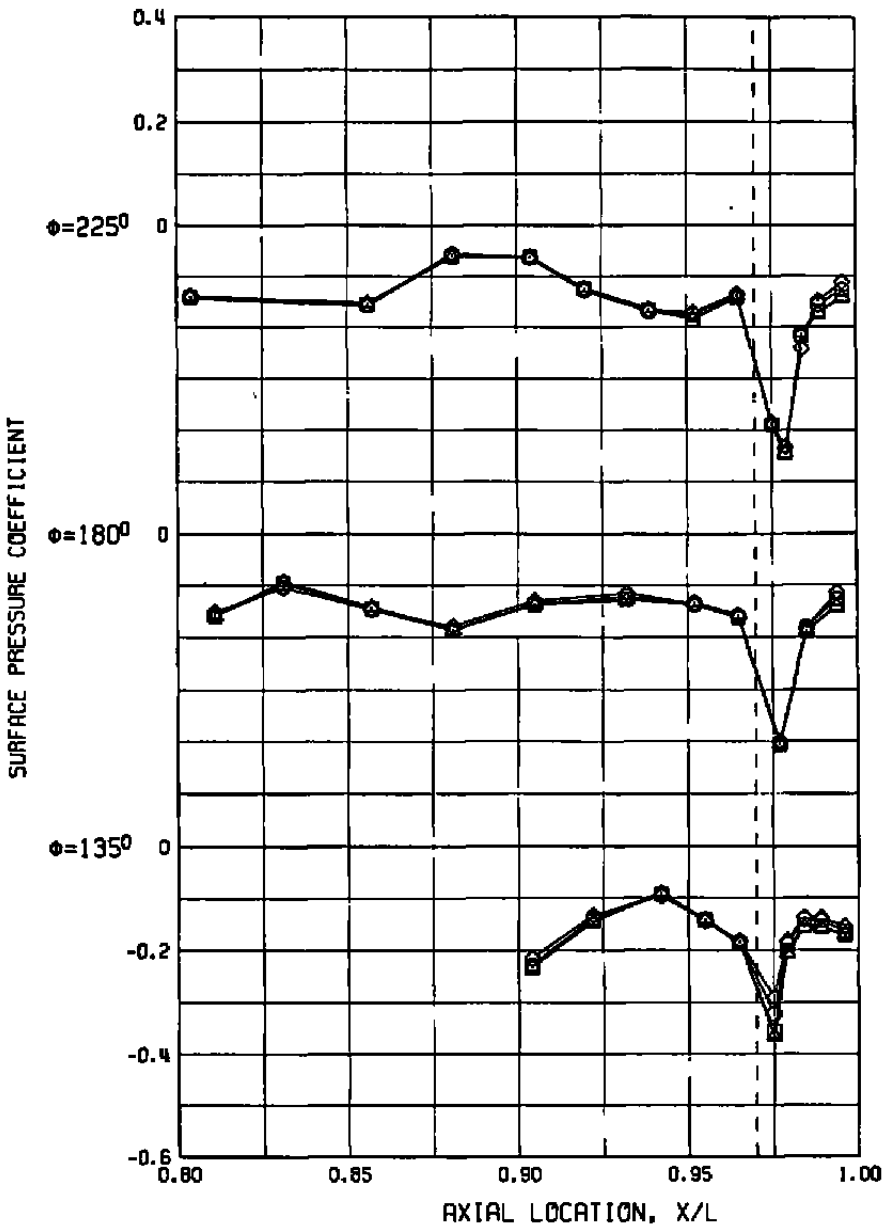

b. Windward-side pressures
Figure 18. Concluded.

SYM	M	Re_ℓ	AB	NPR	α	δ_H	CATPW	PN/PT
○	0.60	29.8	200.	3.4	4.1	0.0	0.0023	511.04
□	0.60	44.7	200.	3.4	4.1	0.0	0.0019	597.04
△	0.60	59.6	200.	3.4	4.2	0.0	0.0020	594.05

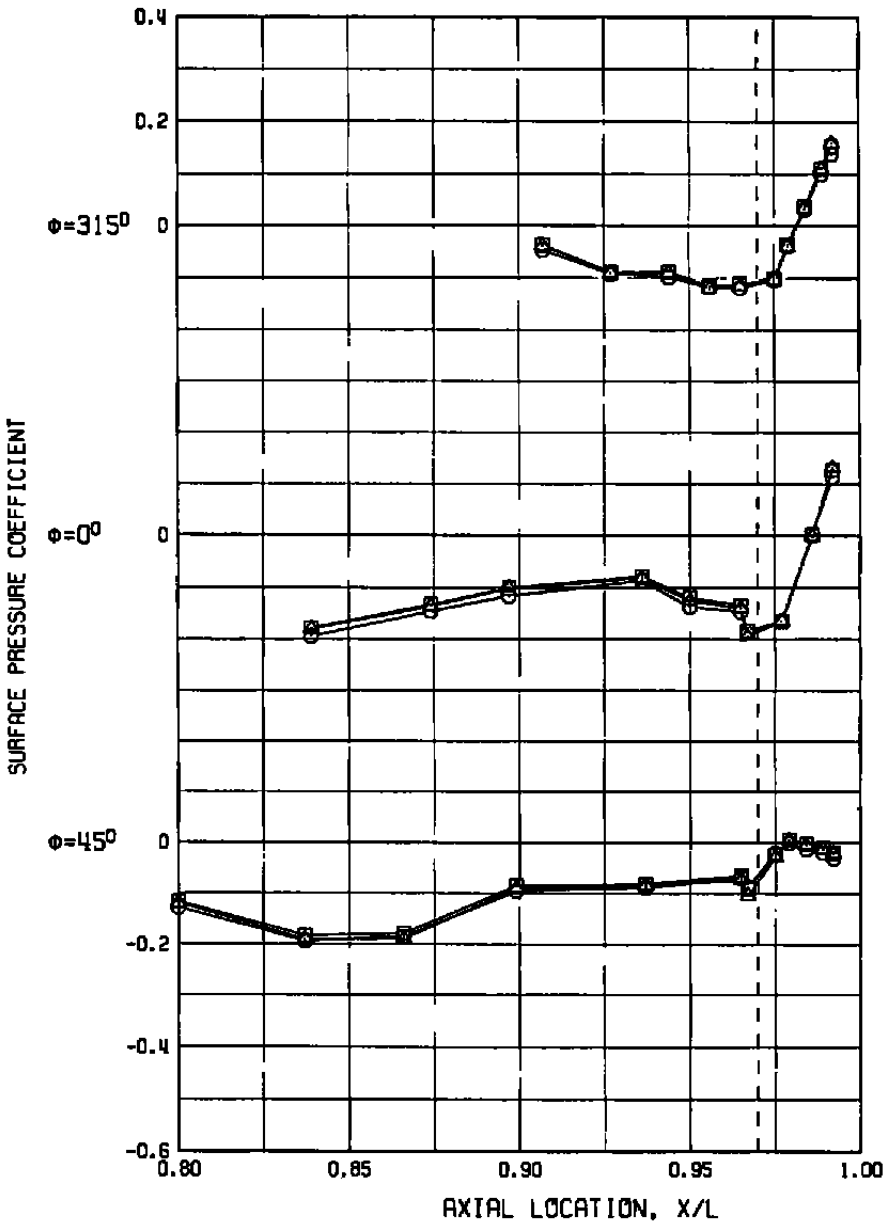

a. Lee-side pressures

Figure 19. Effect of Reynolds number on the 0.2-scale model surface pressure distribution at M = 0.6, A8 = 200 in.², $\alpha \sim 4$ deg, and NPR ~ 3.4.

SYM	M	Re_ℓ	AB	NPR	α	δ_H	CATPW	PN/PT
○	0.60	29.8	200.	3.4	4.1	0.0	0.0023	511.04
□	0.60	44.7	200.	3.4	4.1	0.0	0.0019	597.04
△	0.60	59.6	200.	3.4	4.2	0.0	0.0020	594.05

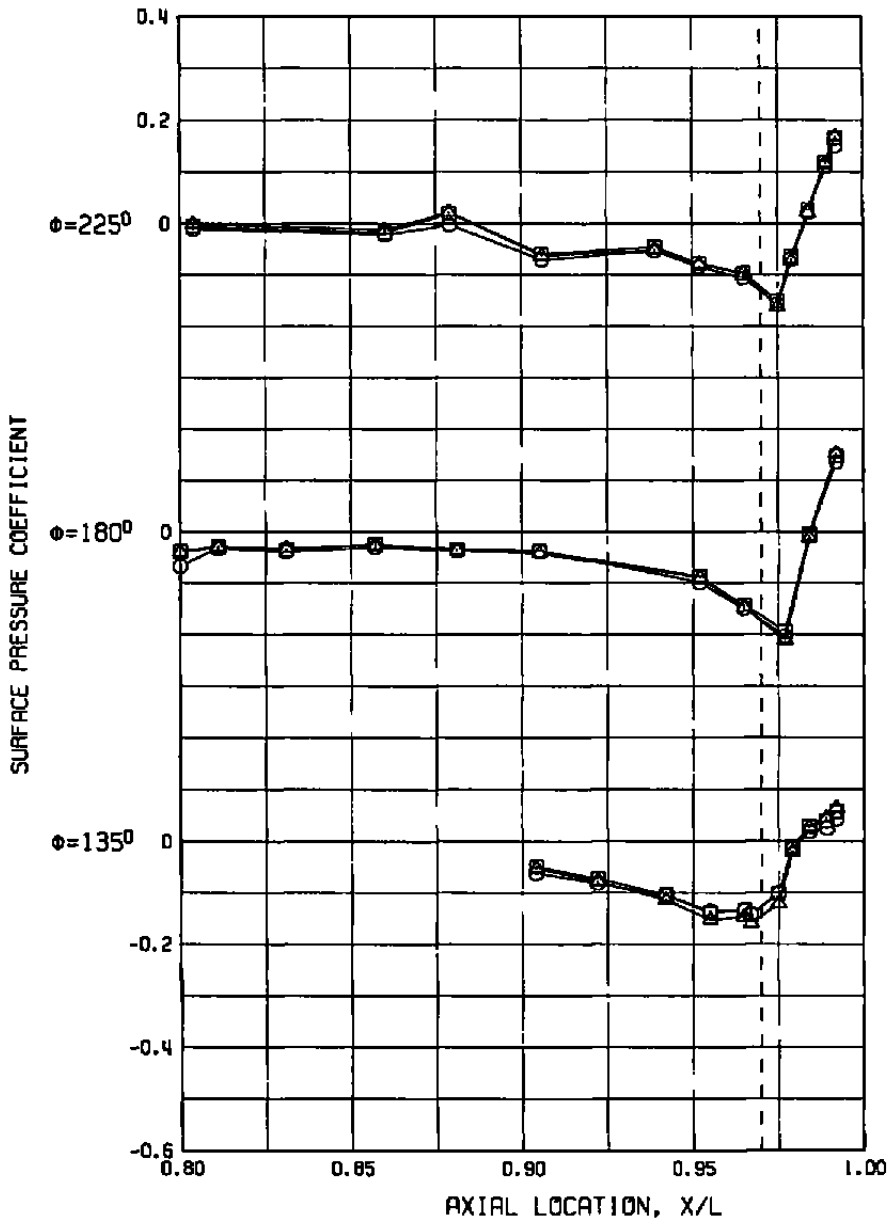

b. Windward-side pressures
Figure 19. Concluded.

SYM	M	Re_{ℓ}	A8	NPR	α	δ_H	CATPH	PN/PT
◇	0.90	14.9	200.	3.4	4.1	0.0	0.0017	521.03
⊙	0.90	29.9	200.	3.4	4.1	0.0	0.0016	522.06
□	0.90	44.5	200.	3.4	4.1	0.0	0.0014	616.03
△	0.90	58.2	200.	2.7	4.1	0.0	0.0014	602.03

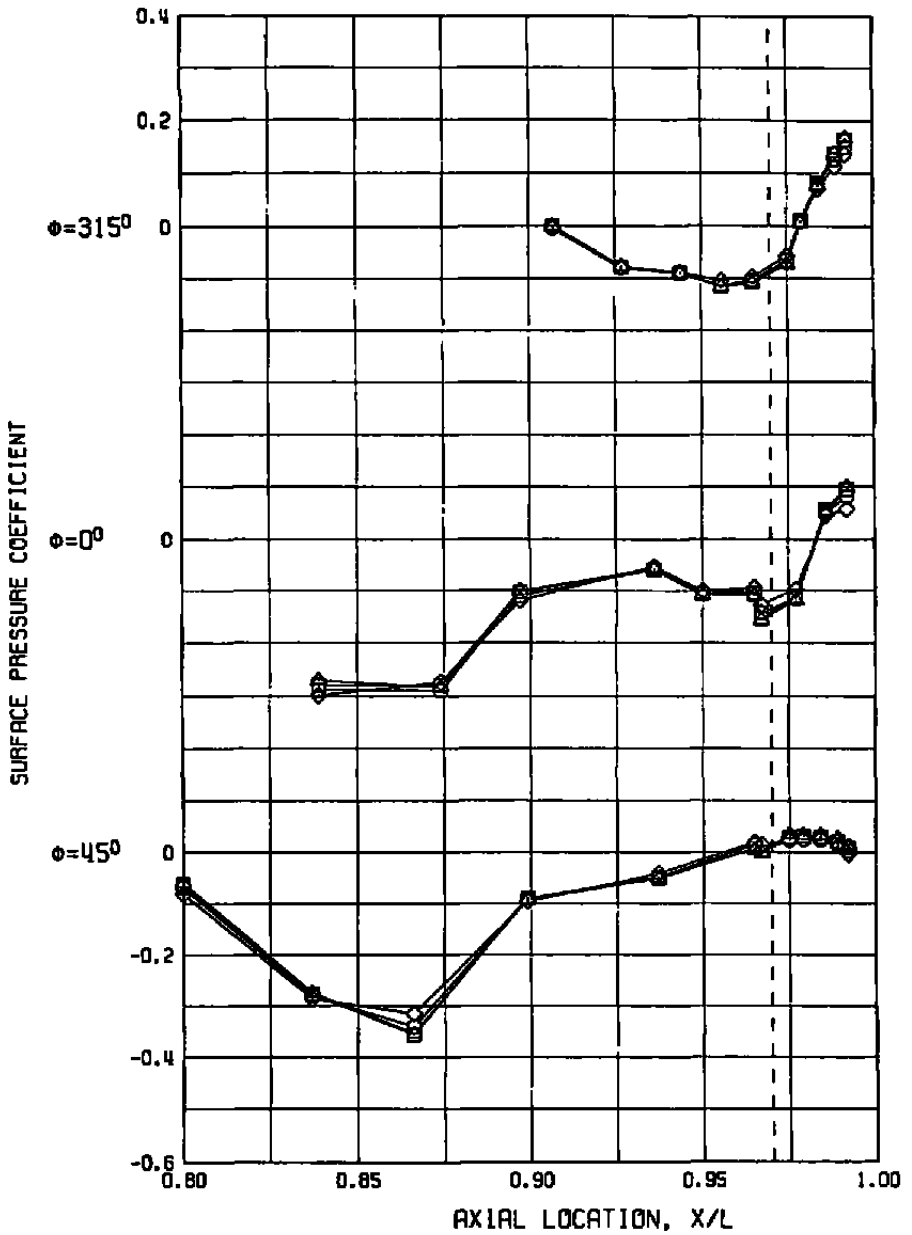

a. Lee-side pressures

Figure 20. Effect of Reynolds number on the 0.2-scale model surface pressure distribution at M = 0.9, A8 = 200 in.^{2}, $\alpha \sim 4$ deg, and NPR ~ 3.0.

SYM	M	Re_{ℓ}	AB	NPR	α	δ_H	CATPW	PN/PT
◇	0.90	14.9	200.	3.4	4.1	0.0	0.0017	521.03
⊙	0.90	29.9	200.	3.4	4.1	0.0	0.0016	522.06
⊡	0.90	44.5	200.	3.4	4.1	0.0	0.0014	616.03
△	0.90	58.2	200.	2.7	4.1	0.0	0.0014	602.03

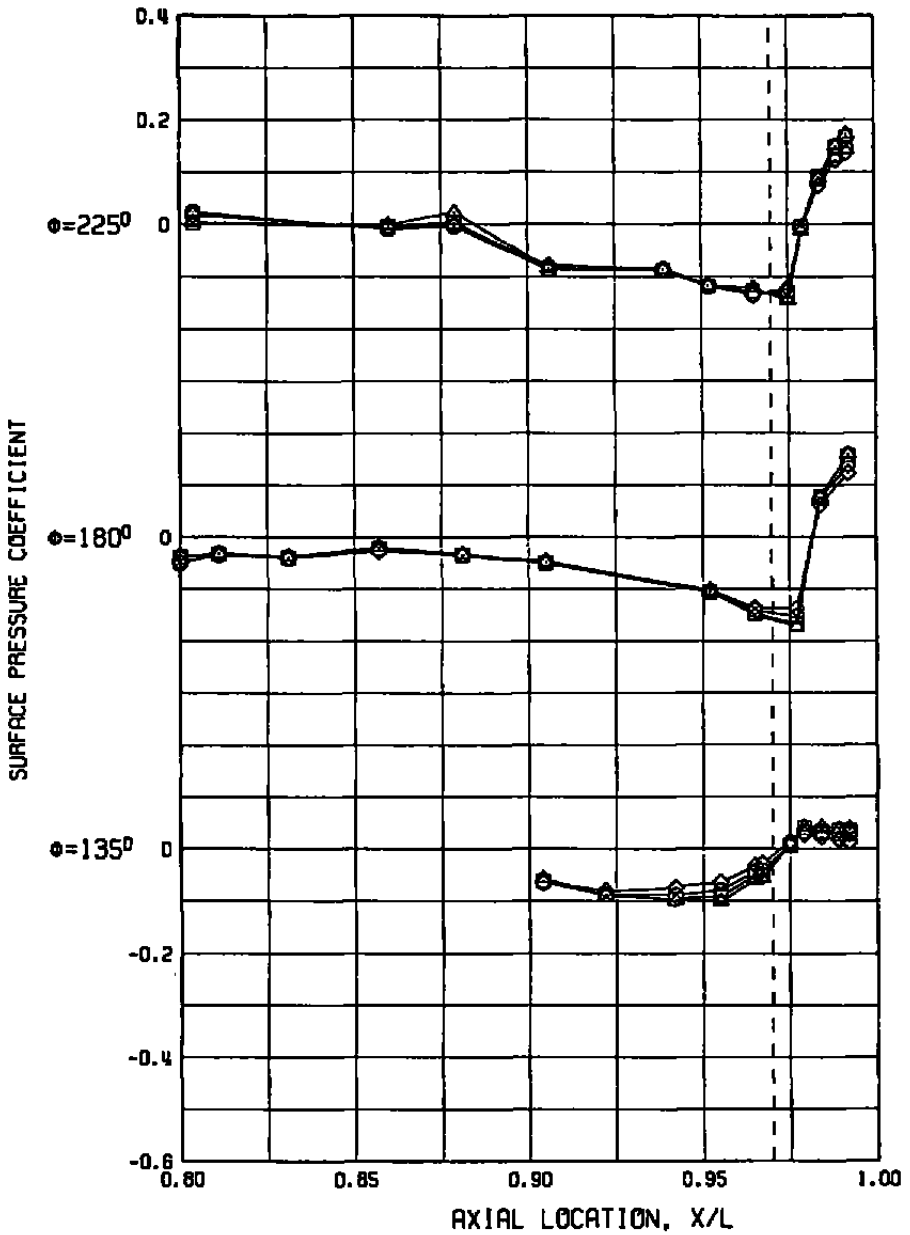

b. Windward-side pressures

Figure 20. Concluded.

SYM	M	Re_{ℓ}	AB	NPR	α	δ_H	CATPW	PN/PT
◇	0.90	14.7	300.	5.1	4.1	0.0	0.0018	695.03
○	0.90	29.9	300.	5.0	4.1	0.0	0.0011	694.03
□	0.90	44.7	300.	5.1	4.1	0.0	0.0011	698.02
△	0.90	55.3	300.	5.0	4.0	0.0	0.0011	700.03

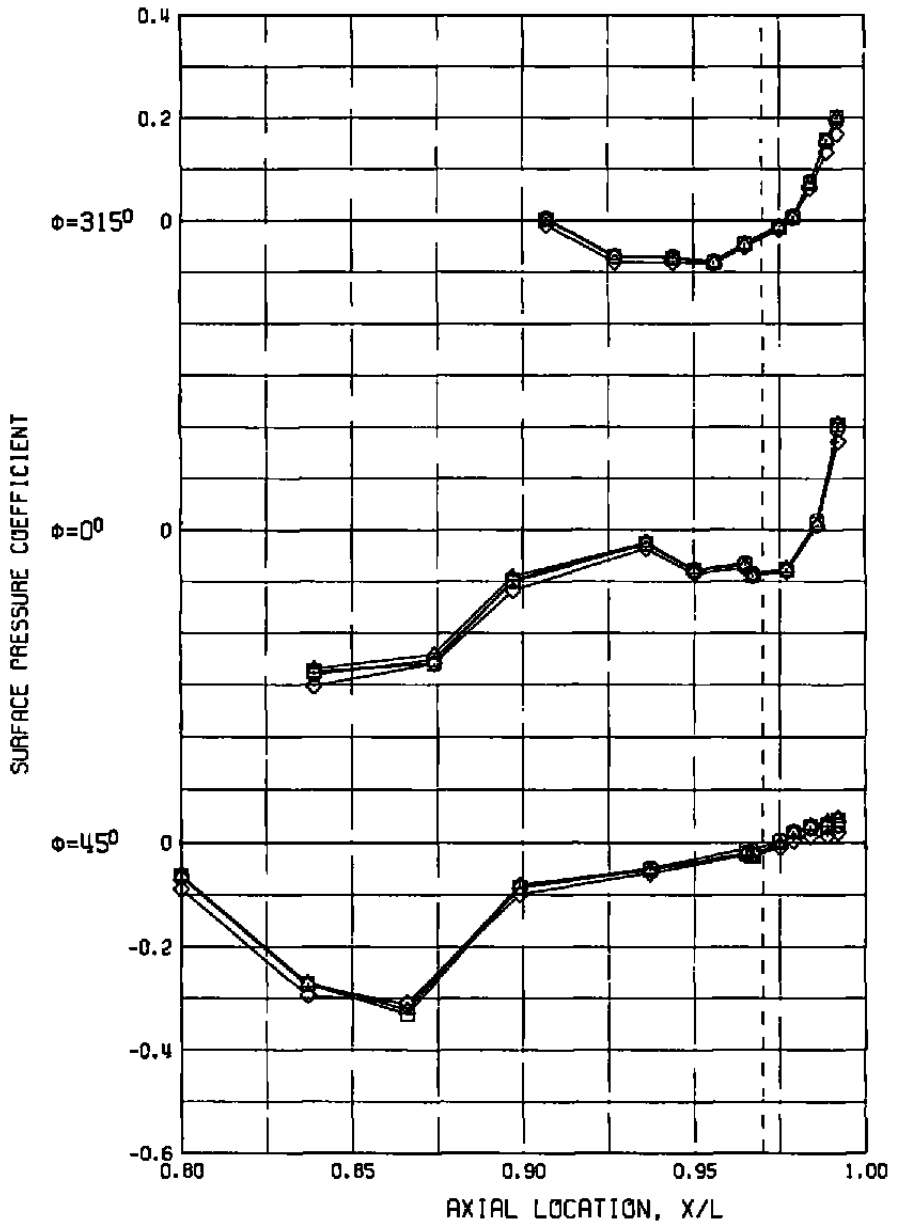

a. Lee-side pressures

Figure 21. Effect of Reynolds number on the 0.2-scale model surface pressure distribution at M = 0.9, A8 = 300 in.^{2}, $\alpha \sim 4$ deg, and NPR ~ 5.0.

SYM	M	Re_ℓ	AB	NPR	α	δ_H	CATPW	PN/PT
◇	0.90	14.7	300.	5.1	4.1	0.0	0.0018	695.03
○	0.90	29.9	300.	5.0	4.1	0.0	0.0011	694.03
□	0.90	44.7	300.	5.1	4.1	0.0	0.0011	698.02
△	0.90	55.3	300.	5.0	4.0	0.0	0.0011	700.03

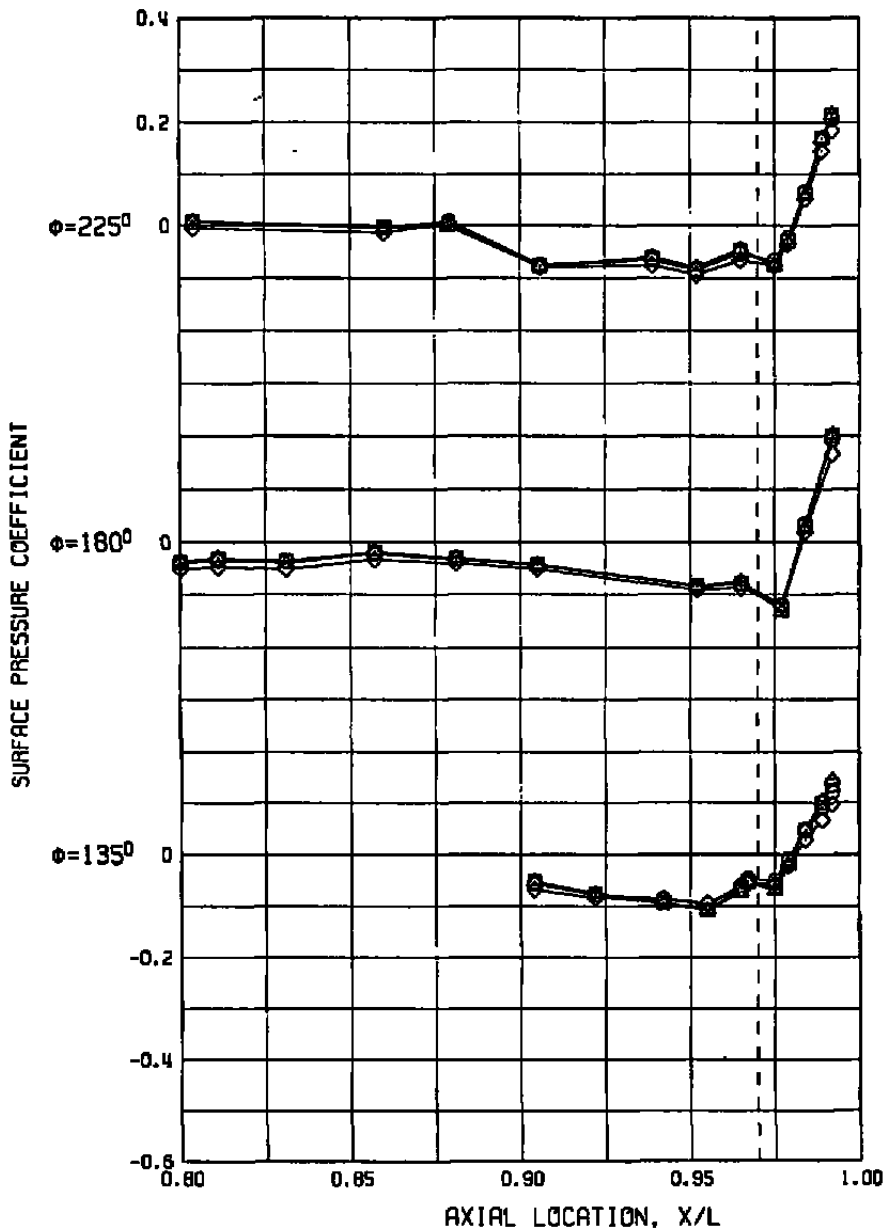

b. Windward-side pressures

Figure 21. Concluded.

SYM	M	Re_ℓ	A8	NPR	α	δ_H	CATPW	PN/PT
◇	1.20	14.9	200.	3.3	4.0	-2.0	0.0119	560.02
○	1.20	29.7	200.	3.4	4.0	-2.0	0.0128	562.02
□	1.20	44.5	200.	3.4	4.0	-2.0	0.0127	563.01
△	1.20	51.0	200.	3.4	4.0	-2.0	0.0130	564.04

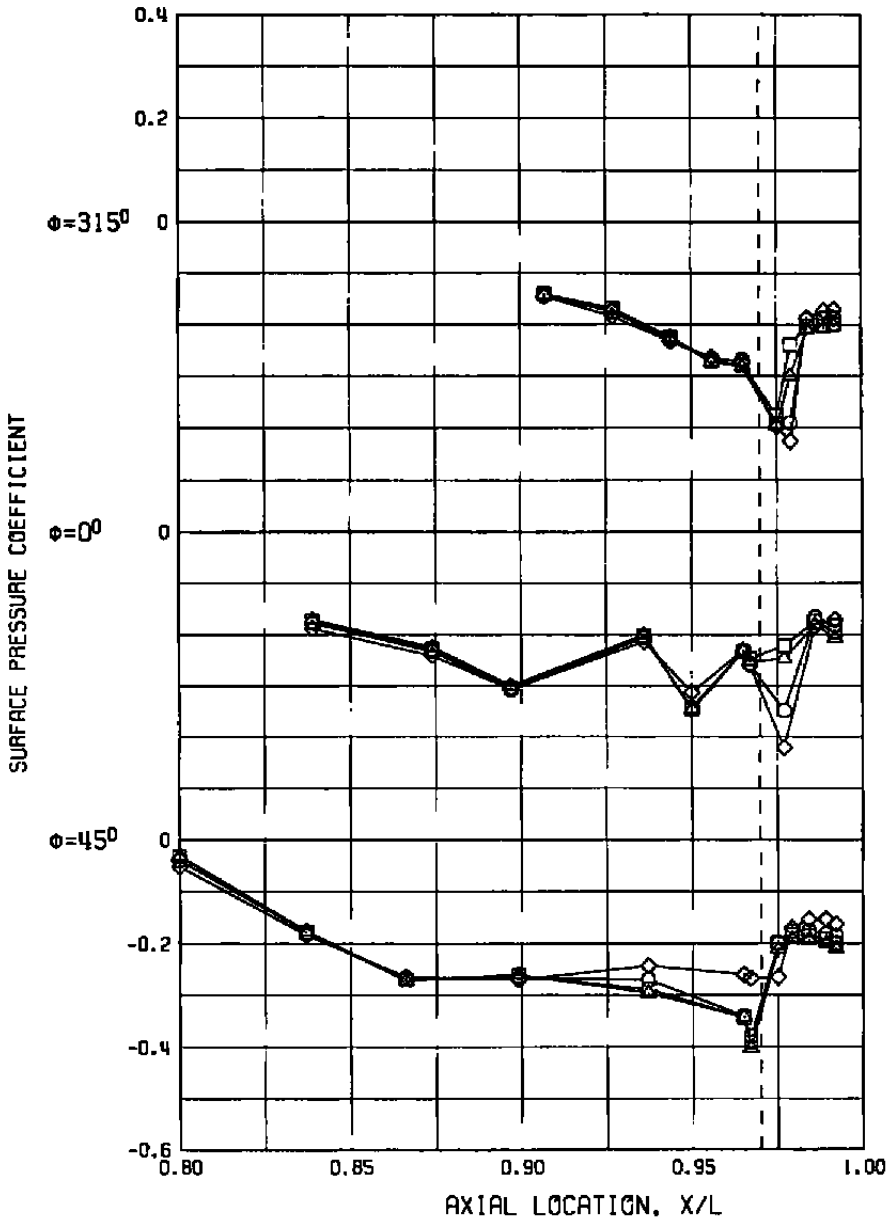

a. Lee-side pressures

Figure 22. Effect of Reynolds number on the 0.2-scale model surface pressure distribution at M = 1.2, A8 = 200 in.², $\alpha \sim 4$ deg, and NPR ~ 3.4.

SYM	M	Re_ℓ	AB	NPR	α	δ_H	CATPW	PN/PT
◇	1.20	14.9	200.	3.3	4.0	-2.0	0.0119	560.02
○	1.20	29.7	200.	3.4	4.0	-2.0	0.0128	562.02
□	1.20	44.5	200.	3.4	4.0	-2.0	0.0127	563.01
△	1.20	51.0	200.	3.4	4.0	-2.0	0.0130	564.04

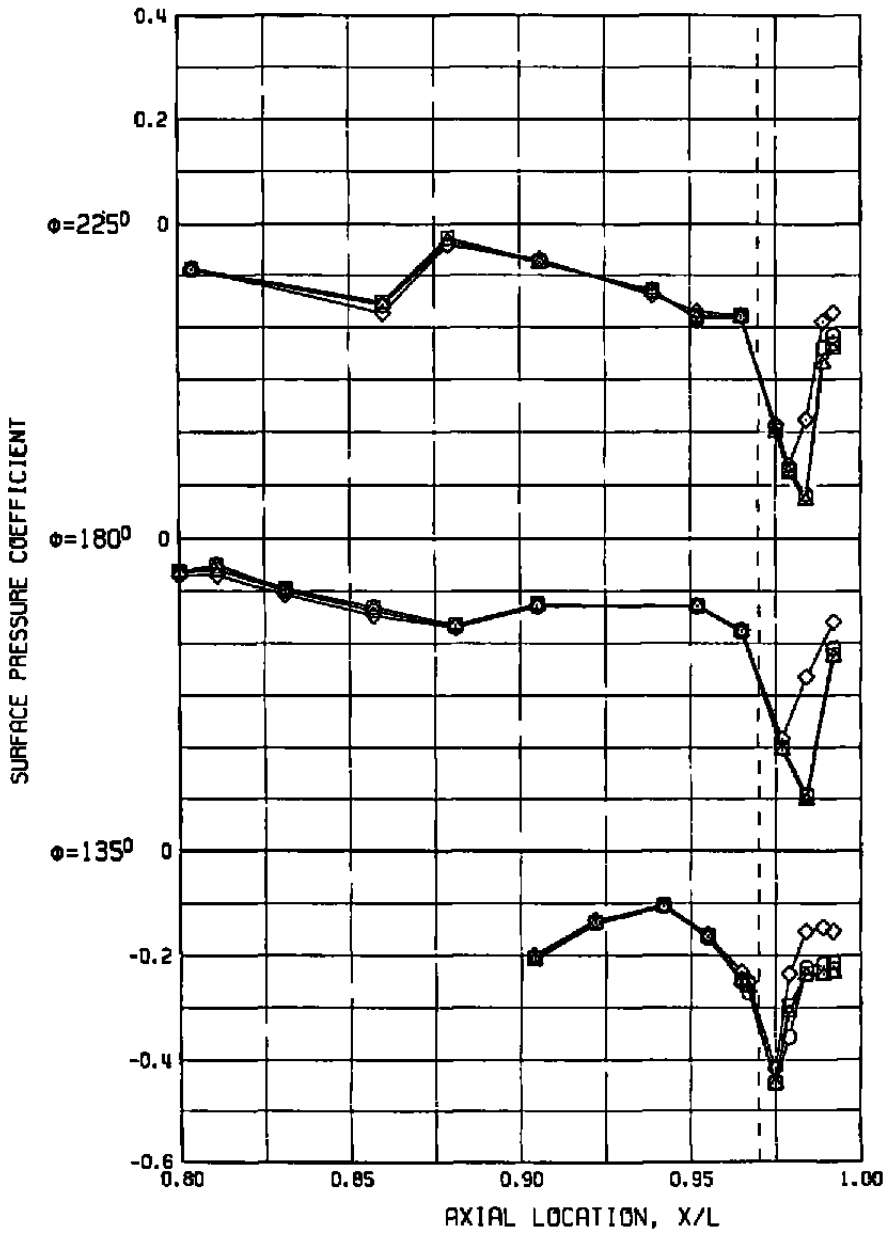

b. Windward-side pressures
Figure 22. Concluded.

SYM	M	Re_ℓ	A8	NPR	α	δ_H	CATPW	PN/PT
◇	0.60	58.3	204.	2.7	5.8	-1.4	0.0020	450.03
○	0.61	108.6	205.	2.5	6.6	-2.0	0.0022	423.03
△	0.61	164.3	204.	2.2	4.6	-1.5	0.0023	452.03

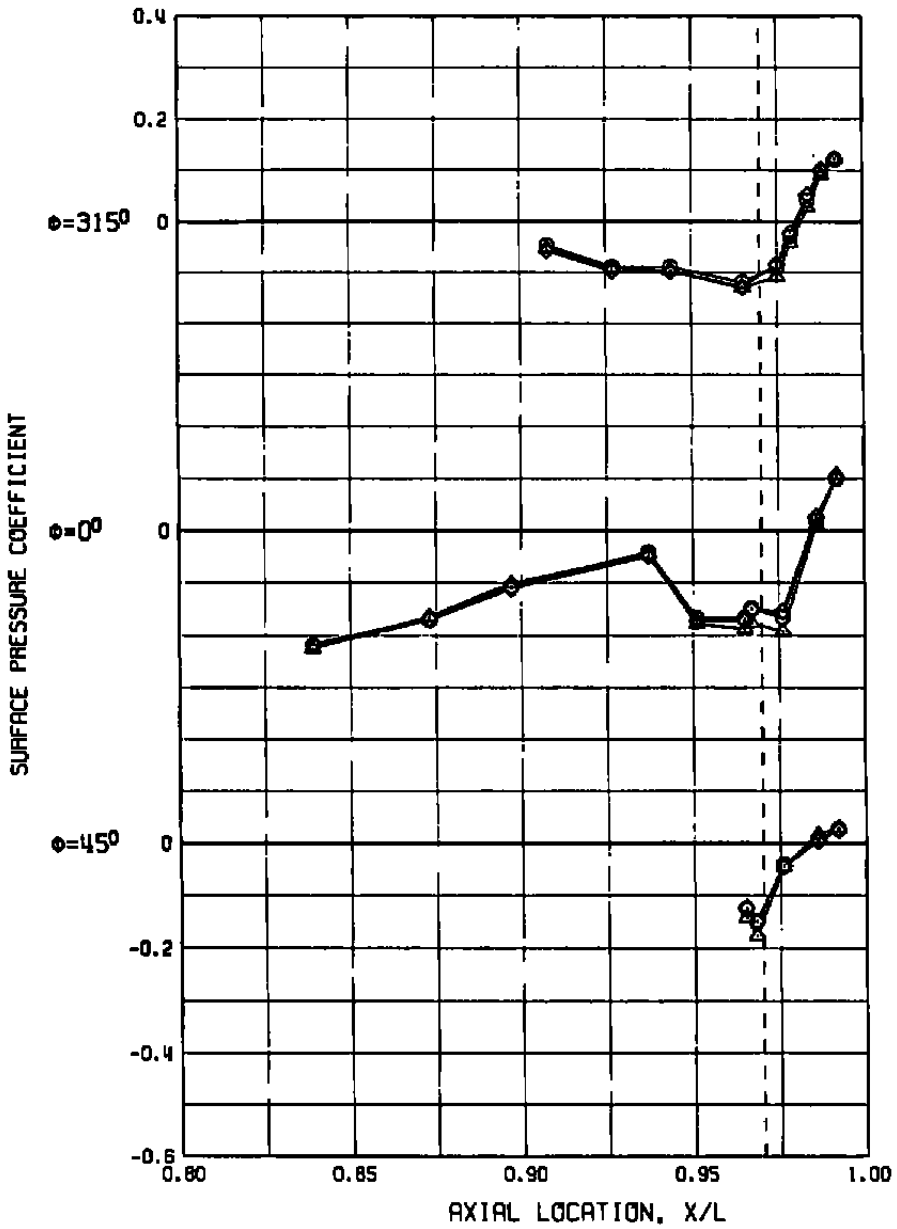

a. Lee-side pressures

Figure 23. Effect of Reynolds number on the full-scale flight vehicle surface pressure distribution at M = 0.6, A8 = 200 in.², α ~ 6 deg, and NPR ~ 2.5.

SYM	M	Re_ℓ	AB	NPR	α	δ_H	CATPW	PN/PT
◇	0.60	58.3	204.	2.7	5.8	-1.4	0.0020	450.03
○	0.61	108.6	205.	2.5	6.6	-2.0	0.0022	423.03
△	0.61	164.3	204.	2.2	4.6	-1.5	0.0023	452.03

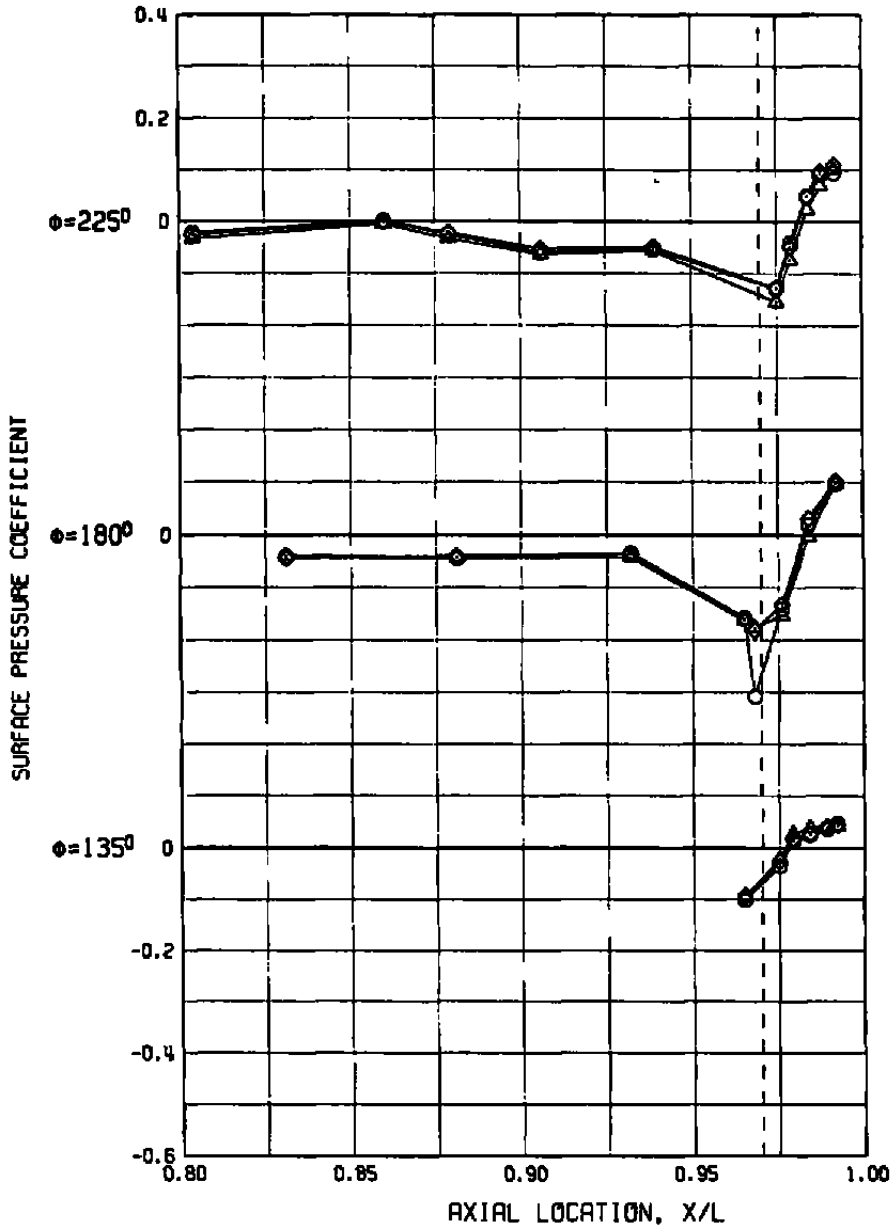

b. Windward-side pressures
Figure 23. Concluded.

SYM	M	Re_ℓ	AB	NPR	α	δ_H	CATPW	PN/PT
⊡	0.90	132.5	205.	3.1	1.5	-0.9	0.0023	402.03
□	0.90	132.5	204.	3.4	1.4	-0.9	0.0019	444.03
◁	0.91	190.8	204.	3.2	0.9	-0.9	0.0018	409.03
▽	0.90	243.8	205.	3.1	0.8	-0.9	0.0020	413.03

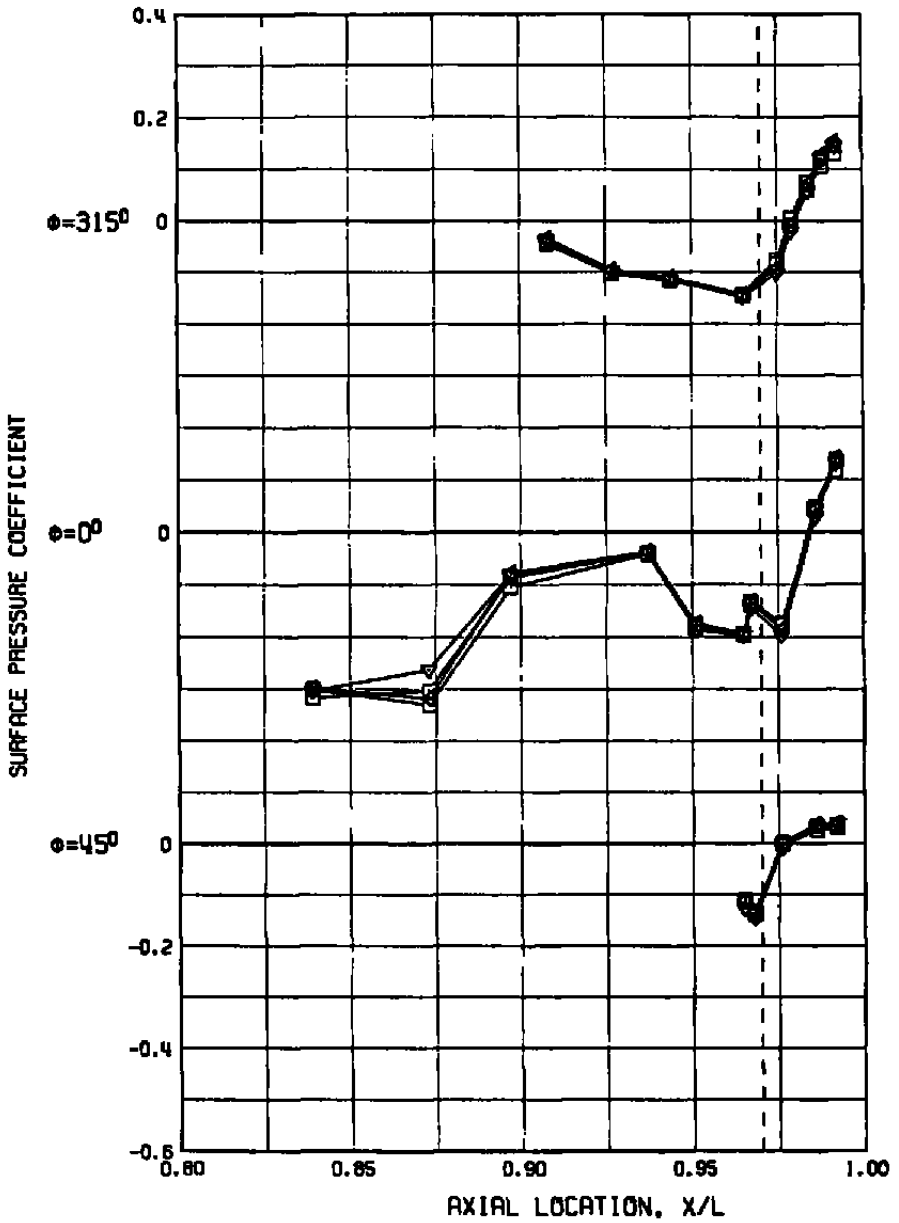

a. Lee-side pressures

Figure 24. Effect of Reynolds number on the full-scale flight vehicle surface pressure distribution at M = 0.9, A8 = 200 in.², $\alpha \sim 1$ deg, and NPR ~ 3.0.

SYM	M	Re_ℓ	AB	NPR	α	δ_H	CATPW	PN/PT
⊡	0.90	132.5	205.	3.1	1.5	-0.9	0.0023	402.03
□	0.90	132.5	204.	3.4	1.4	-0.9	0.0019	444.03
◁	0.91	190.8	204.	3.2	0.9	-0.9	0.0018	409.03
▽	0.90	243.8	205.	3.1	0.8	-0.9	0.0020	413.03

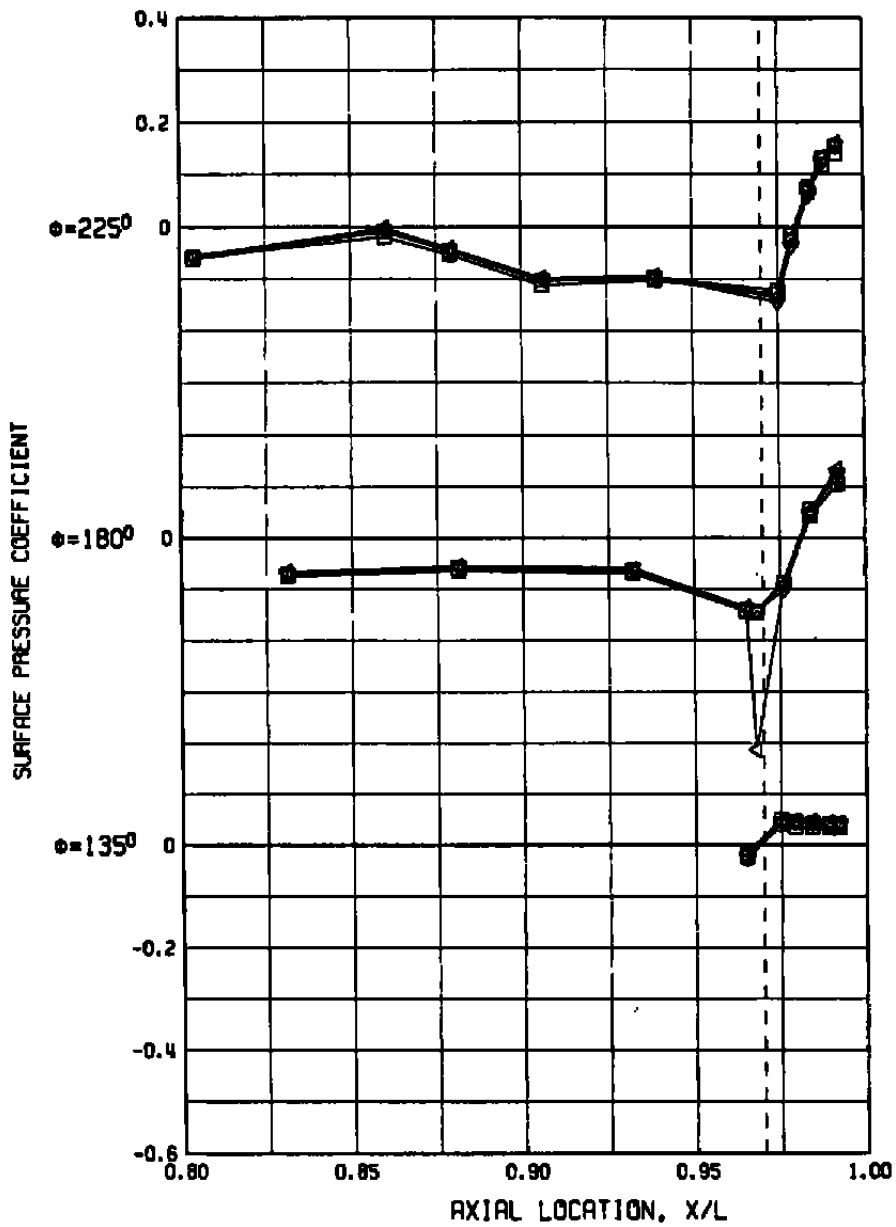

b. Windward-side pressures

Figure 24. Concluded.

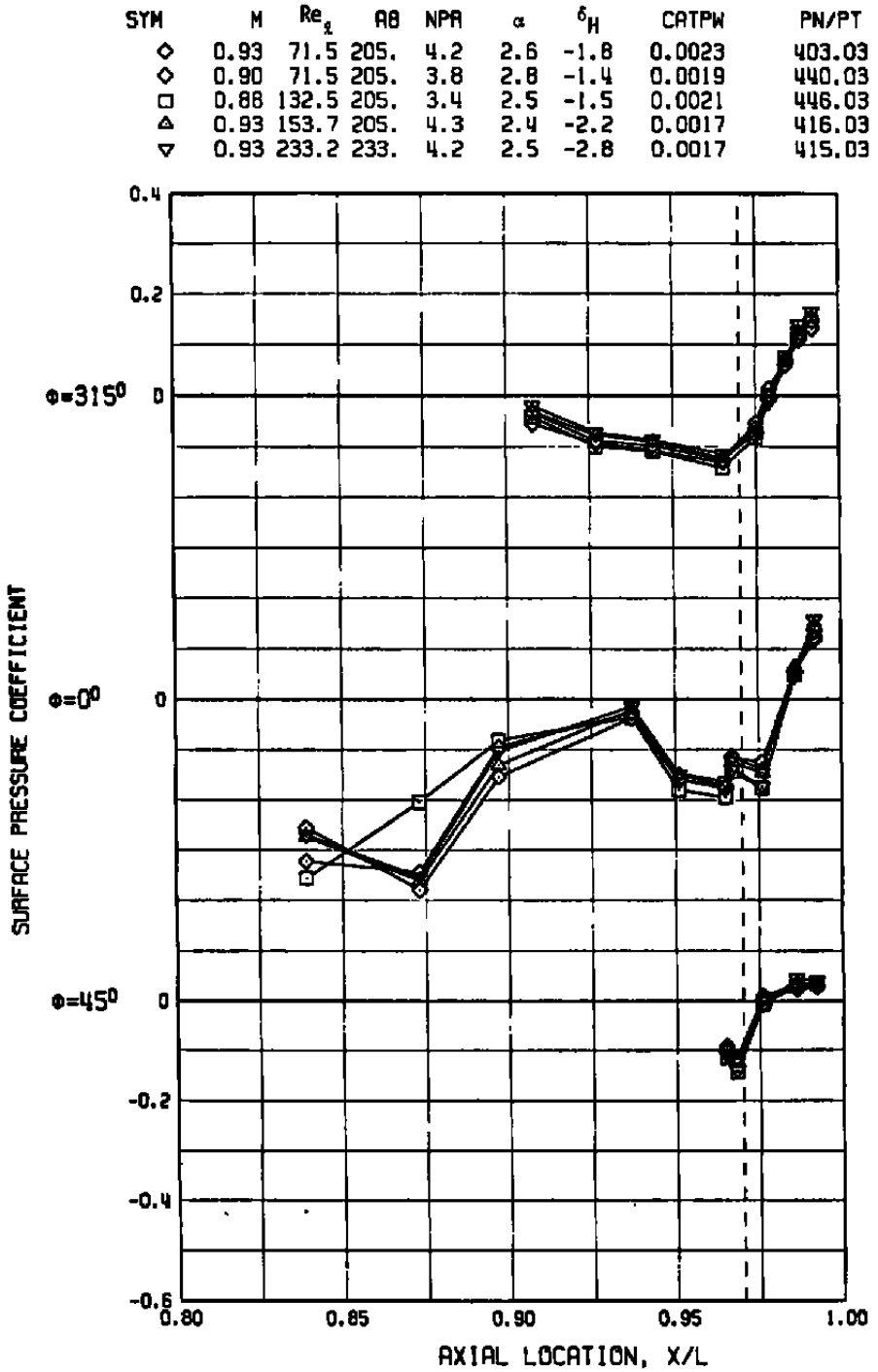

a. Lee-side pressures

Figure 25. Effect of Reynolds number on the full-scale flight vehicle surface pressure distribution at M = 0.9, A8 ~ 200 in.^{2}, α ~ 2.5 deg, and NPR ~4.

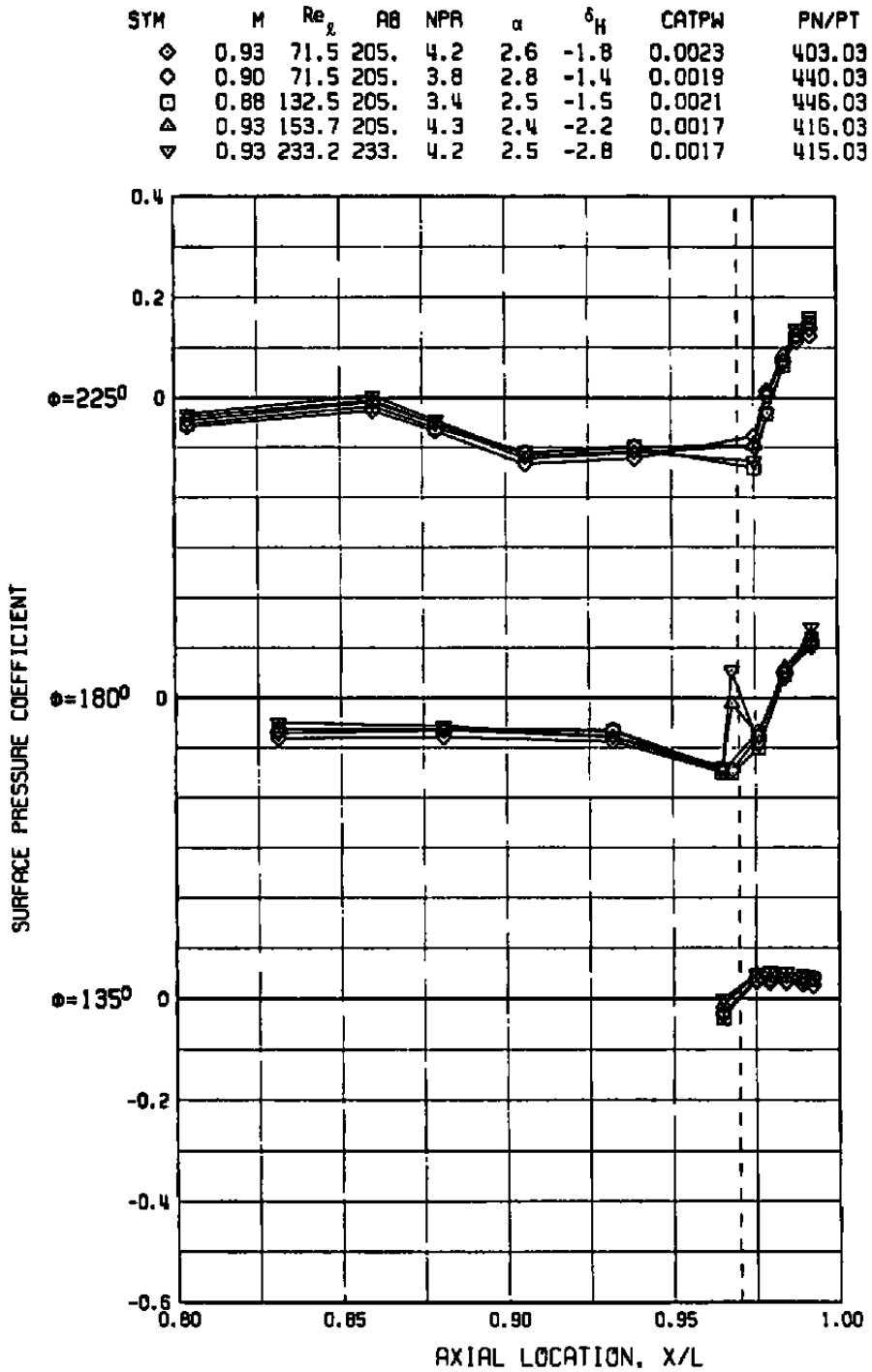

b. Windward-side pressures
Figure 25. Concluded.

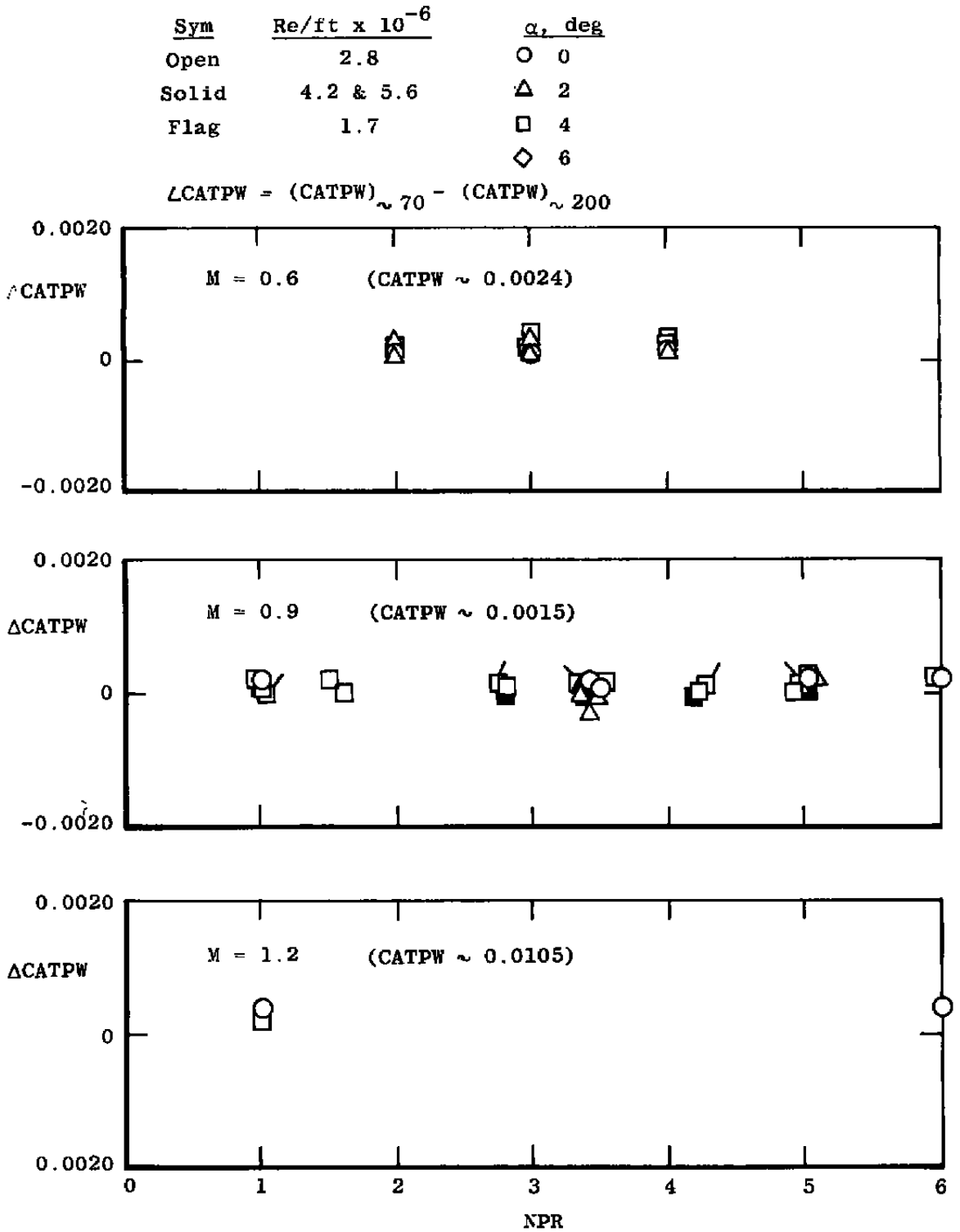

Figure 26. Effect of limited-orifice integration on the cruise nozzle (A8 = 200 in.²) loads.

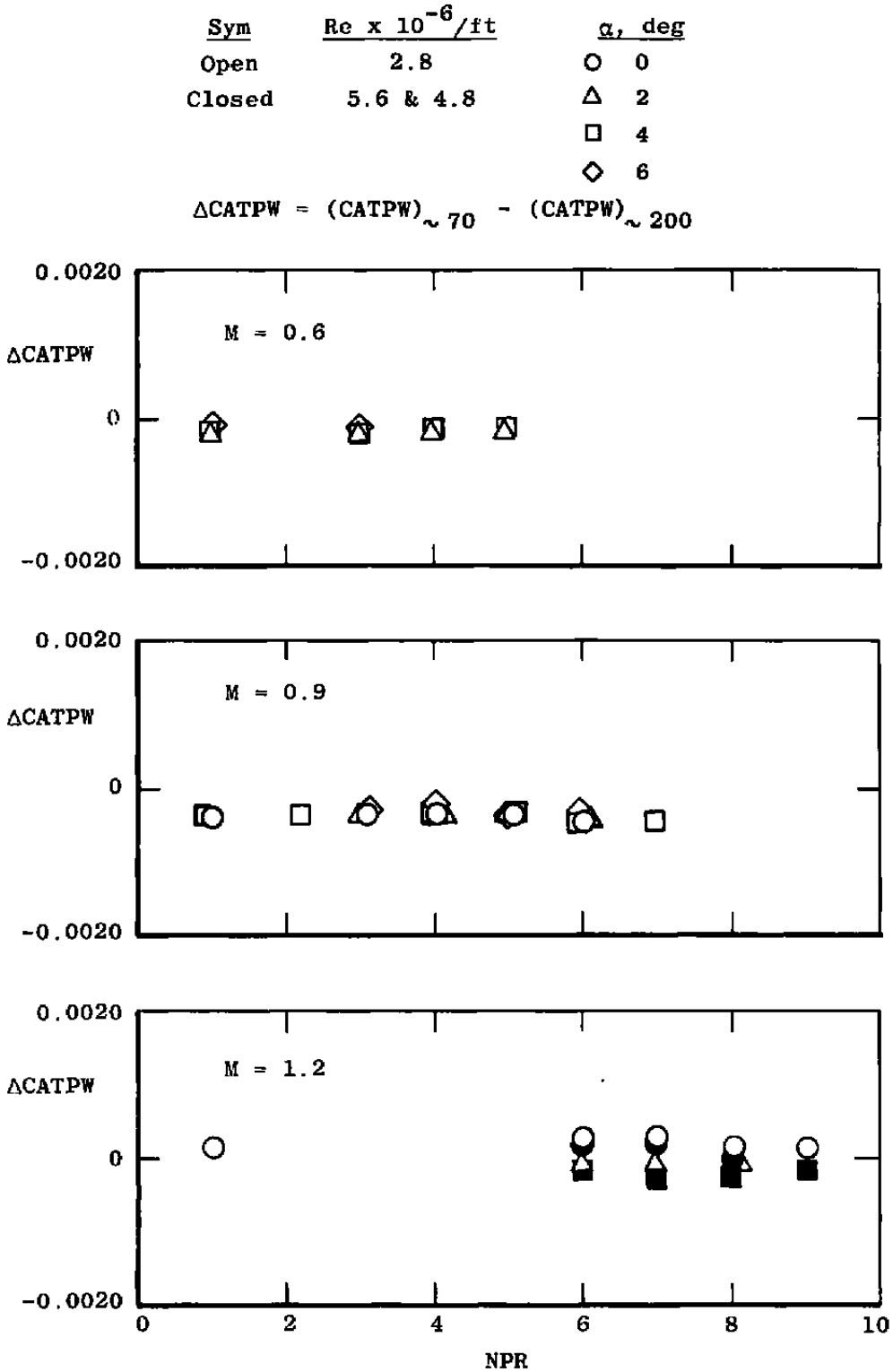

Figure 27. Effect of limited-orifice integration on the intermediate nozzle (A8 = 286 in.²) loads.

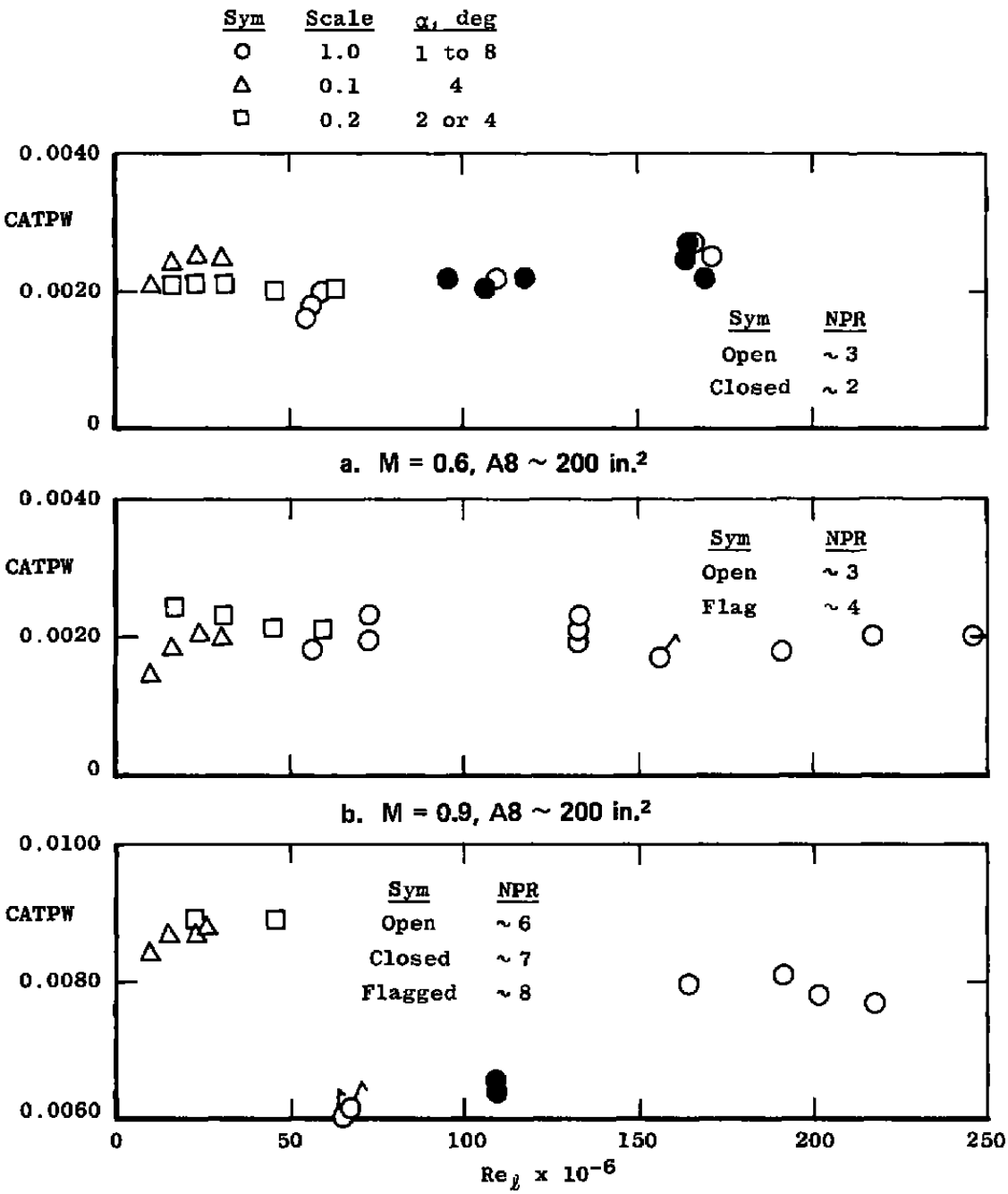

Figure 28. Comparison of the integrated axial loads from the corrected-wind-tunnel full-jet model and flight vehicle.

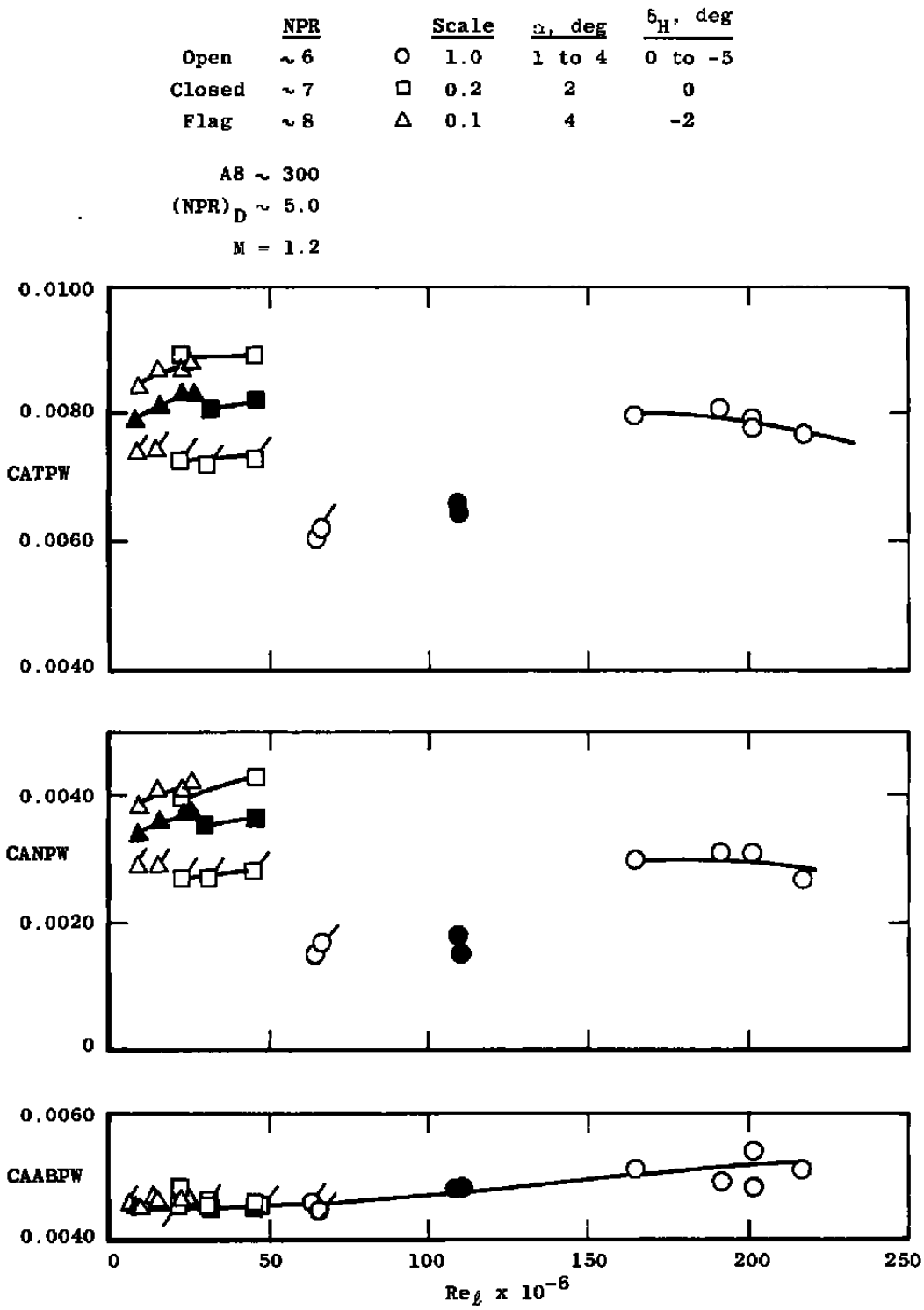

Figure 29. Comparison of components of the integrated axial loads from the corrected-wind-tunnel full-jet model and flight vehicle with NPR variations.

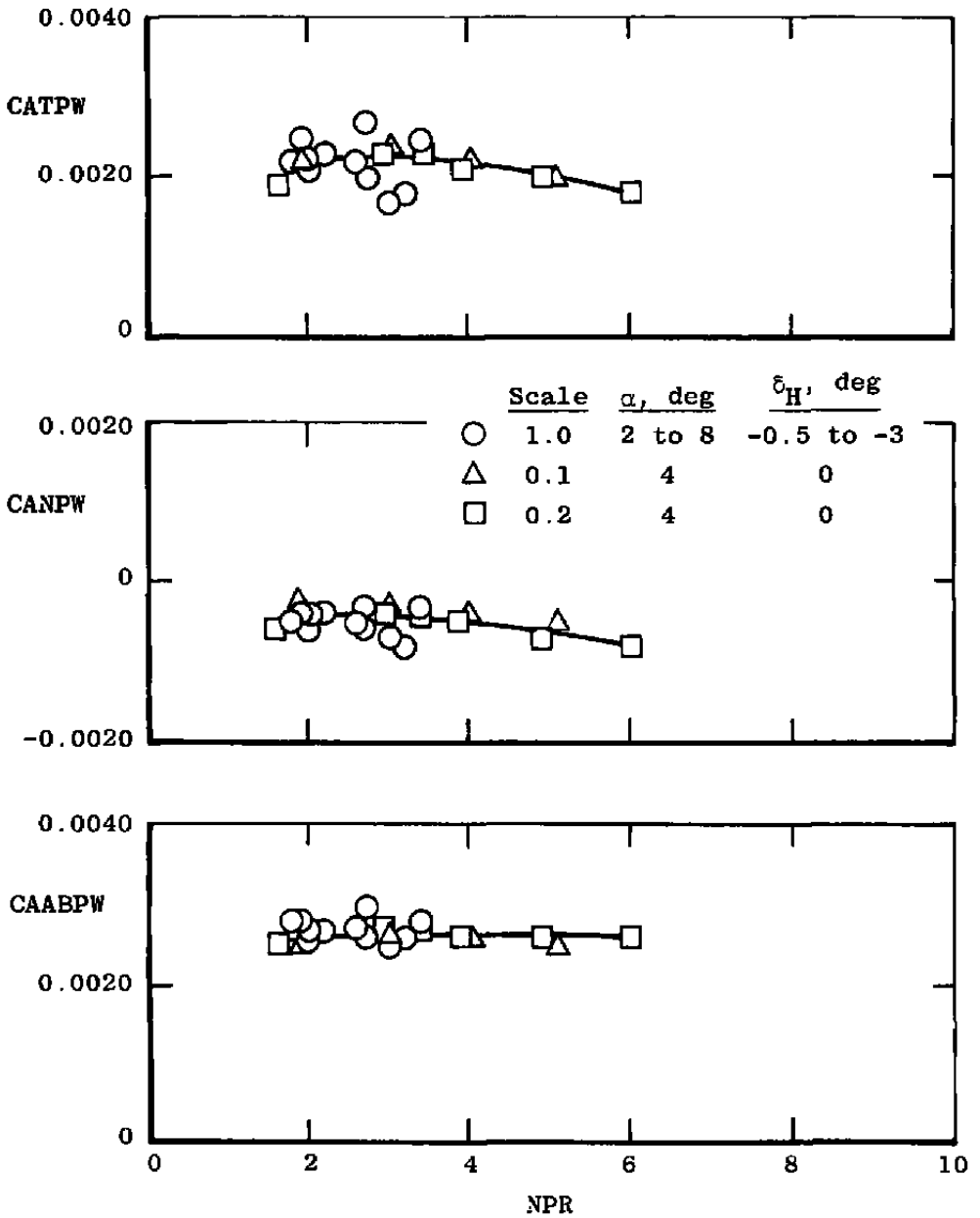

a. M = 0.6, A 8 ~ 200 in.^{2}

a. M = 0.6, A8 ~ 200 in.^{2}

Figure 30. Effect of NPR on the comparison of wind tunnel to flight integrated axial loads.

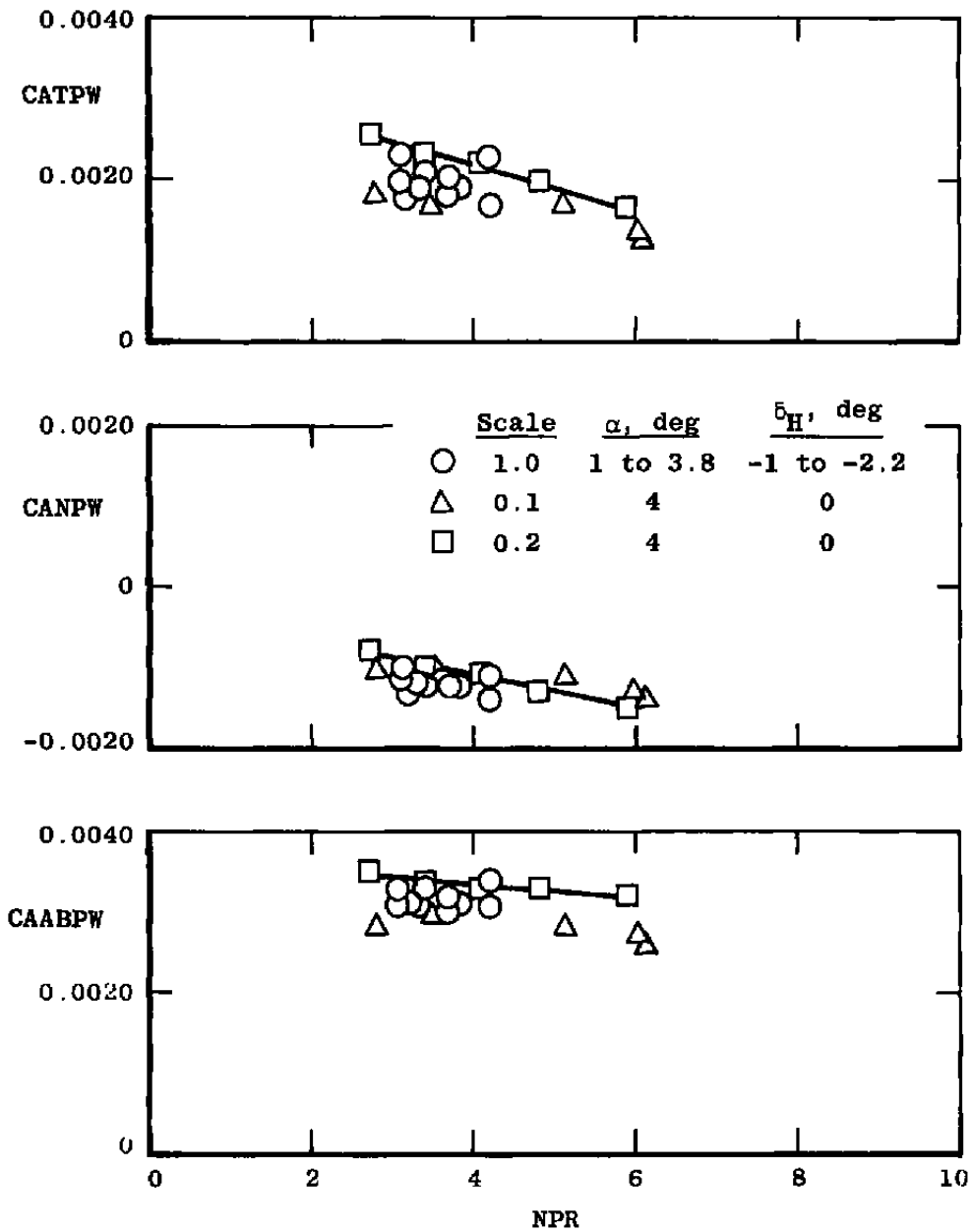

b. M = 0.9, A8 ~ 200 in.²
Figure 30. Continued.

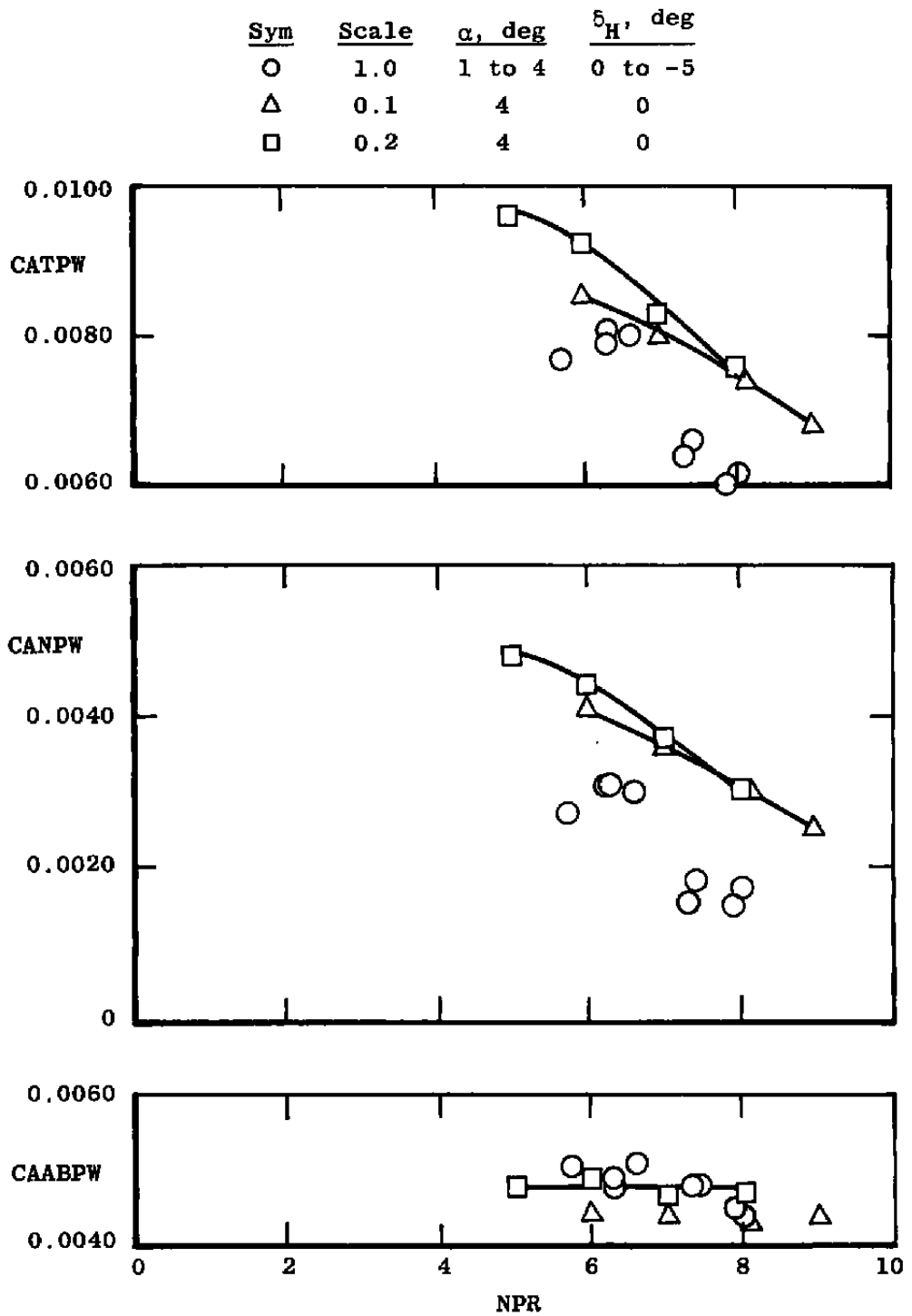

c. M = 1.2, A8 ~ 300 in.²
Figure 30. Concluded.

SYM	M	Re_{ℓ}	A8	NPR	α	δ_H	CATPW	SCALE
△	0.60	14.9	200.	3.6	6.6	-1.8	0.0023	0.1 (WT Corr.)
□	0.60	60.5	200.	3.7	6.4	-1.8	0.0019	0.2 (WT Corr.)
○	0.64	58.3	205.	3.7	6.5	-1.8	0.0021	1.0

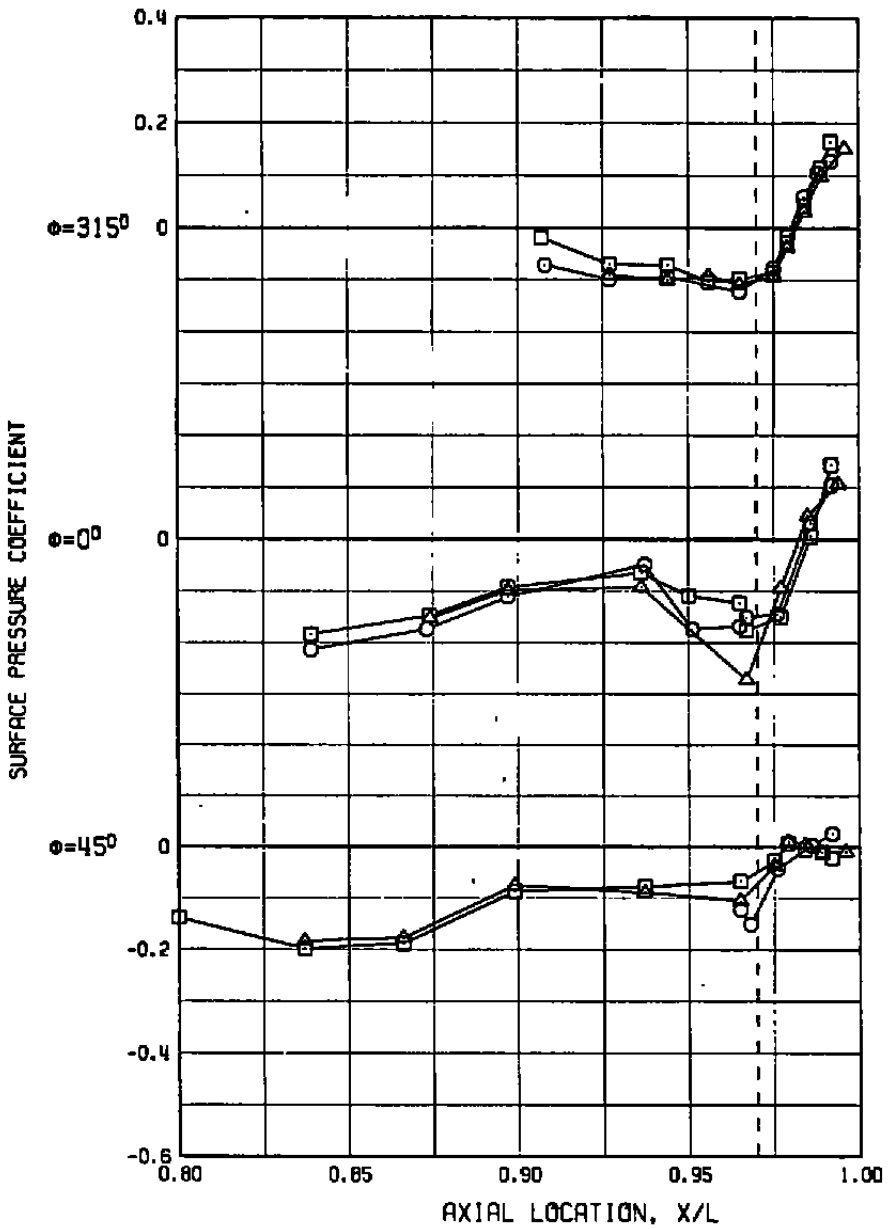

a. Lee-side pressures

Figure 31. Comparison of wind tunnel and flight vehicle surface pressure distributions at M = 0.6, A8 = 200 in.^{2}, $\alpha \sim 6.5$ deg, and NPR ~ 3.7.

SYM	M	Re_λ	AB	NPR	α	δ_H	CATPW	SCALE
△	0.60	14.9	200.	3.6	6.6	-1.8	0.0023	0.1 (WT Corr.)
⊡	0.60	60.5	200.	3.7	6.4	-1.8	0.0019	0.2 (WT Corr.)
⊙	0.64	58.3	205.	3.7	6.5	-1.8	0.0021	1.0

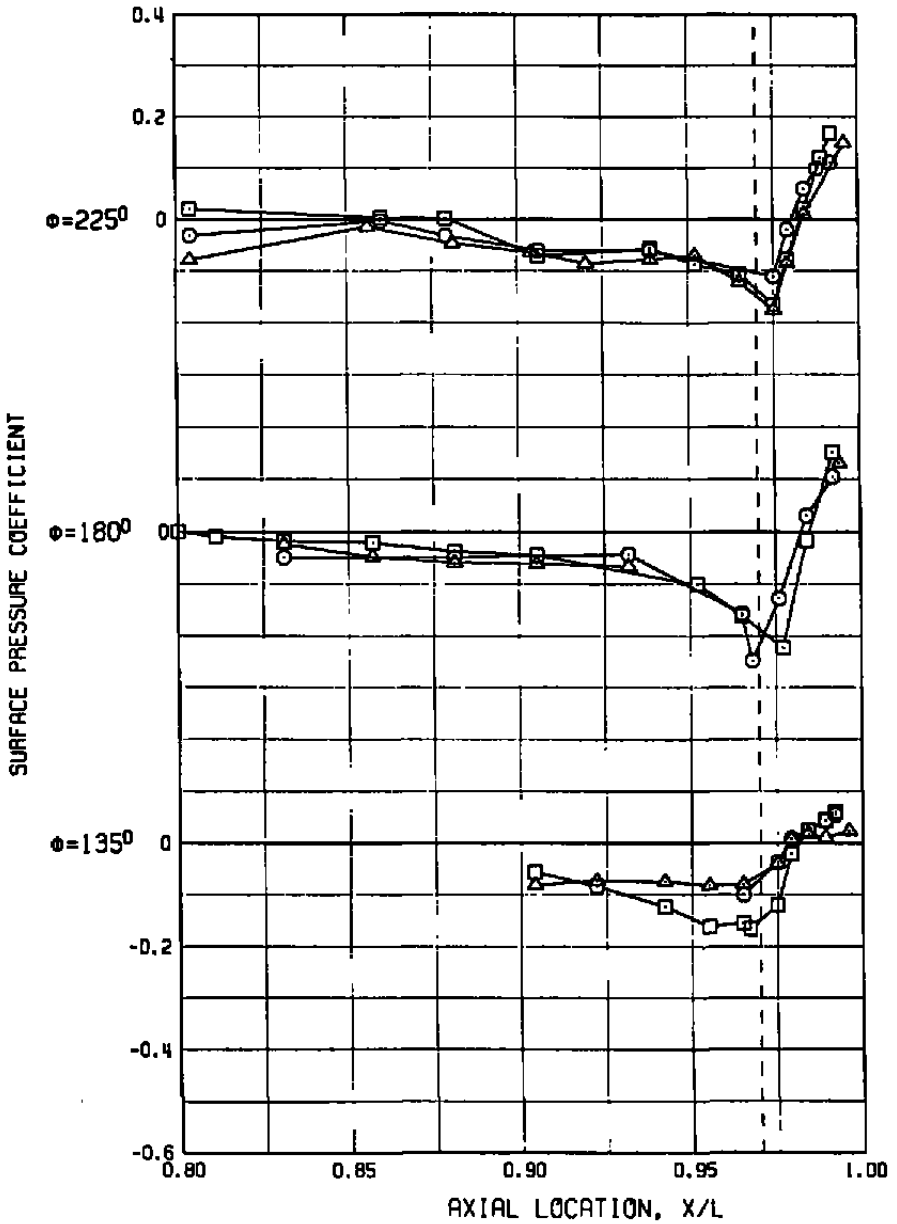

b. Windward-side pressures

Figure 31. Concluded.

SYM	M	Re_{ℓ}	A8	NPR	α	δ_H	CATPW	SCALE
△	0.60	14.9	200.	2.9	8.3	-1.6	0.0024	0.1 (WT Corr.)
□	0.60	60.6	200.	2.9	8.3	-1.6	0.0018	0.2 (WT Corr.)
○	0.60	55.6	205.	2.9	9.0	-1.6	0.0017	1.0

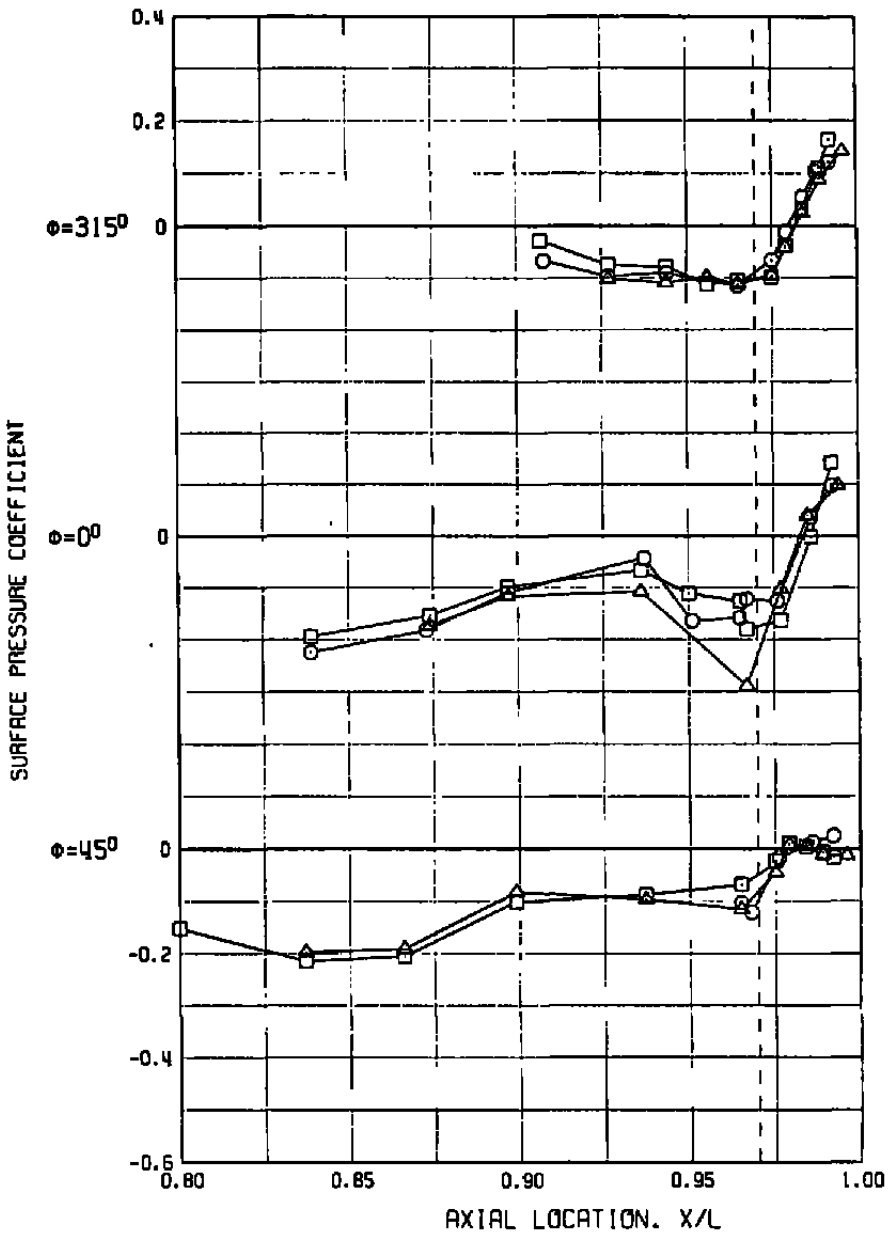

a. Lee-side pressures

Figure 32. Comparison of wind tunnel and flight vehicle surface pressure distributions at M = 0.6, A8 = 200 in.², α ~ 8.5 deg, and NPR ~ 2.9.

SYM	M	Re_ℓ	AB	NPR	α	δ_H	CATPW	SCALE
△	0.60	14.9	200.	2.9	8.3	-1.6	0.0024	0.1 (WT Corr.)
□	0.60	60.6	200.	2.9	8.3	-1.6	0.0018	0.2 (WT Corr.)
○	0.60	55.6	205.	2.9	9.0	-1.6	0.0017	1.0

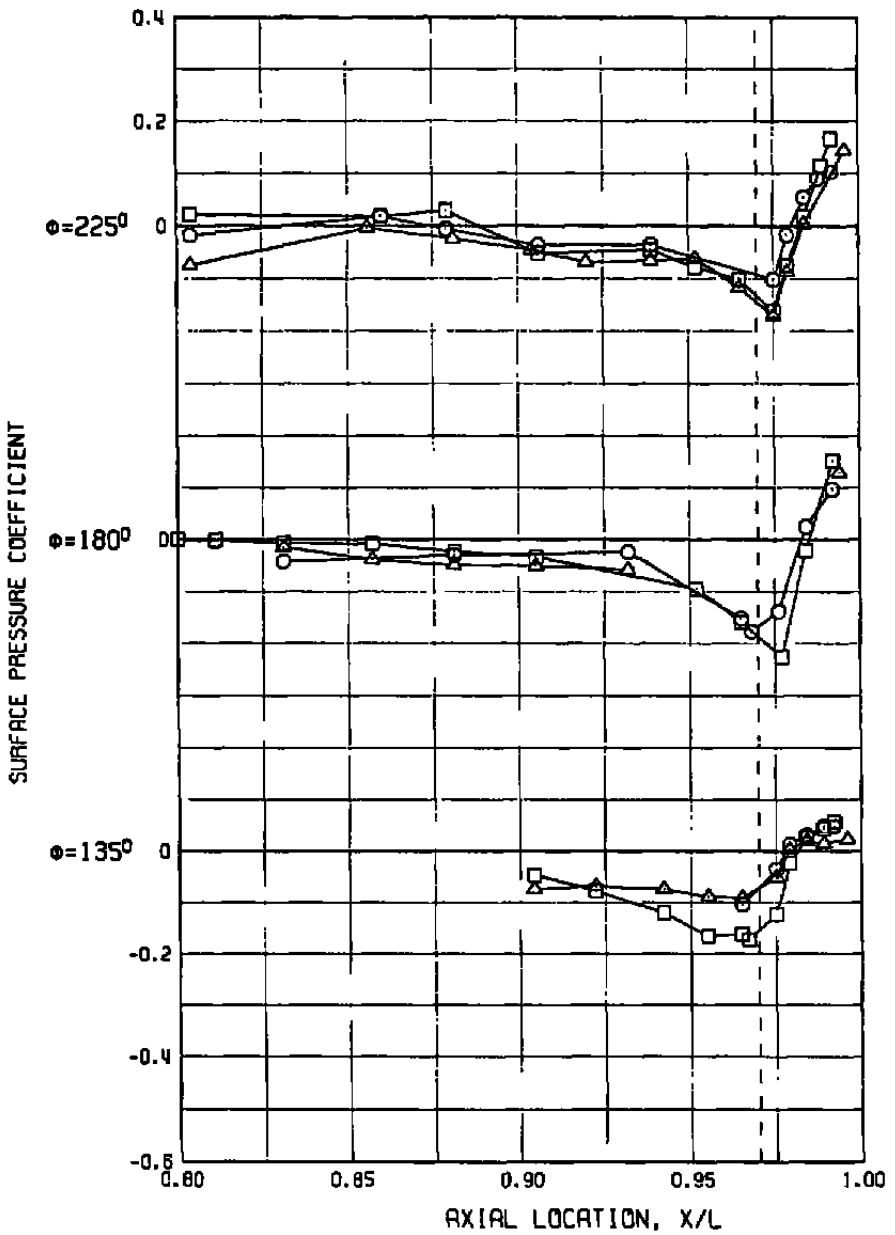

b. Windward-side pressures

Figure 32. Concluded.

SYM	M	Re_ℓ	A8	NPR	α	δ_H	CATPW	SCALE
△	0.90	14.8	200.	3.8	2.8	-1.4	0.0016	0.1 (WT Corr.)
⊡	0.90	59.3	200.	3.4	2.5	-1.5	0.0015	0.2 (WT Corr.)
○	0.90	71.5	205.	3.8	2.8	-1.4	0.0019	1.0

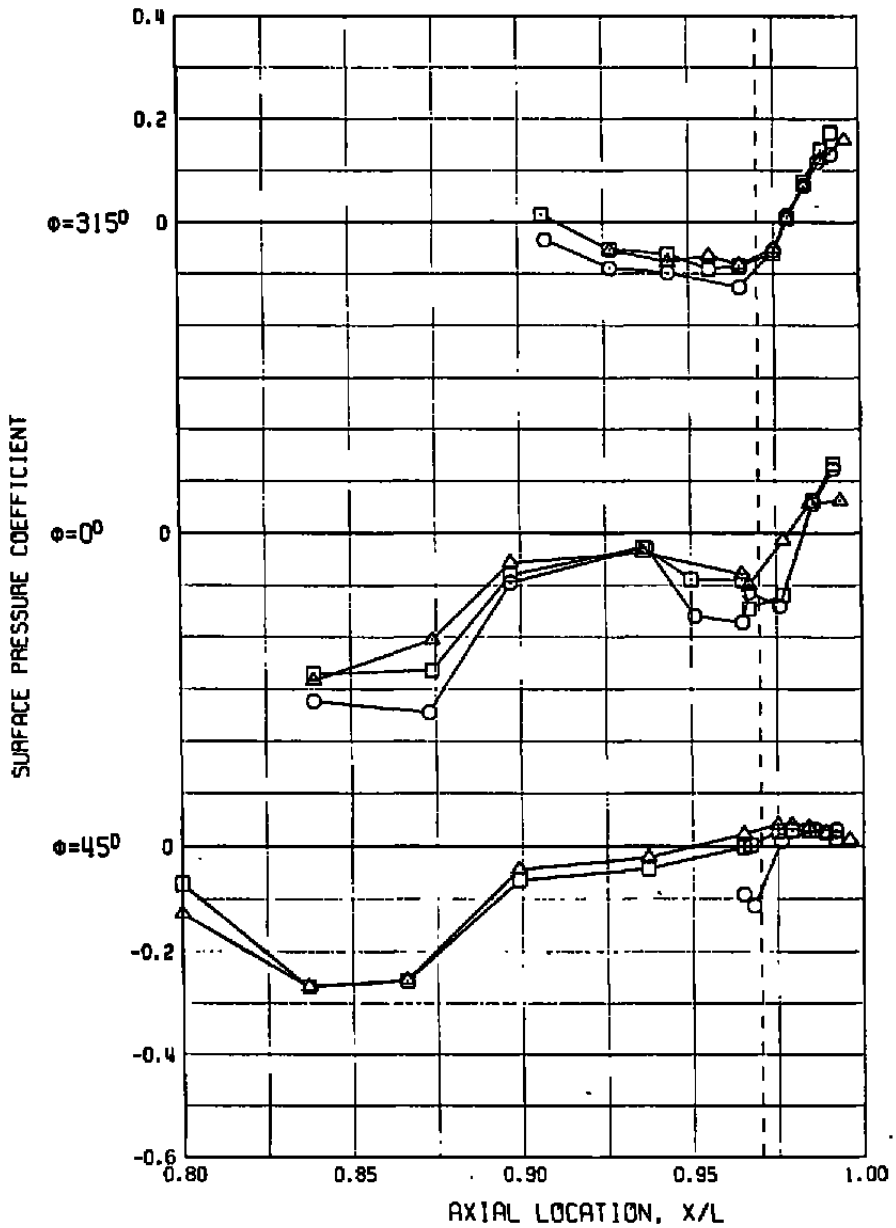

a. Lee-side pressures

Figure 33. Comparison of wind tunnel and flight vehicle surface pressure distributions at M = 0.9, A8 = 200 in.^{2} $\alpha \sim 2.8$ deg, and NPR ~ 3.6.

SYM	M	Re_ℓ	AB	NPR	α	δ_H	CATPW	SCALE
△	0.90	14.8	200.	3.8	2.8	-1.4	0.0016	0.1 (WT Corr.)
□	0.90	59.3	200.	3.4	2.5	-1.5	0.0016	0.2 (WT Corr.)
⊙	0.90	71.5	205.	3.8	2.8	-1.4	0.0019	1.0

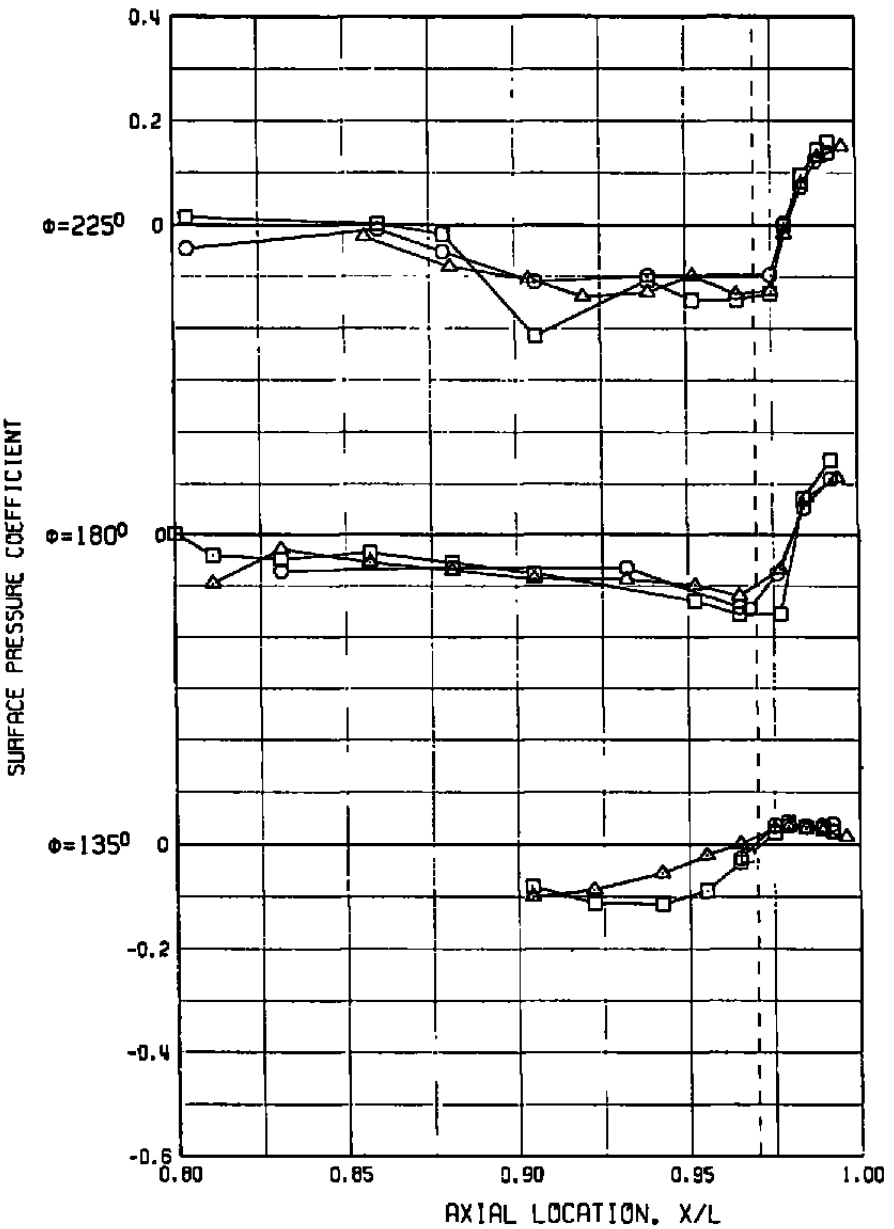

b. Windward-side pressures

Figure 33. Concluded.

SYM	M	Re_ℓ	A8	NPR	α	δ_H	CATPW	SCALE
△	0.90	14.8	200.	3.7	3.8	-1.6	0.0016	0.1 (WT Corr.)
⊡	0.90	59.4	200.	3.4	3.9	-1.5	0.0015	0.2 (WT Corr.)
○	0.89	55.6	204.	3.7	3.8	-1.6	0.0018	1.0

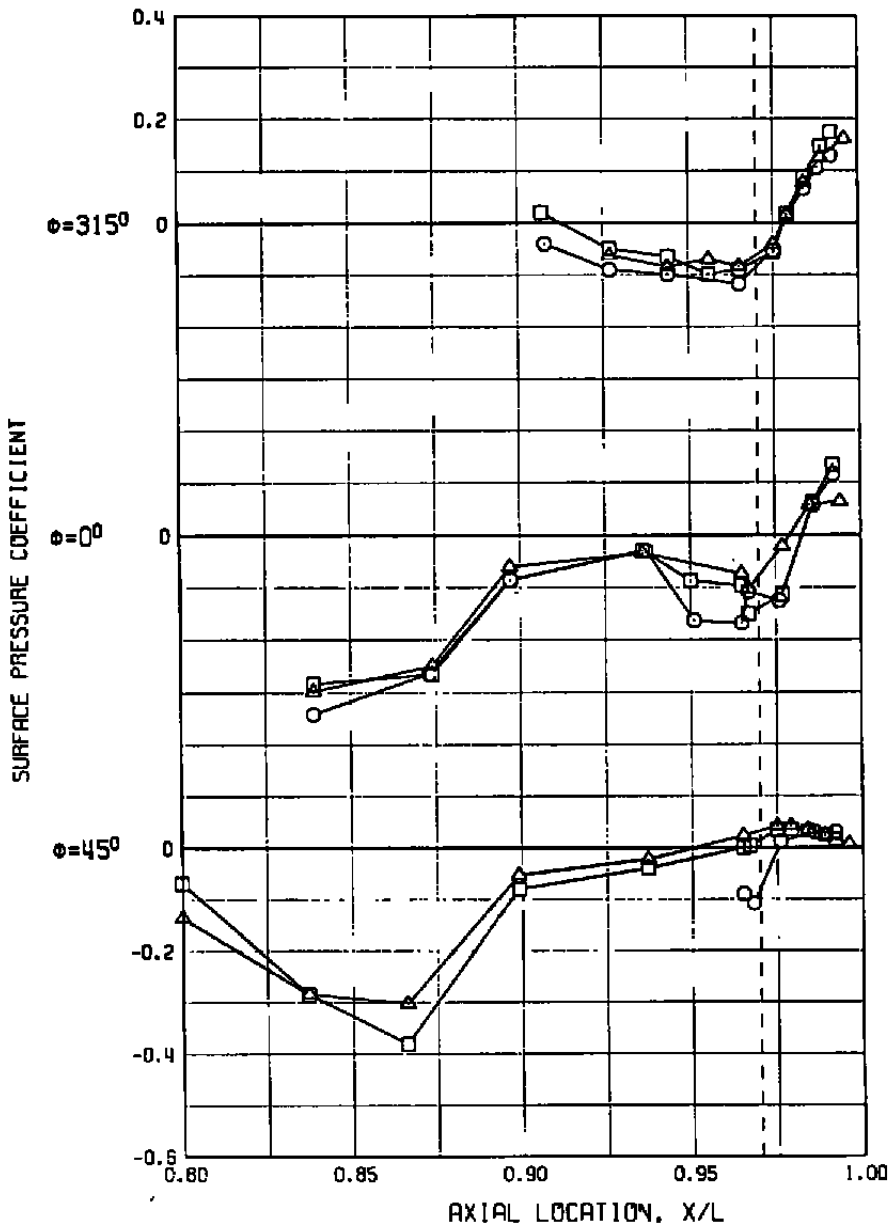

a. Lee-side pressures

Figure 34. Comparison of wind tunnel and flight vehicle surface pressure distributions at M = 0.9, A8 = 200 in.^{2}, $\alpha \sim 3.9$ deg, and NPR ~ 3.5.

SYM	M	Re_ℓ	AB	NPR	α	δ_H	CATPW	SCALE
△	0.90	14.8	200.	3.7	3.8	-1.6	0.0016	0.1 (WT Corr.)
□	0.90	59.4	200.	3.4	3.9	-1.5	0.0015	0.2 (WT Corr.)
○	0.89	55.6	204.	3.7	3.8	-1.6	0.0018	1.0

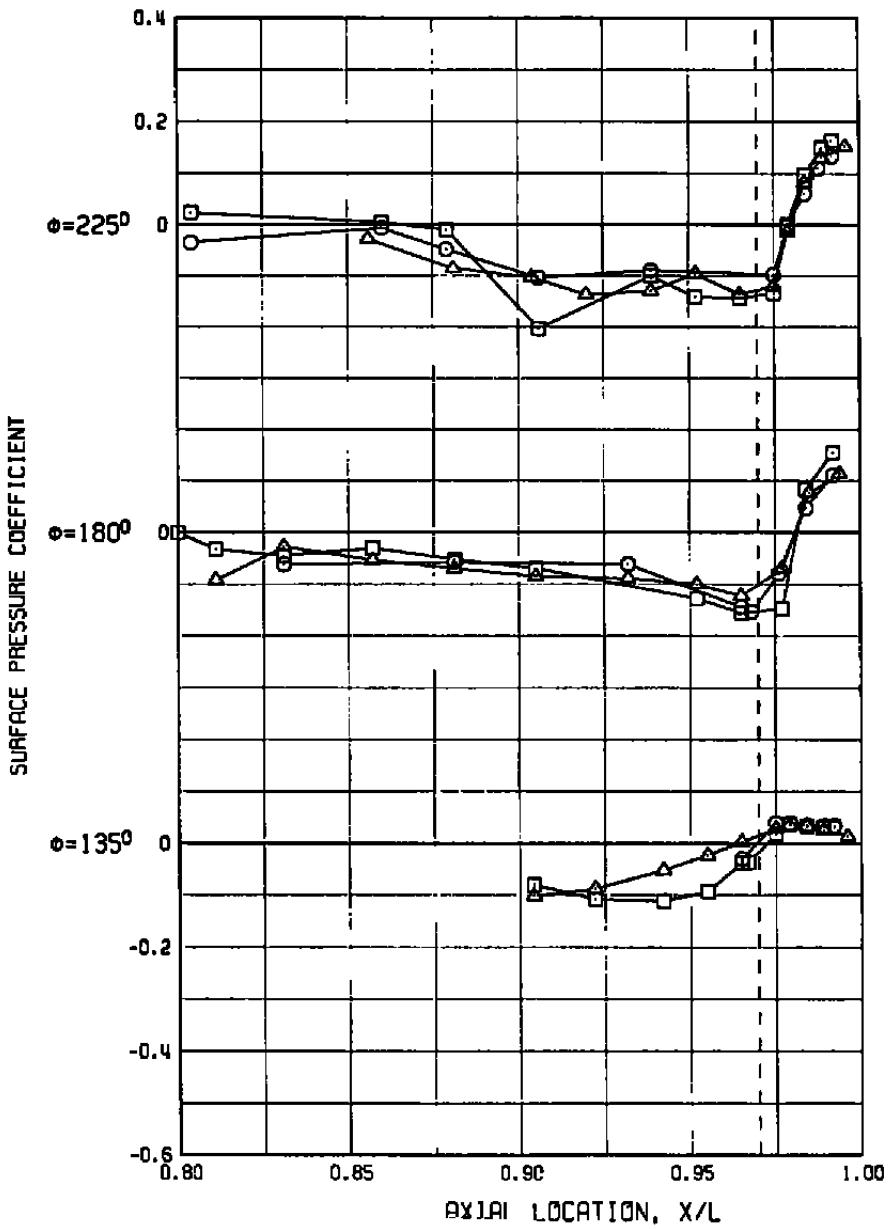

b. Windward-side pressures

Figure 34. Concluded.

SYM	M	Re_{ℓ}	A8	NPR	α	δ_H	CATPW	SCALE
△	0.90	14.8	200.	5.7	3.4	-2.2	0.0014	0.1 (WT Corr.)
□	0.90	57.3	230.	5.7	3.4	-2.0	0.0019	0.2 (WT Corr.)
○	0.90	55.6	225.	5.8	3.4	-2.2	0.0011	1.0

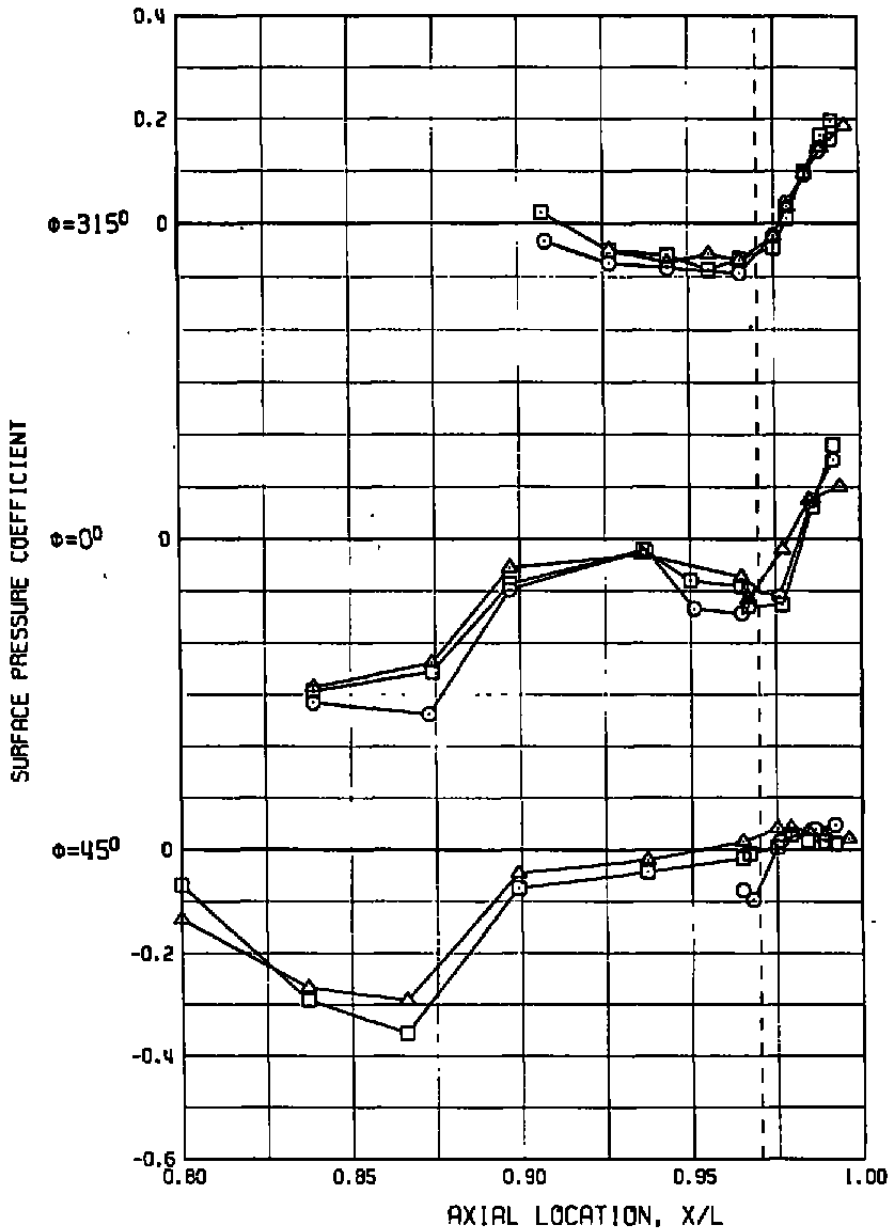

a. Lee-side pressures

Figure 35. Comparison of wind tunnel and flight vehicle surface pressure distributions at M = 0.9, A8 ~ 230 in.², α ~ 3.4 deg, and NPR ~ 5.7.

SYM	M	Re_{ℓ}	AB	NPR	α	δ_H	CATPW	SCALE
△	0.90	14.8	200.	5.7	3.4	-2.2	0.0014	0.1 (WT Corr.)
□	0.90	57.3	230.	5.7	3.4	-2.0	0.0019	0.2 (WT Corr.)
○	0.90	55.6	225.	5.8	3.4	-2.2	0.0011	1.0

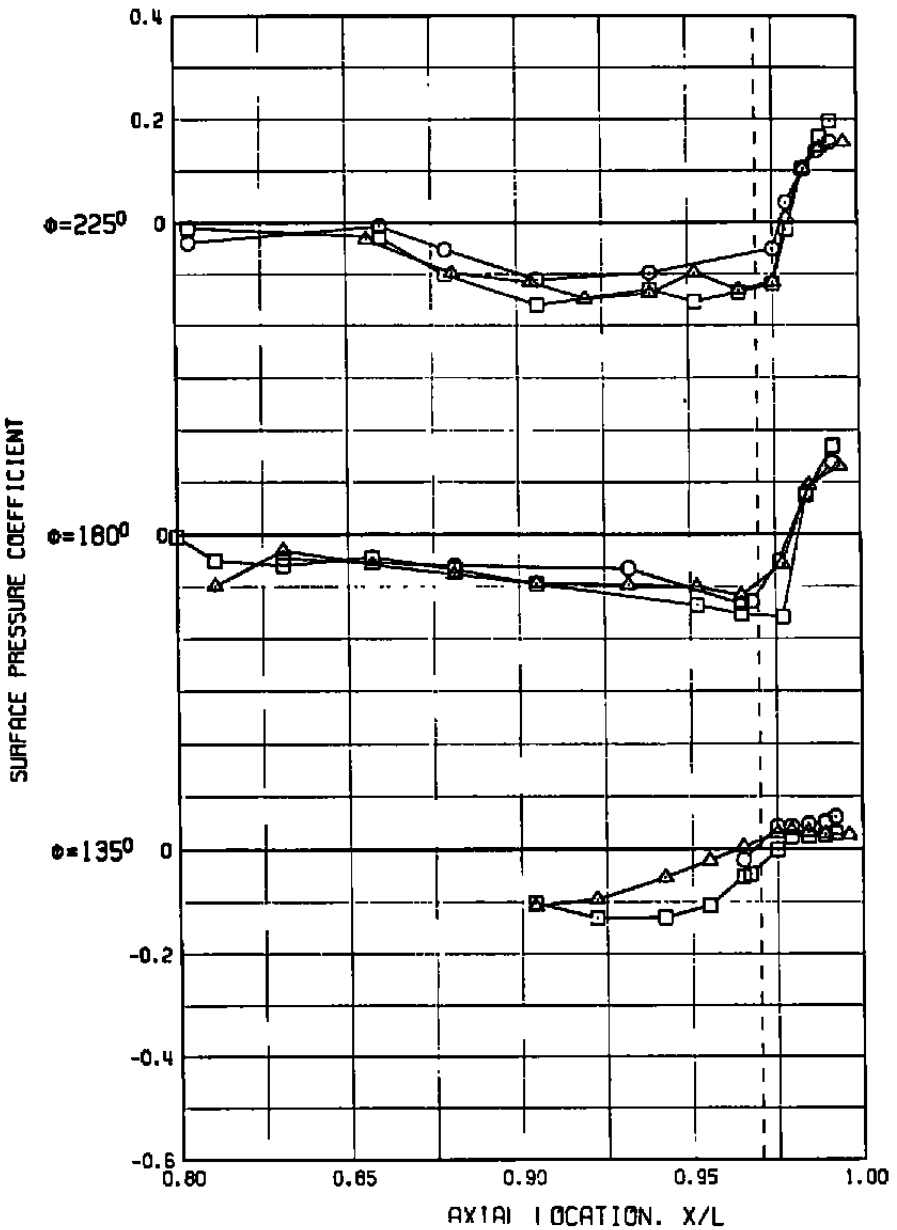

b. Windward-side pressures

Figure 35. Concluded.

SYM	M	Re_ℓ	A8	NPR	α	δ_H	CATPW	SCALE
△	0.90	14.8	200.	5.7	4.6	-2.3	0.0013	0.1 (WT Corr.)
□	0.90	57.2	230.	5.7	4.6	-2.0	0.0016	0.2 (WT Corr.)
○	0.92	55.6	229.	5.7	4.6	-2.3	0.0011	1.0

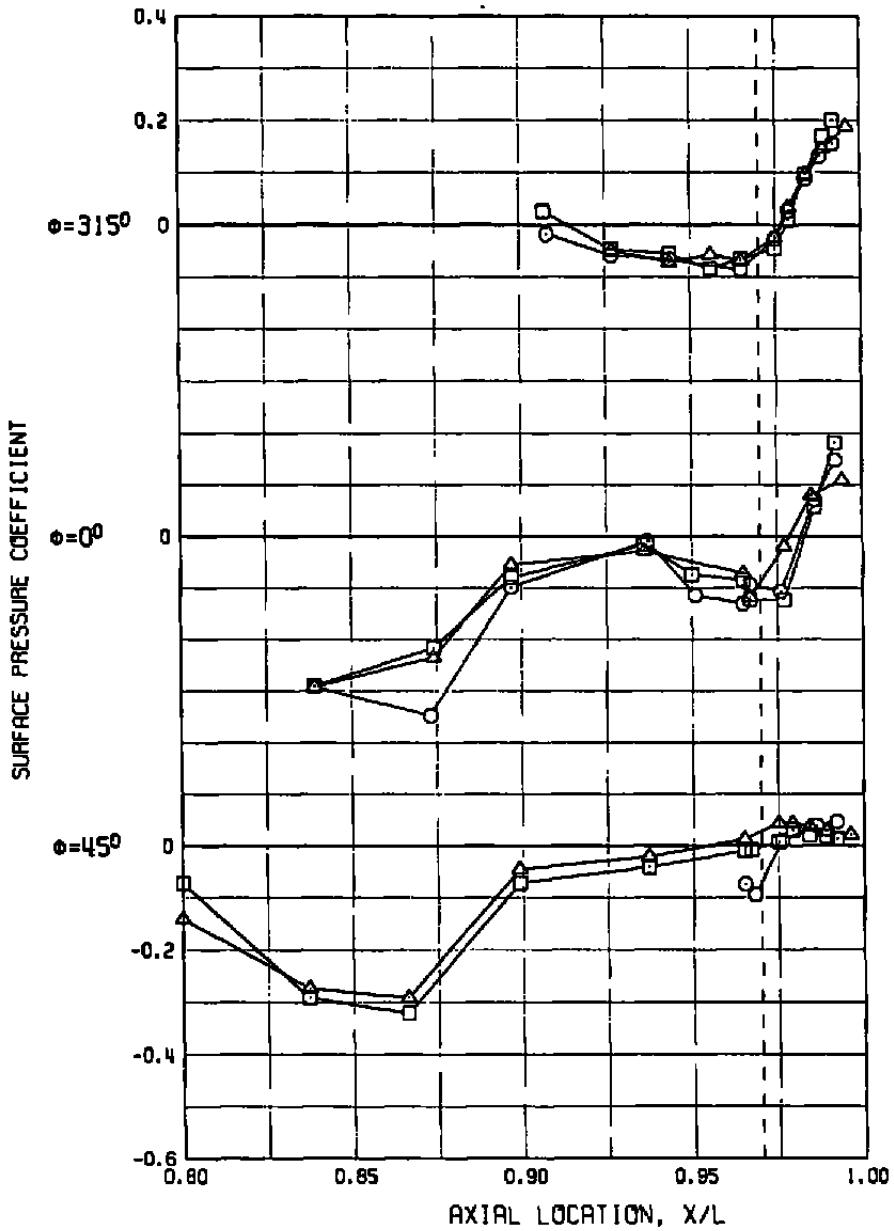

a. Lee-side pressures

Figure 36. Comparison of wind tunnel and flight vehicle surface pressure distributions at M = 0.9, A8 ~ 230 in.², α ~ 4.6 deg, and NPR ~ 5.7.

SYM	M	Re_{ℓ}	AB	NPR	α	δ_H	CATPW	SCALE
△	0.90	14.8	200.	5.7	4.6	-2.3	0.0013	0.1 (WT Corr.)
□	0.90	57.2	230.	5.7	4.6	-2.0	0.0016	0.2 (WT Corr.)
○	0.92	55.6	229.	5.7	4.6	-2.3	0.0011	1.0

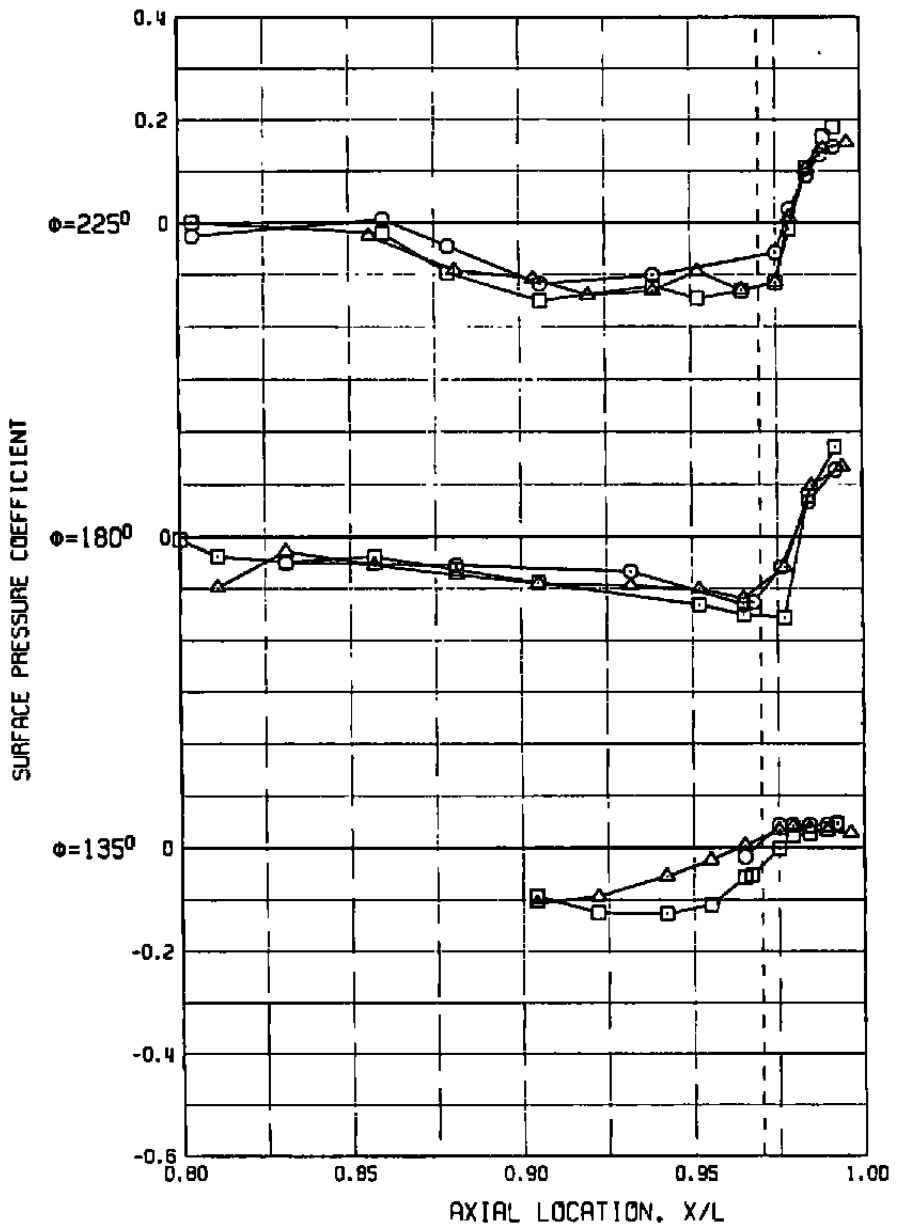

b. Windward-side pressures

Figure 36. Concluded.

SYM	M	Re_ℓ	A8	NPR	α	δ_H	CATPW	SCALE
△	0.90	14.8	200.	5.6	5.9	-2.2	0.0011	0.1 (WT Corr.)
□	0.90	57.3	230.	5.6	5.9	-2.0	0.0012	0.2 (WT Corr.)
○	0.89	55.6	235.	5.6	5.9	-2.2	0.0012	1.0

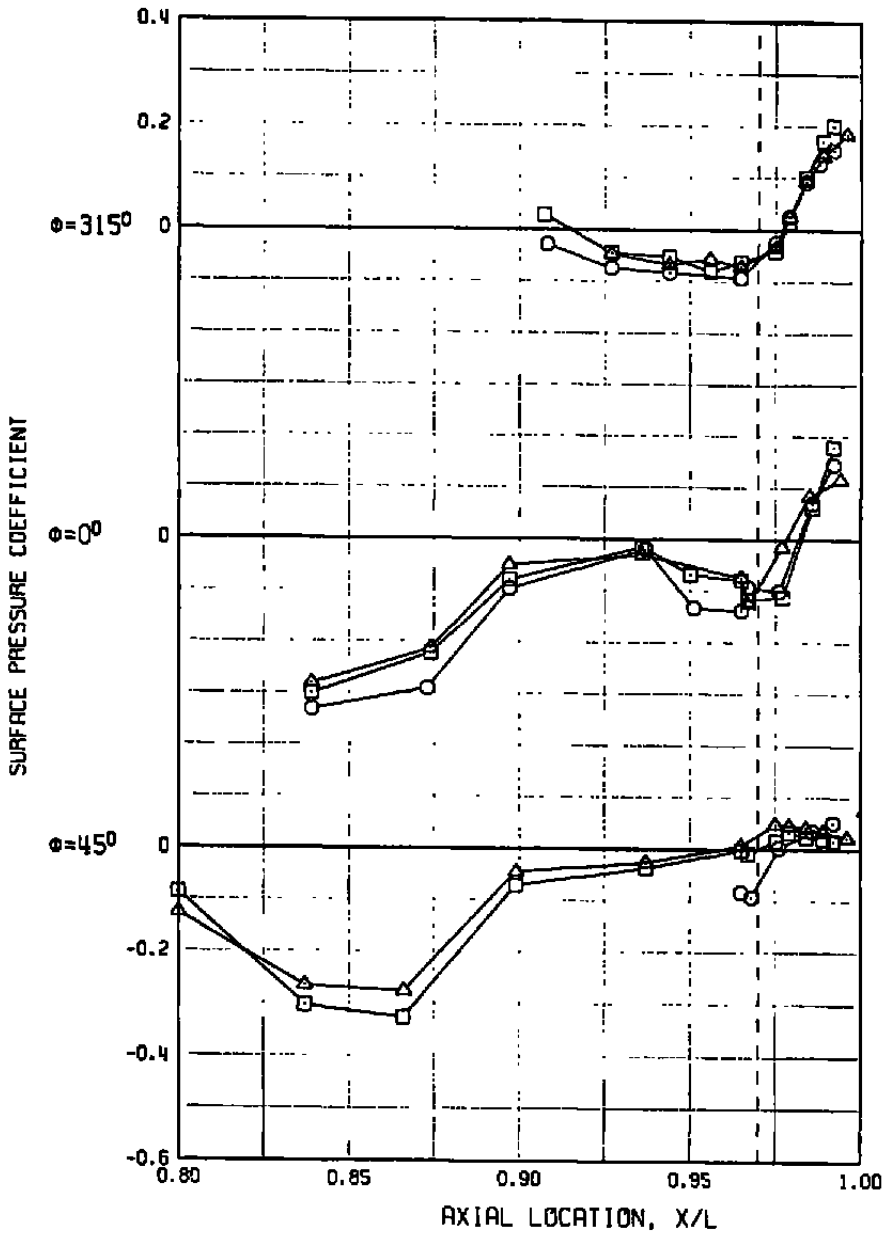

a. Lee-side pressures

Figure 37. Comparison of wind tunnel and flight vehicle surface pressure distributions at M = 0.9, A8 ~ 230 in.², α ~ 5.9 deg, and NPR = 5.6.

SYM	M	Re_ℓ	AB	NPR	α	δ_H	CRTPW	SCALE
△	0.90	14.8	200.	5.6	5.9	-2.2	0.0011	0.1 (WT Corr.)
□	0.90	57.3	230.	5.6	5.9	-2.0	0.0012	0.2 (WT Corr.)
○	0.89	55.6	235.	5.6	5.9	-2.2	0.0012	1.0

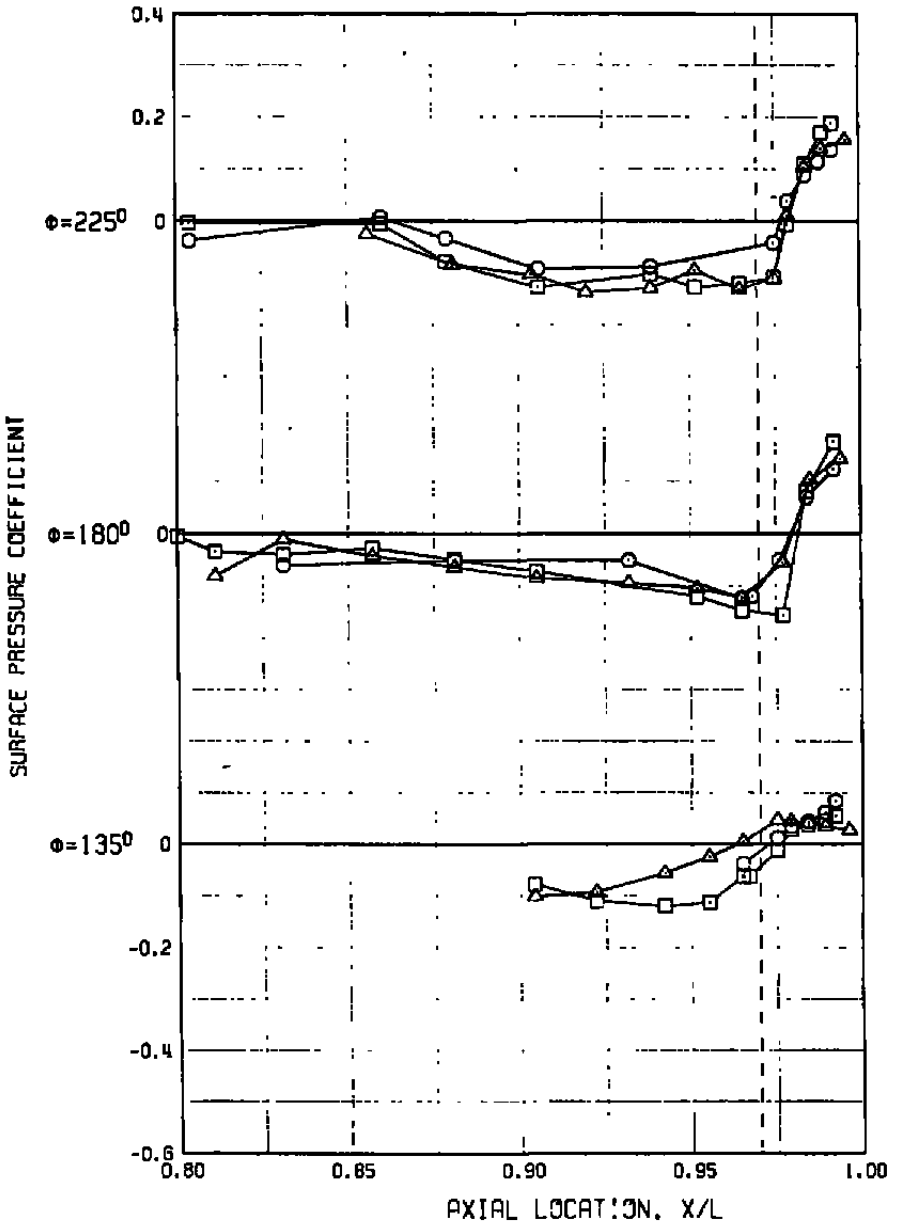

b. Windward-side pressures
Figure 37. Concluded.

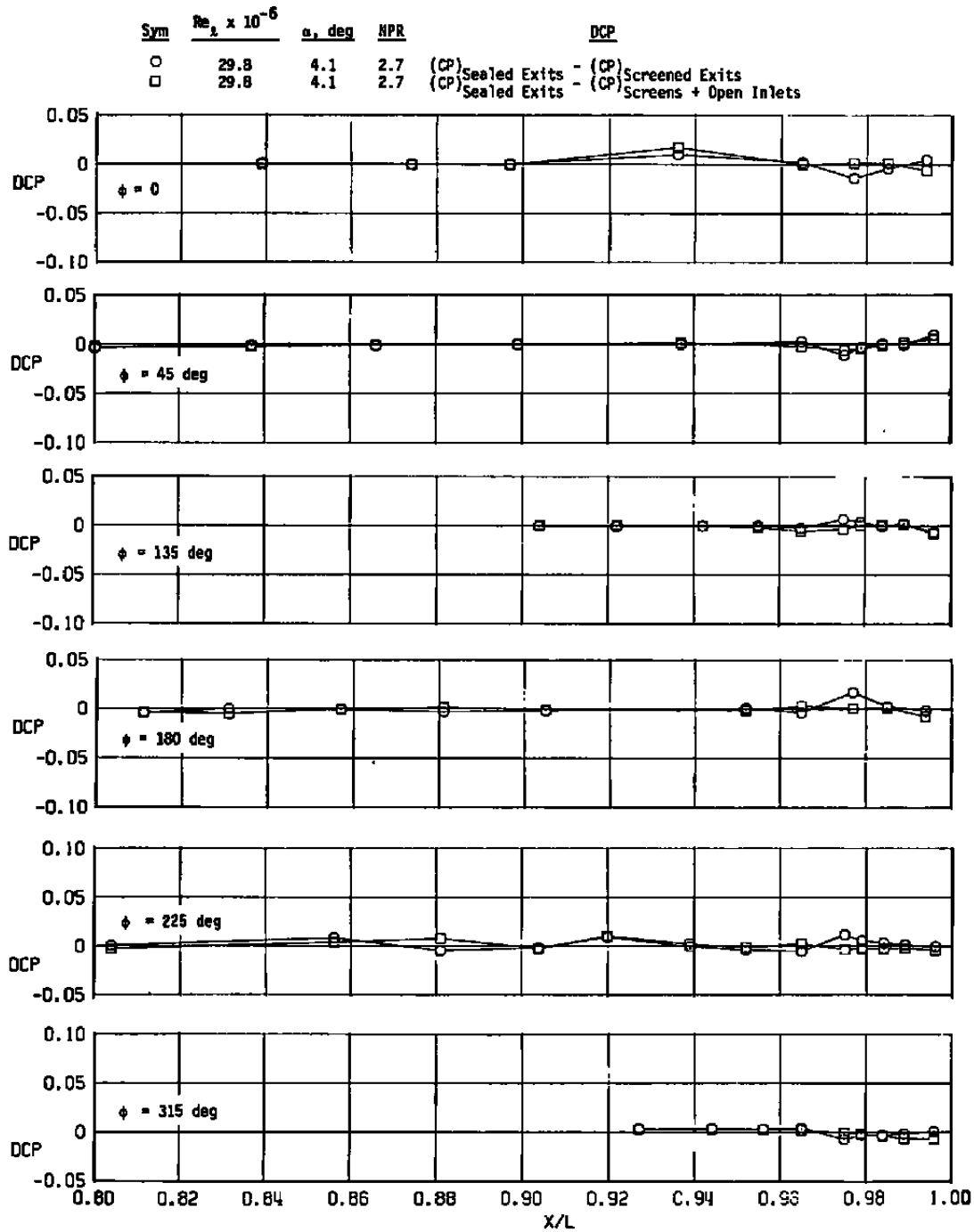

Figure 38. Effect of incremental bay purge flow changes on the 0.2-scale model surface pressure coefficients at M = 0.6, A8 = 200 in.^{2}, α_H = -1.5 deg.

SYM	M	Re_ℓ	A8	NPR	α	δ_H	CATPW	SCALE
△	0.60	14.9	200.	2.7	6.2	-1.4	0.0022	0.1 (WT Corr.)
□	0.60	29.7	200.	2.7	5.9	-1.5	0.0023	0.2 (WT. Corr.)
○	0.60	58.3	204.	2.7	5.8	-1.4	0.0020	1.0

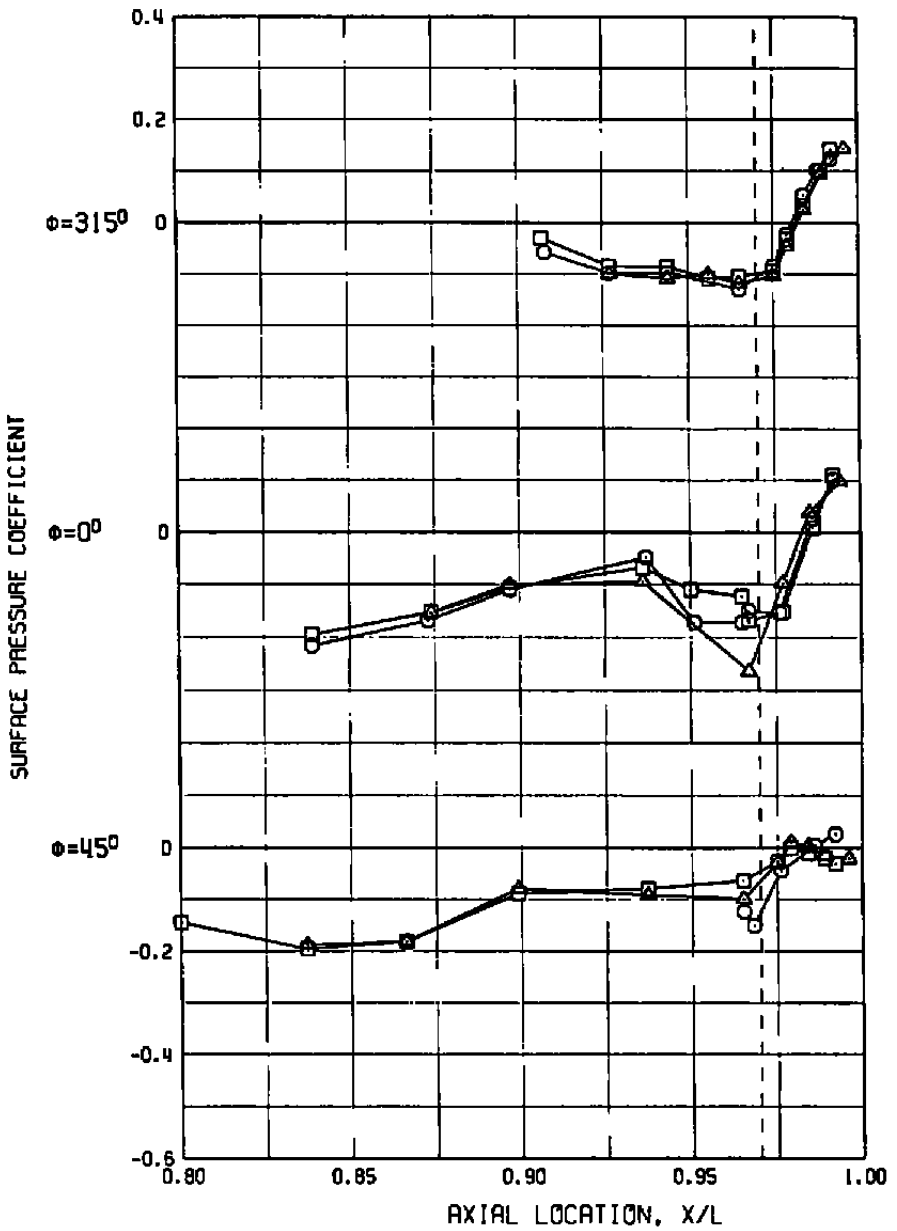

a. Lee-side pressures

Figure 39. Comparison of the wind tunnel and flight vehicle surface pressure distributions at M = 0.6, A8 = 200 in.^{2}, α = 6 deg, and NPR = 2.7.

SYM	M	Re_{ℓ}	AB	NPR	α	δ_H	CATPW	SCALE
△	0.60	14.9	200.	2.7	6.2	-1.4	0.0022	0.1 (WT Corr.)
□	0.60	29.7	200.	2.7	5.9	-1.5	0.0023	0.2 (WT Corr.)
○	0.60	58.3	204.	2.7	5.8	-1.4	0.0020	1.0

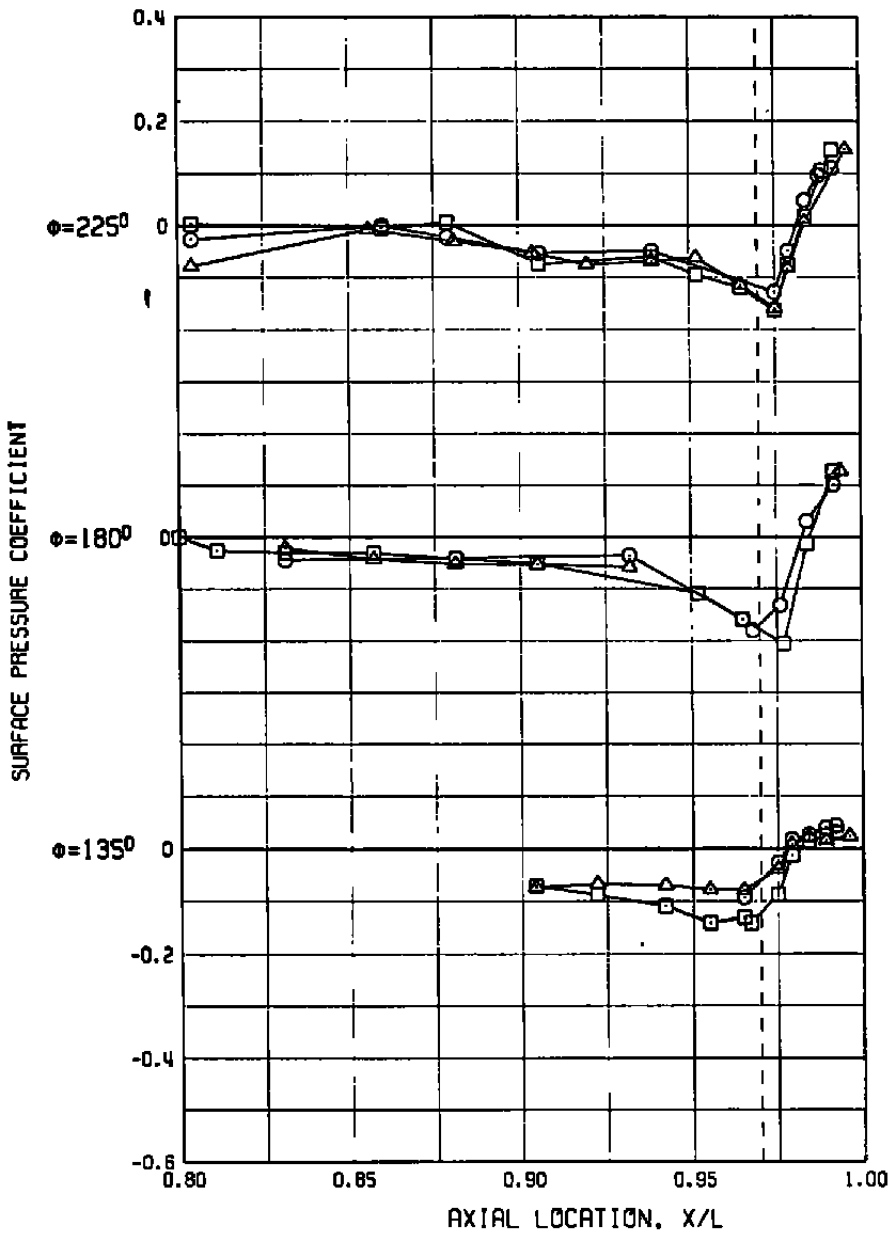

b. Windward-side pressures

Figure 39. Concluded.

SYM	M	Re_{ℓ}	A8	NPR	α	δ_H	CATPW	SCALE
△	1.20	14.9	286.	8.0	2.8	-3.3	0.0078	0.1 (WT Corr.)
□	1.20	29.7	300.	8.1	2.7	-3.3	0.0083	0.2 (WT Corr.)
⊙	1.24	63.6	302.	7.9	3.1	-3.3	0.0060	1.0

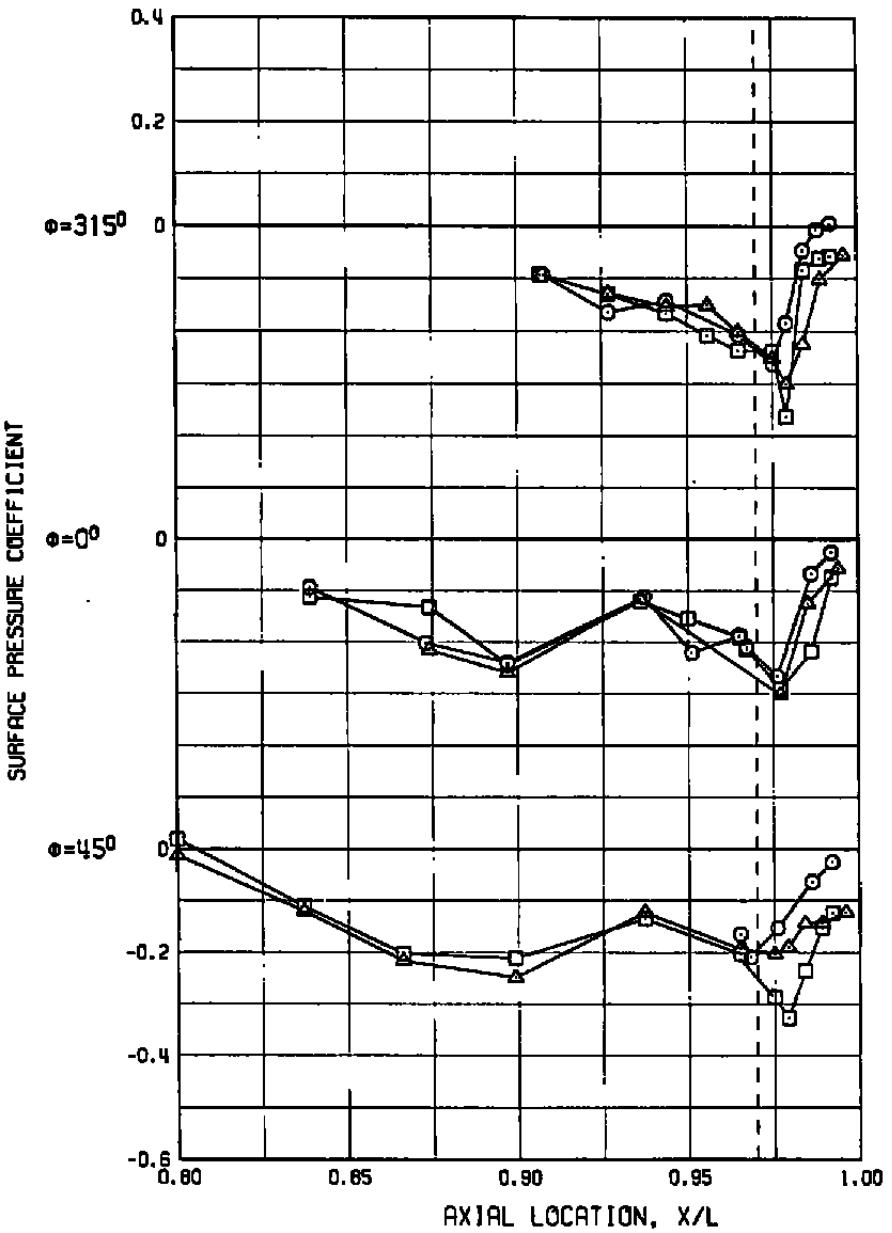

a. Lee-side pressures

Figure 40. Comparison of wind tunnel and flight vehicle surface pressure distributions at M = 1.2, A8 ~ 300 in.², α ~ 2.7 deg, and NPR ~ 8.0.

SYM	M	Re_{ℓ}	AB	NPR	α	δ_H	CATPW	SCALE
△	1.20	14.9	286.	8.0	2.8	-3.3	0.0078	0.1 (WT Corr.)
□	1.20	29.7	300.	8.1	2.7	-3.3	0.0083	0.2 (WT Corr.)
○	1.24	63.6	302.	7.9	3.1	-3.3	0.0060	1.0

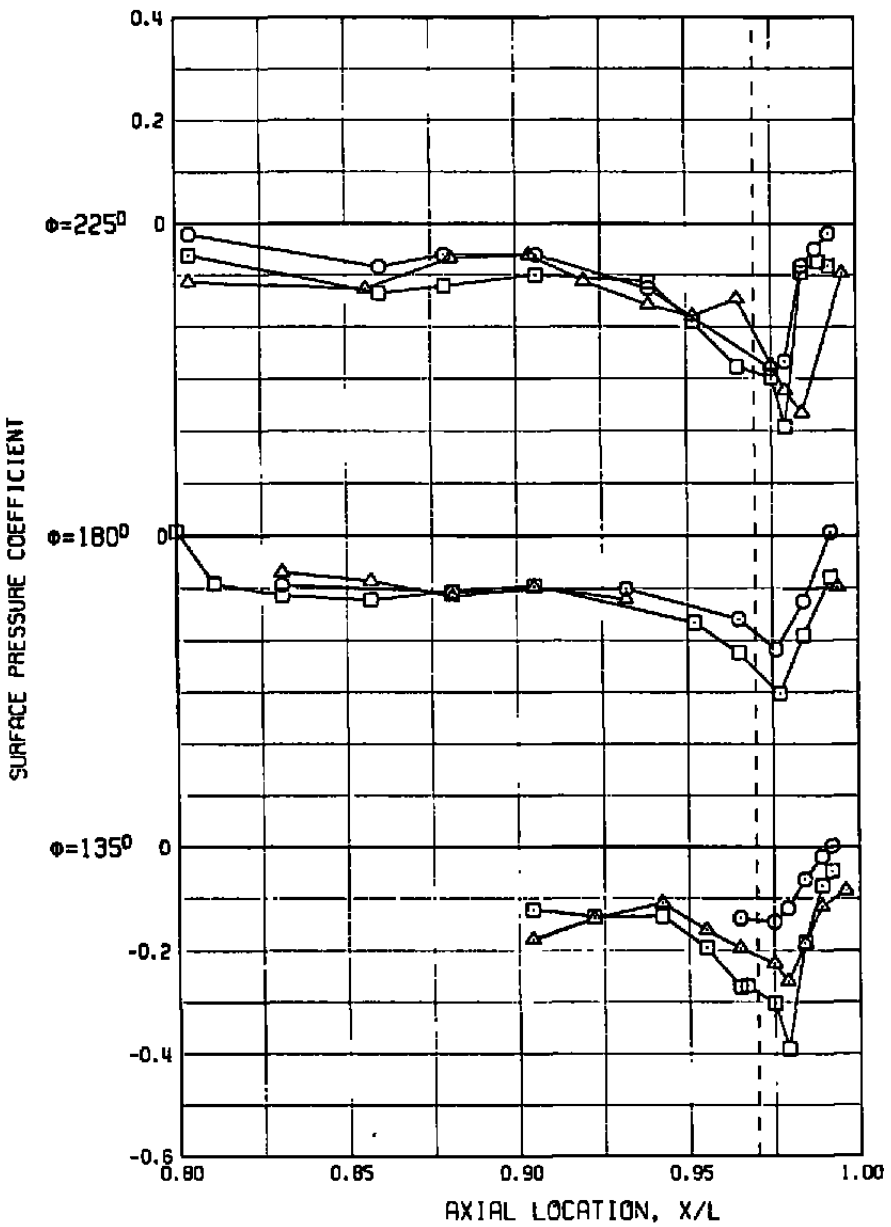

b. Windward-side pressures
Figure 40. Concluded.

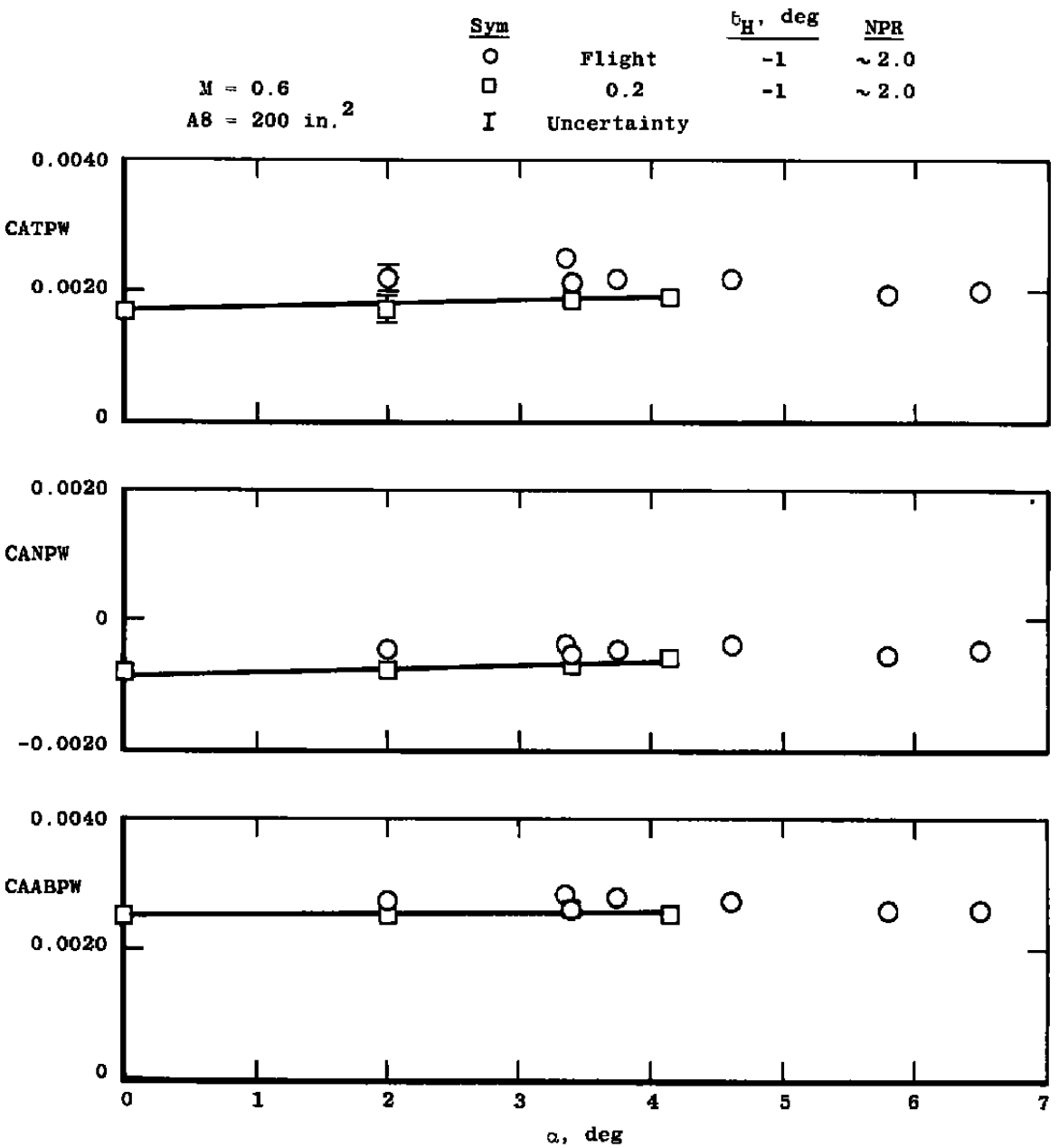

a. M = 0.6, A8 = 200 in.^{2}

Figure 41. Comparison of the integrated axial loads from the wind tunnel annular-jet model and the flight vehicle.

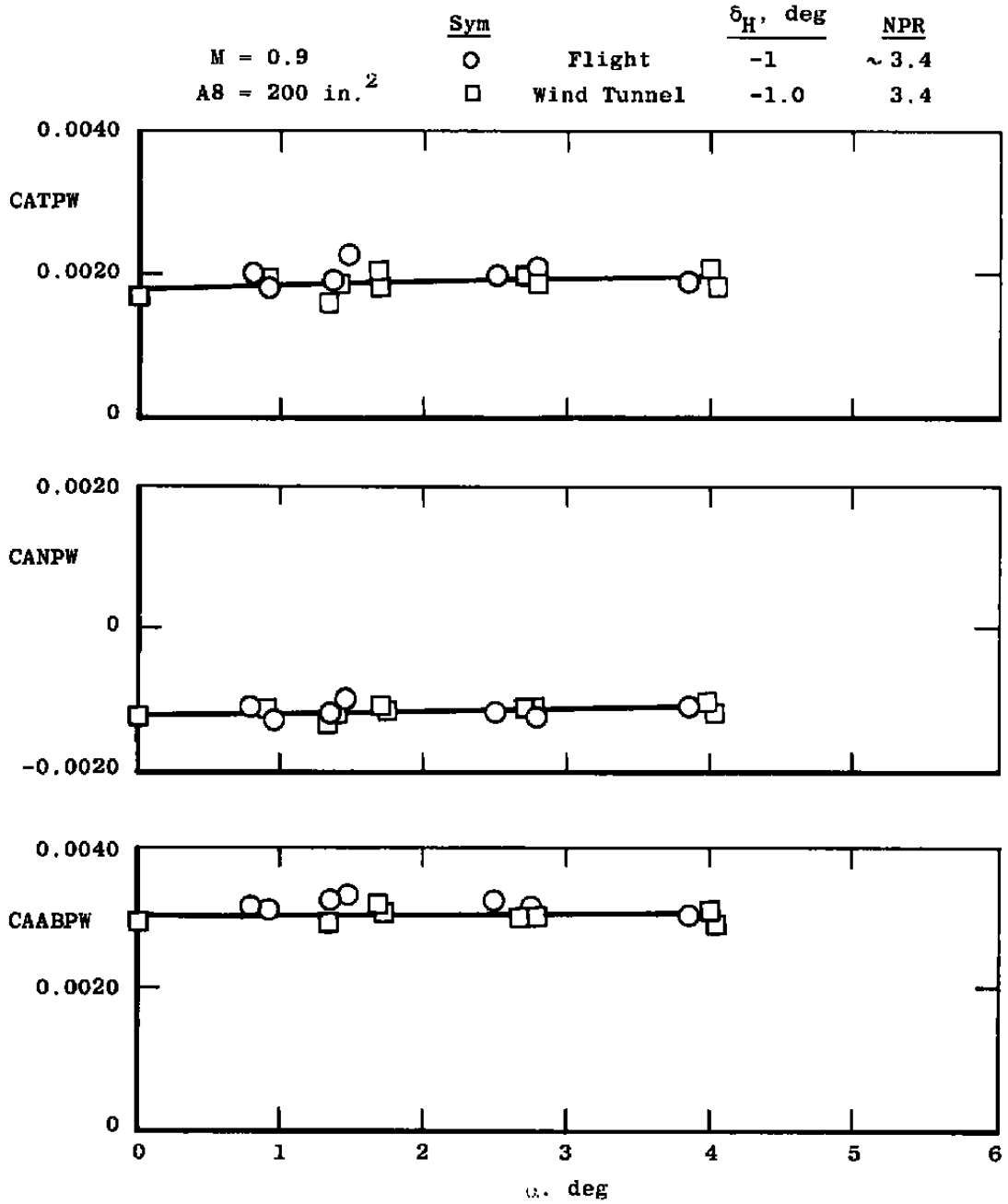

b. M = 0.9, A8 = 200 in.²
Figure 41. Continued.

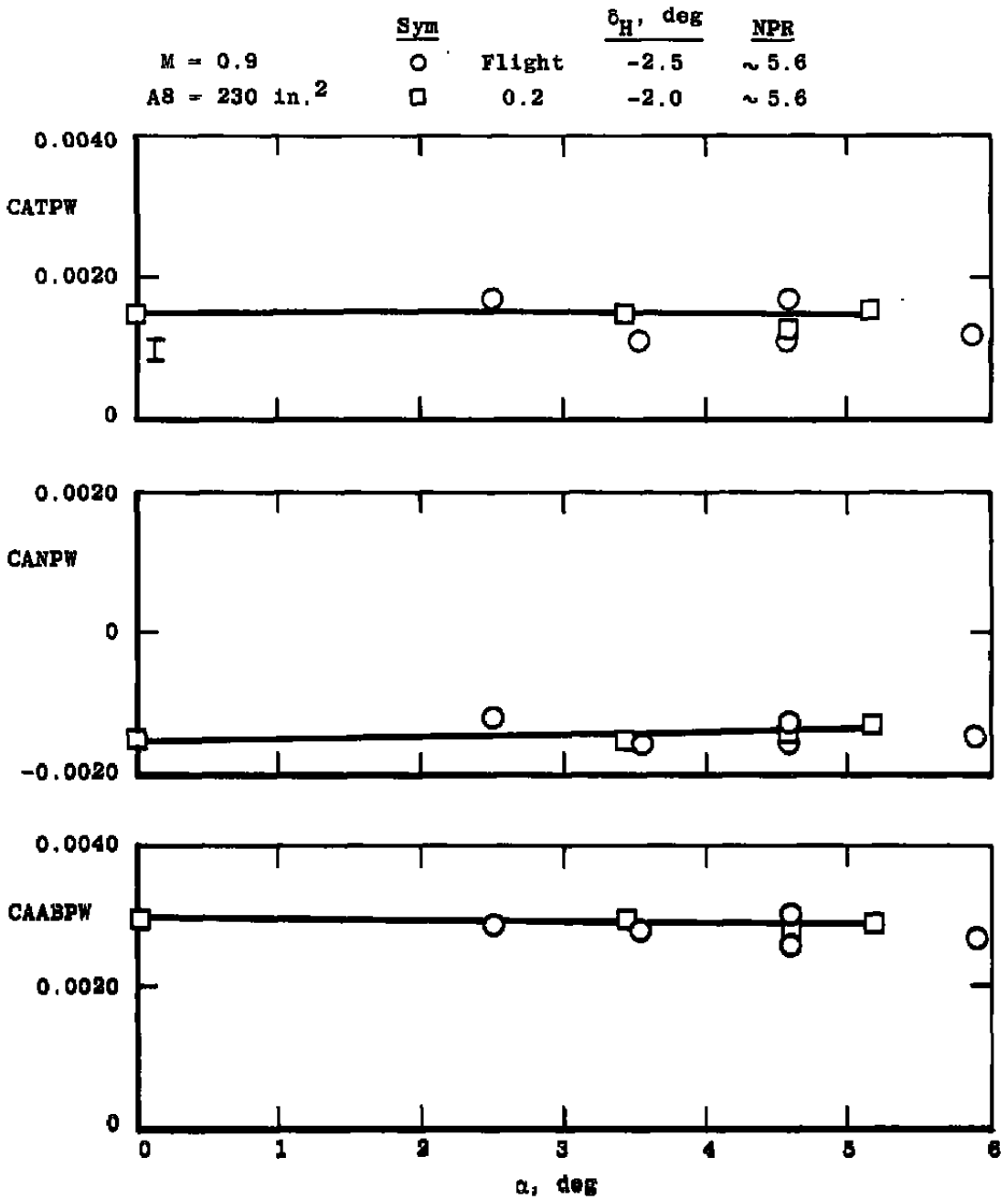

a. M = 0.9, A8 = 300 in.²
Figure 41. Continued.

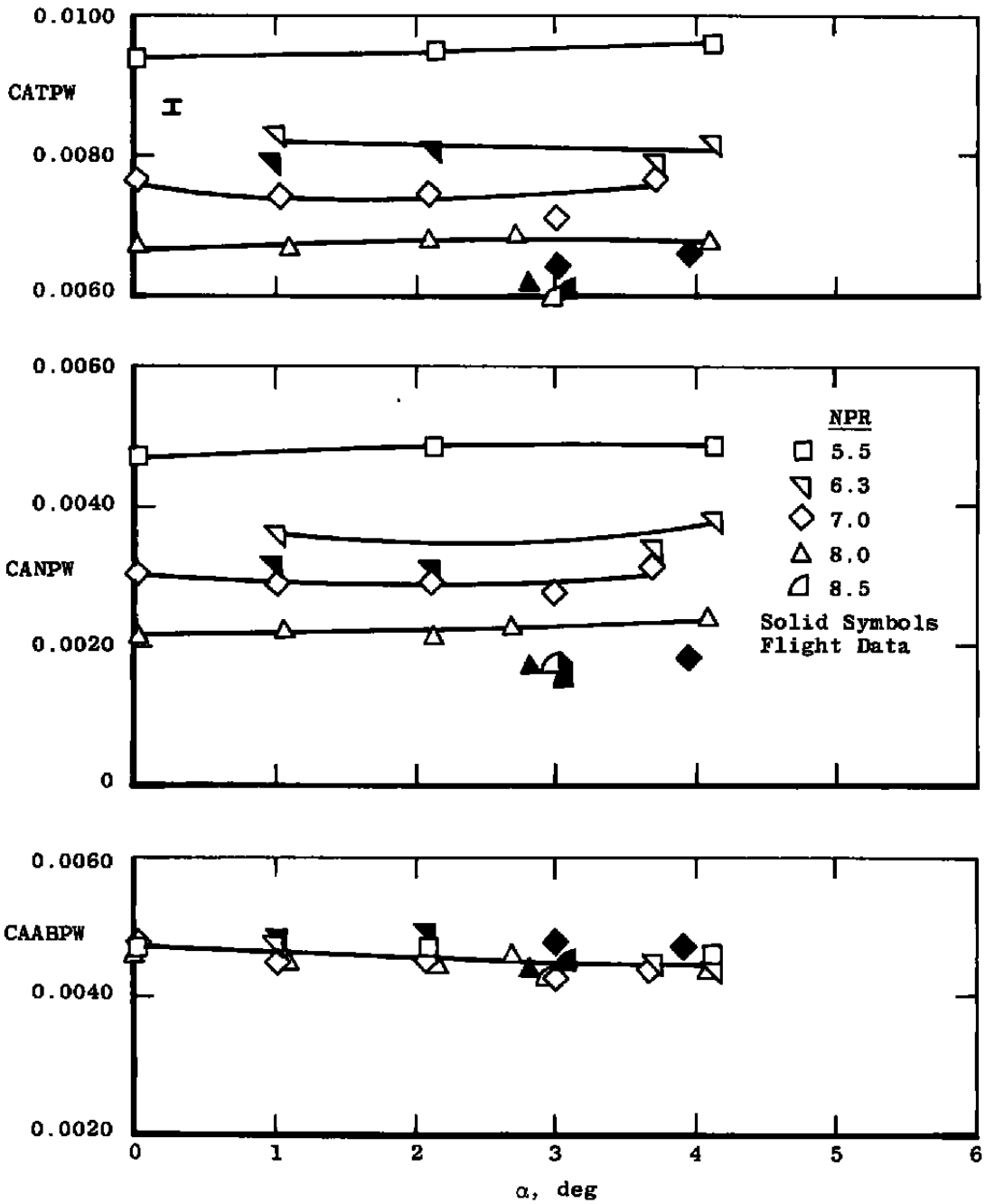

d. M = 1.2, A8 = 300 in.²
Figure 41. Concluded.

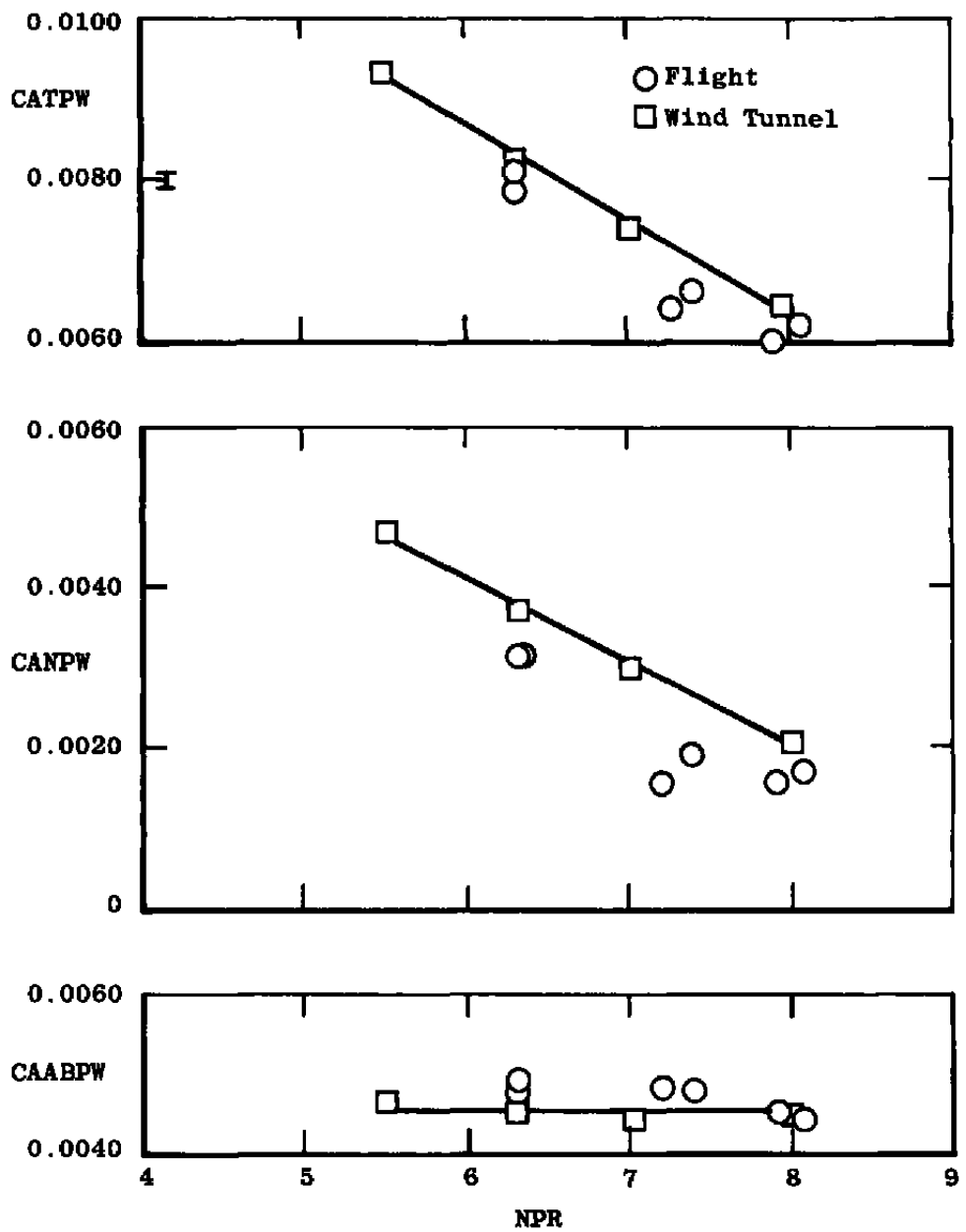

Figure 42. Effect of NPR on the comparison of annular-jet wind tunnel to flight data at M = 1.2, A8 ~ 300 in.^{2}, and α ~ 3 deg.

SYM	M	Re_ℓ	A8	NPR	α	δ_H	CATPW	SCALE
⊙	0.64	58.3	205.	3.7	6.5	-1.8	0.0021	0.1
⋇	0.60	25.6	200.	3.7	6.4	-1.8	0.0018	0.2

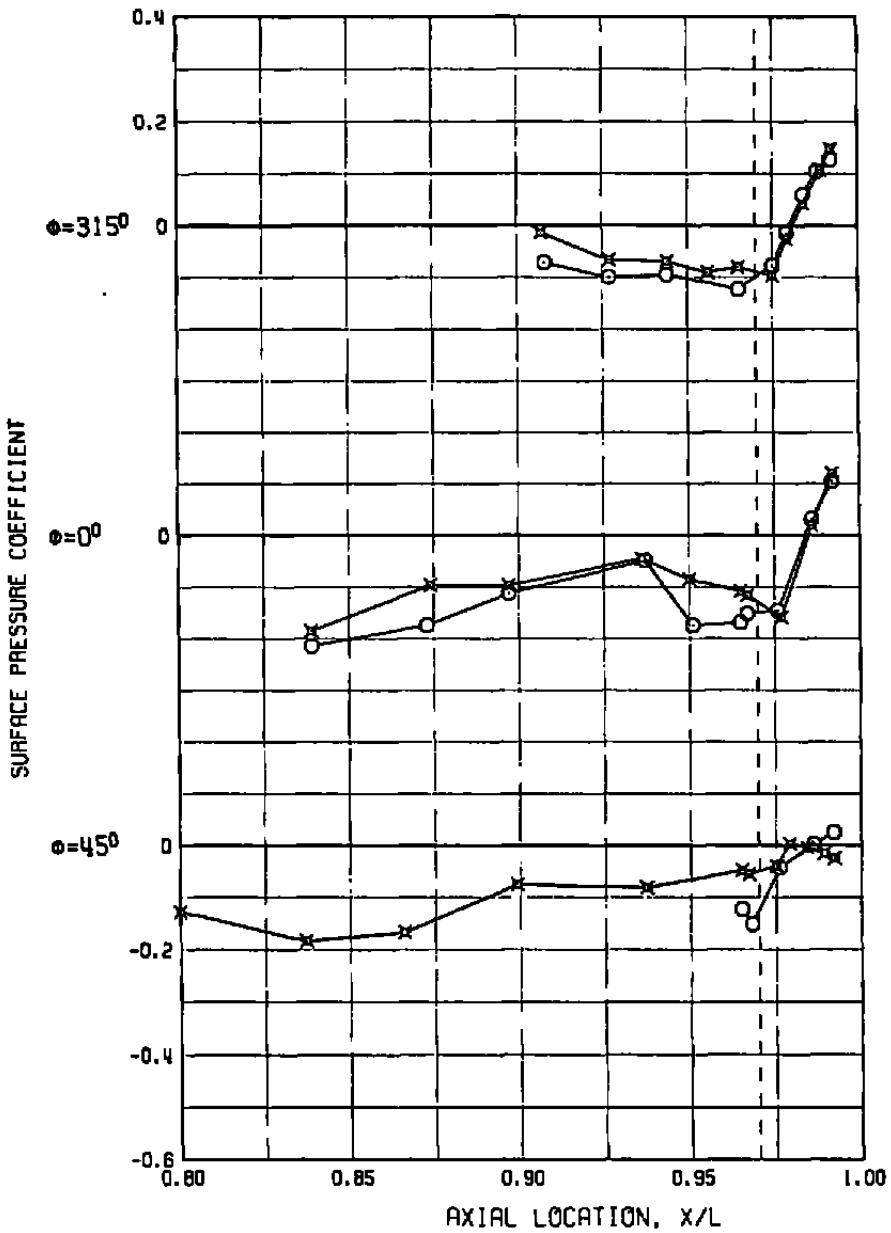

a. Lee-side pressures

Figure 43. Comparison of wind tunnel annular-jet and flight vehicle surface pressures distributions at M = 0.6, A8 = 200 in.², α ~ 6.5 deg, and NPR ~ 3.7.

SYM	M	Re_{ℓ}	AB	NPR	α	δ_H	CATPW	SCALE
○	0.64	58.3	205.	3.7	6.5	-1.8	0.0021	0.1
✕	0.60	25.6	200.	3.7	6.4	-1.8	0.0018	0.2

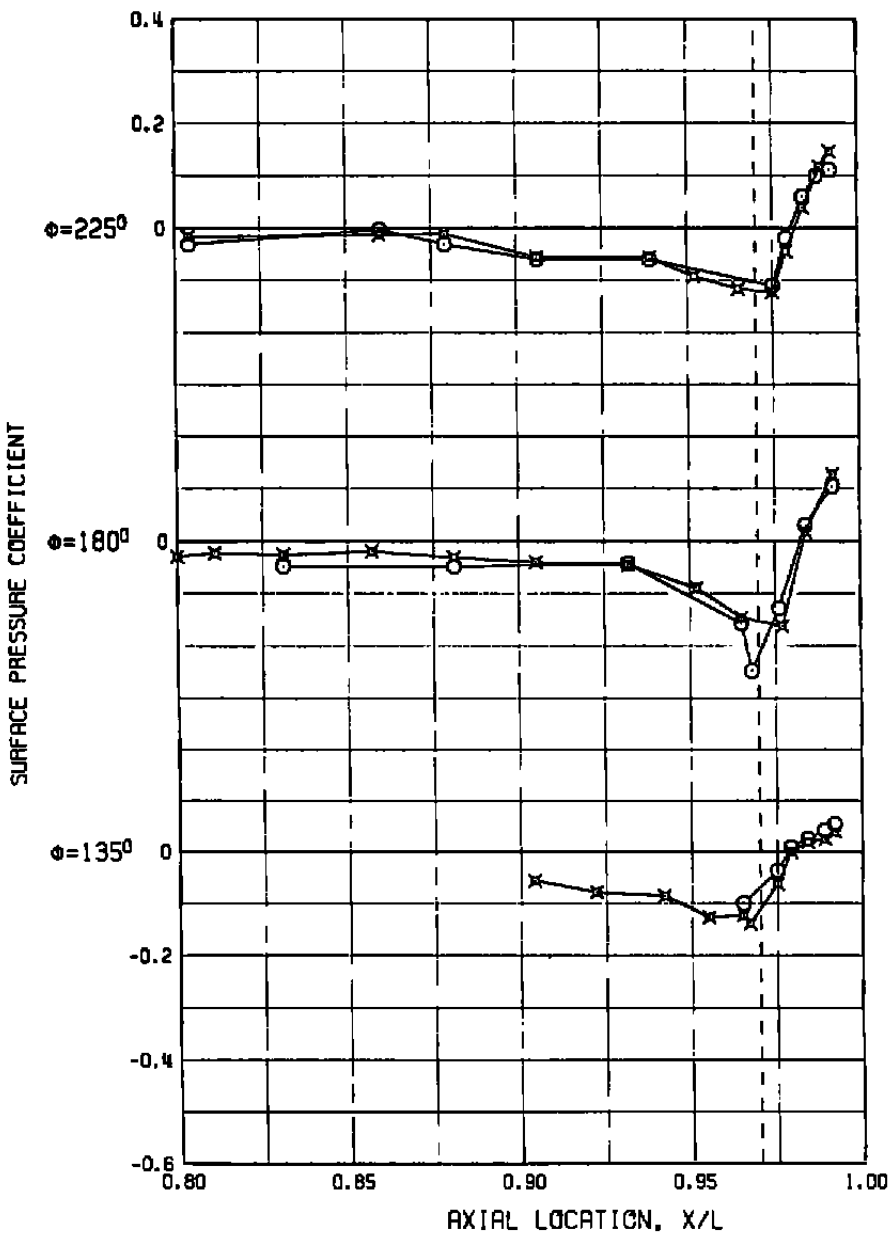

b. Windward-side pressures

Figure 43. Concluded.

SYM	M	Re_{ℓ}	A8	NPR	α	δ_H	CATPW	SCALE
O	0.90	55.6	225.	5.8	3.4	-2.2	0.0011	0.1
⌘	0.90	22.2	230.	5.6	3.4	-2.0	0.0015	0.2

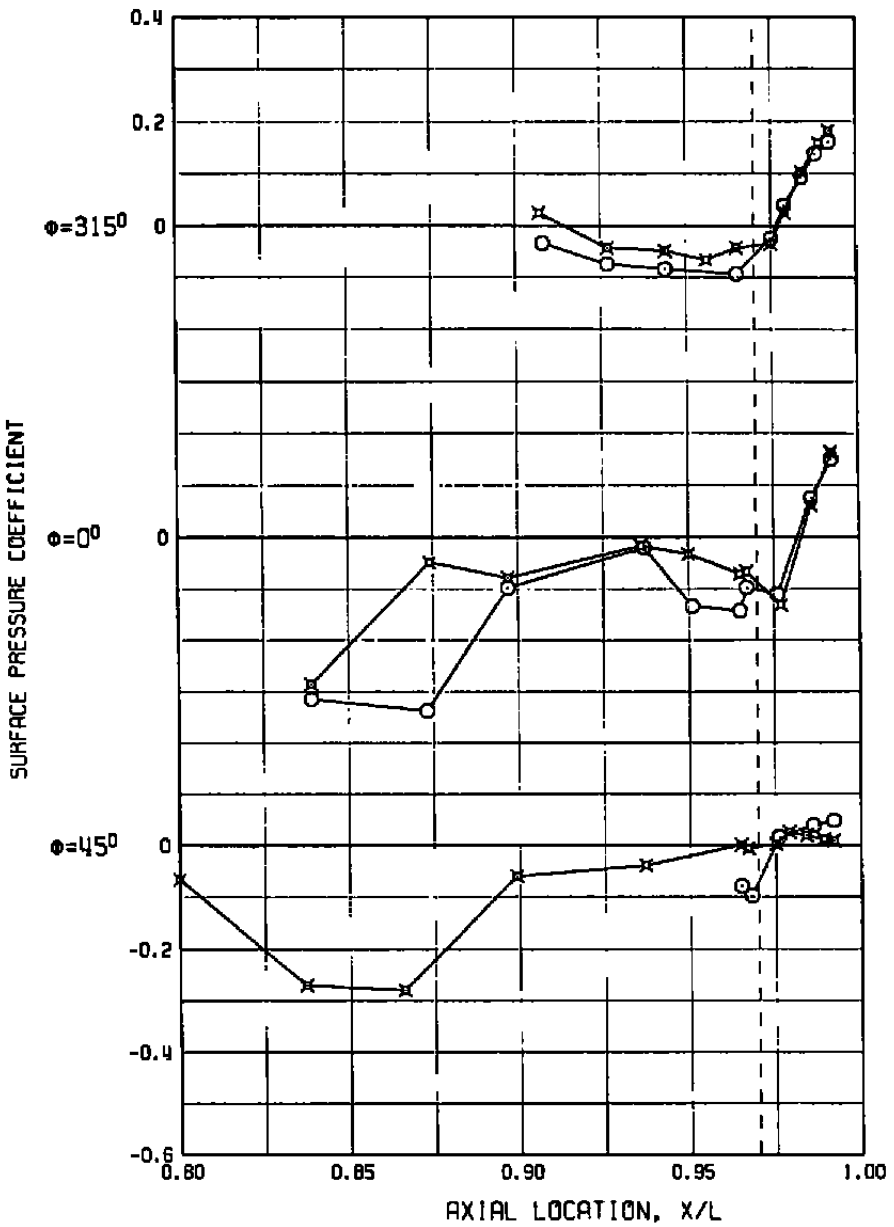

a. Lee-side pressures

Figure 44. Comparison of wind tunnel annular-jet and flight vehicle surface pressure distributions at M = 0.9, A8 = 230 in.², α = 3.4 deg, and NPR ~ 5.7.

SYM	M	Re_ℓ	RB	NPR	α	δ_H	CATPW	SCALE
⊙	0.90	55.6	225.	5.8	3.4	-2.2	0.0011	0.1
⋇	0.90	22.2	230.	5.6	3.4	-2.0	0.0015	0.2

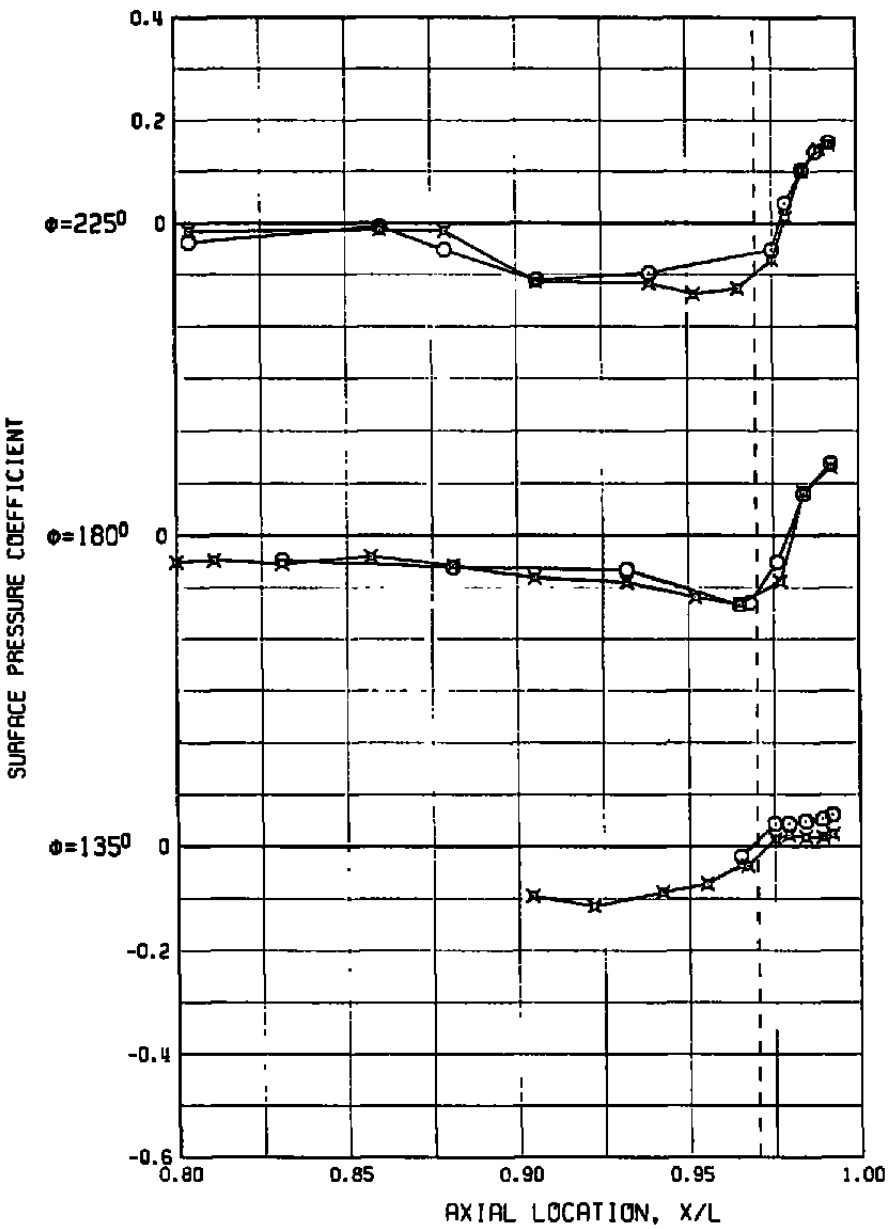

b. Windward-side pressures

Figure 44. Concluded.

SYM	M	Re_ℓ	A8	NPR	α	δ_H	CATPW	SCALE
⊙	1.24	63.6	302.	7.9	3.1	-3.3	0.0060	0.1
⋇	1.20	22.2	300.	8.2	3.0	-3.5	0.0060	0.2

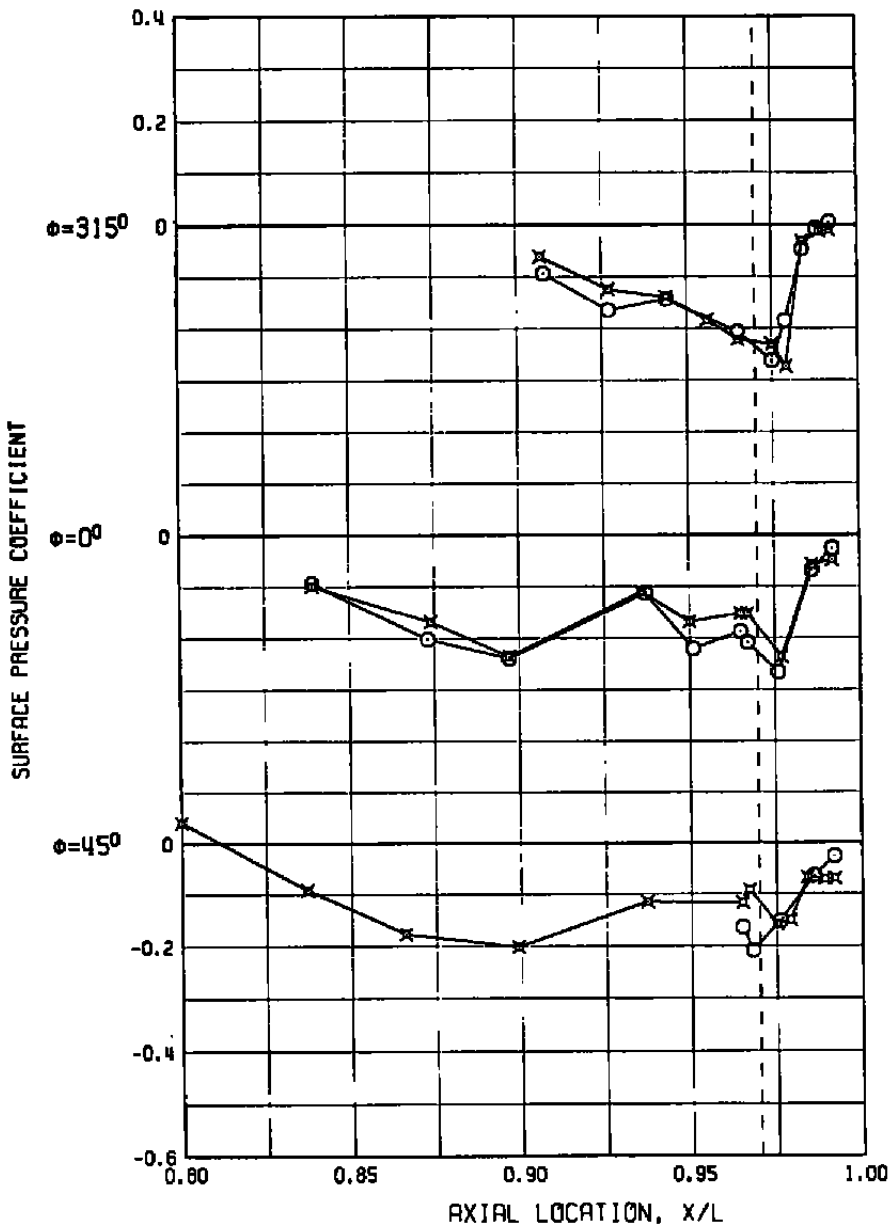

a. Lee-side pressures

Figure 45. Comparison of wind tunnel annular-jet and flight vehicle surface pressure distributions at M = 1.2, A8 = 300 in.², α = 3.0 deg, and NPR ~ 8.0.

SYM	M	Re_ℓ	AB	NPR	α	δ_H	CATPW	SCALE
⊙	1.24	63.6	302.	7.9	3.1	-3.3	0.0060	0.1
⊠	1.20	22.2	300.	8.2	3.0	-3.5	0.0060	0.2

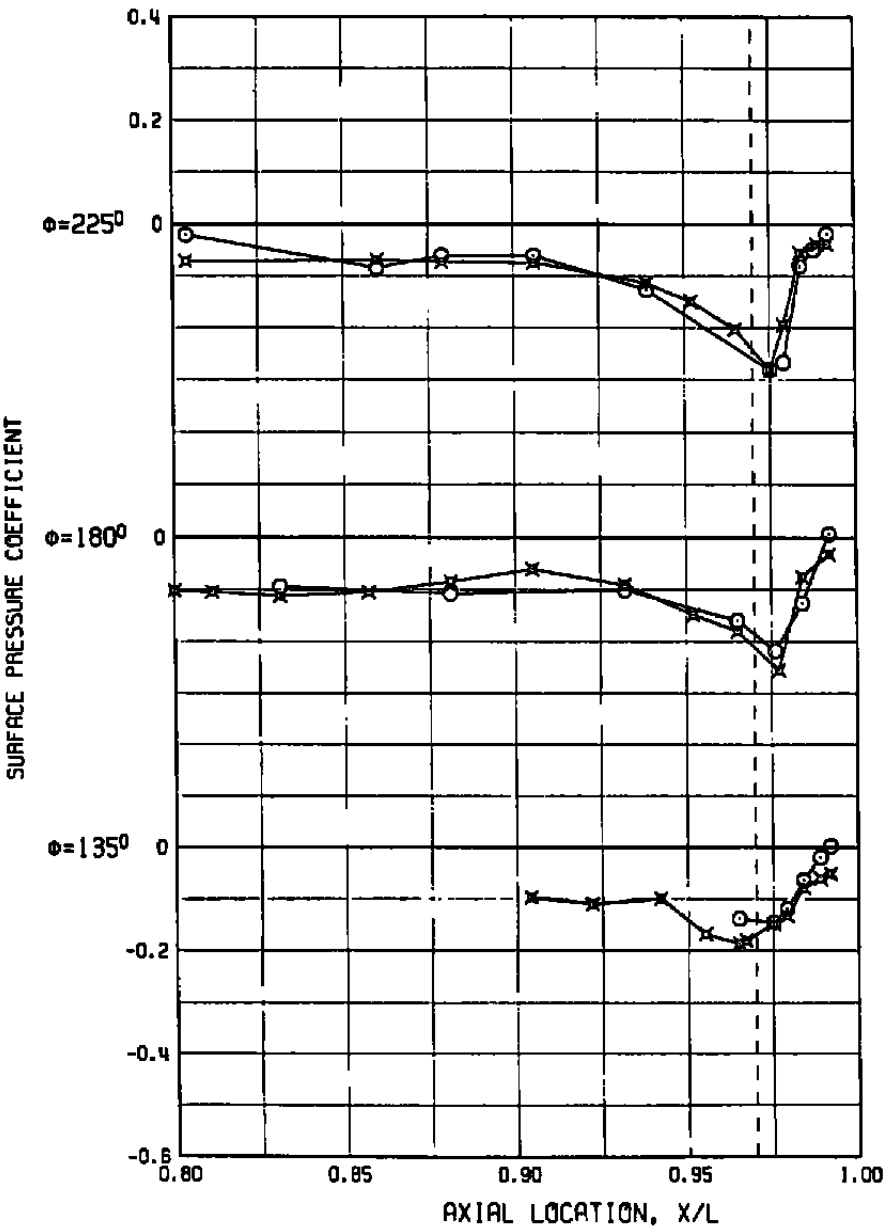

b. Windward-side pressures
Figure 45. Concluded.

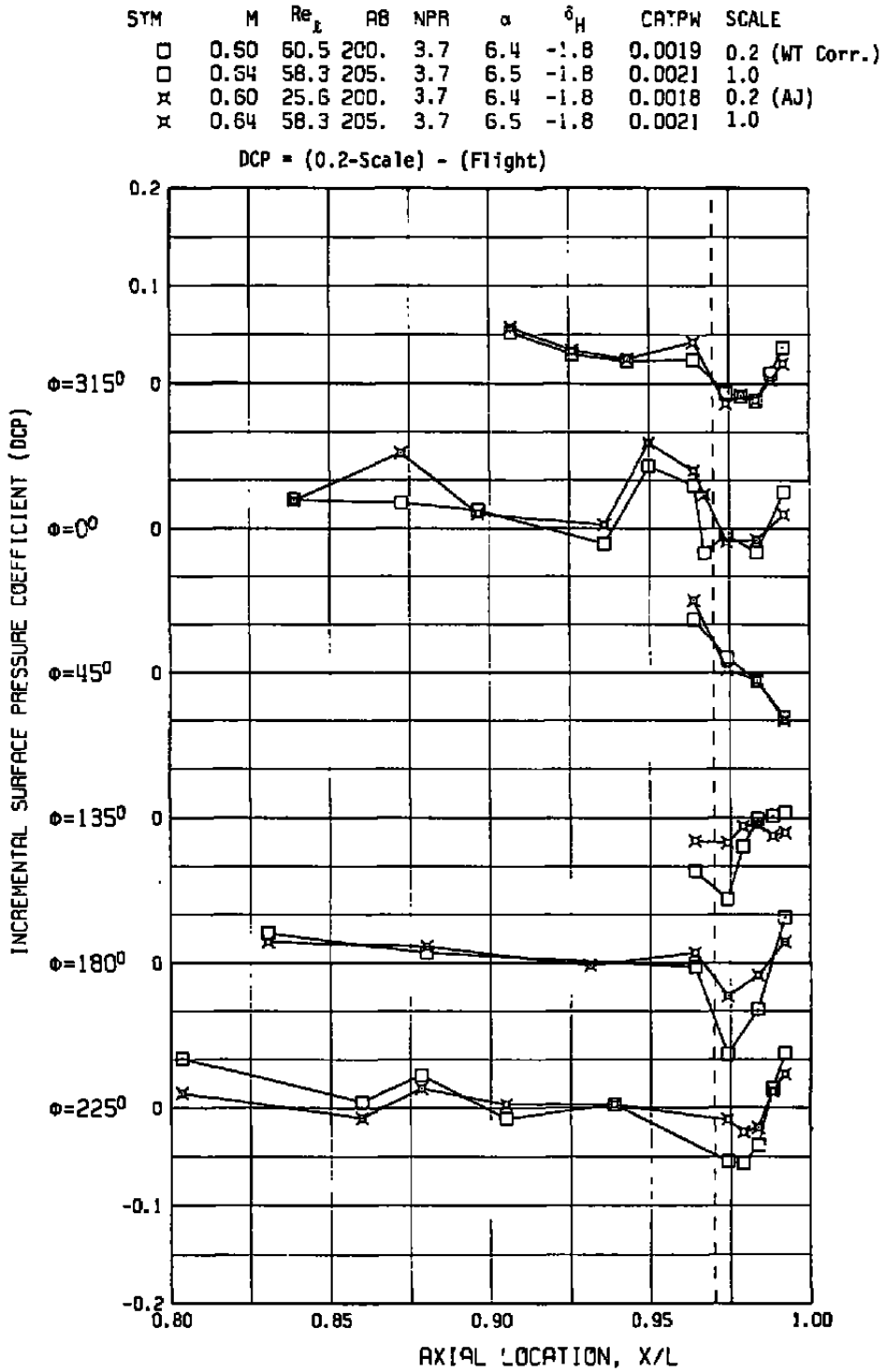

a. M = 0.6, $\alpha \sim 6.4$ deg, NPR = 3.7

Figure 46. Comparison of results from the annular- and corrected-full-jet simulations.

SYM	M	Re_ℓ	AB	NPR	α	δ_H	CATPW	SCALE
□	0.90	59.3	200.	3.4	2.5	-1.5	0.0016	0.2 (WT Corr.)
□	0.90	71.5	205.	3.8	2.8	-1.4	0.0019	1.0
⌘	0.90	22.2	200.	3.4	2.8	-1.5	0.0019	0.2 (AJ)
⌘	0.90	71.5	205.	3.8	2.8	-1.4	0.0019	1.0

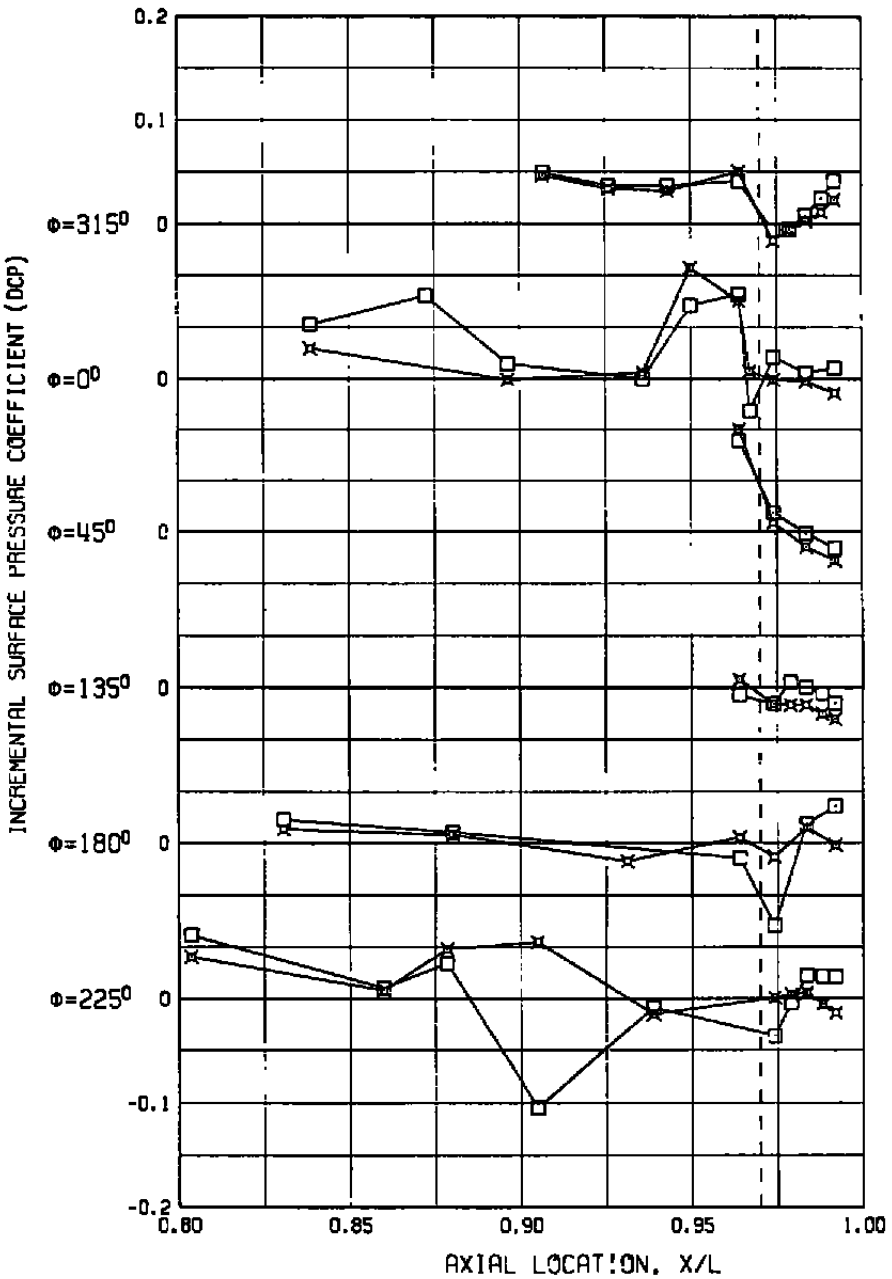

b. M = 0.9, α ~ 2.8 deg, NPR ~ 3.6
Figure 46. Continued.

SYM	M	Re_ℓ	AB	NPR	α	δ_H	CATPW	SCALE
□	1.20	29.6	300.	6.4	1.0	0.0	0.0091	0.2 (WT Corr.)
⊡	1.18	201.4	295.	6.3	0.9	0.1	0.0079	1.0
⋈	1.20	22.3	300.	6.3	1.0	0.0	0.0082	0.2 (AJ)
⋈	1.18	201.4	295.	6.3	0.9	0.1	0.0079	1.0

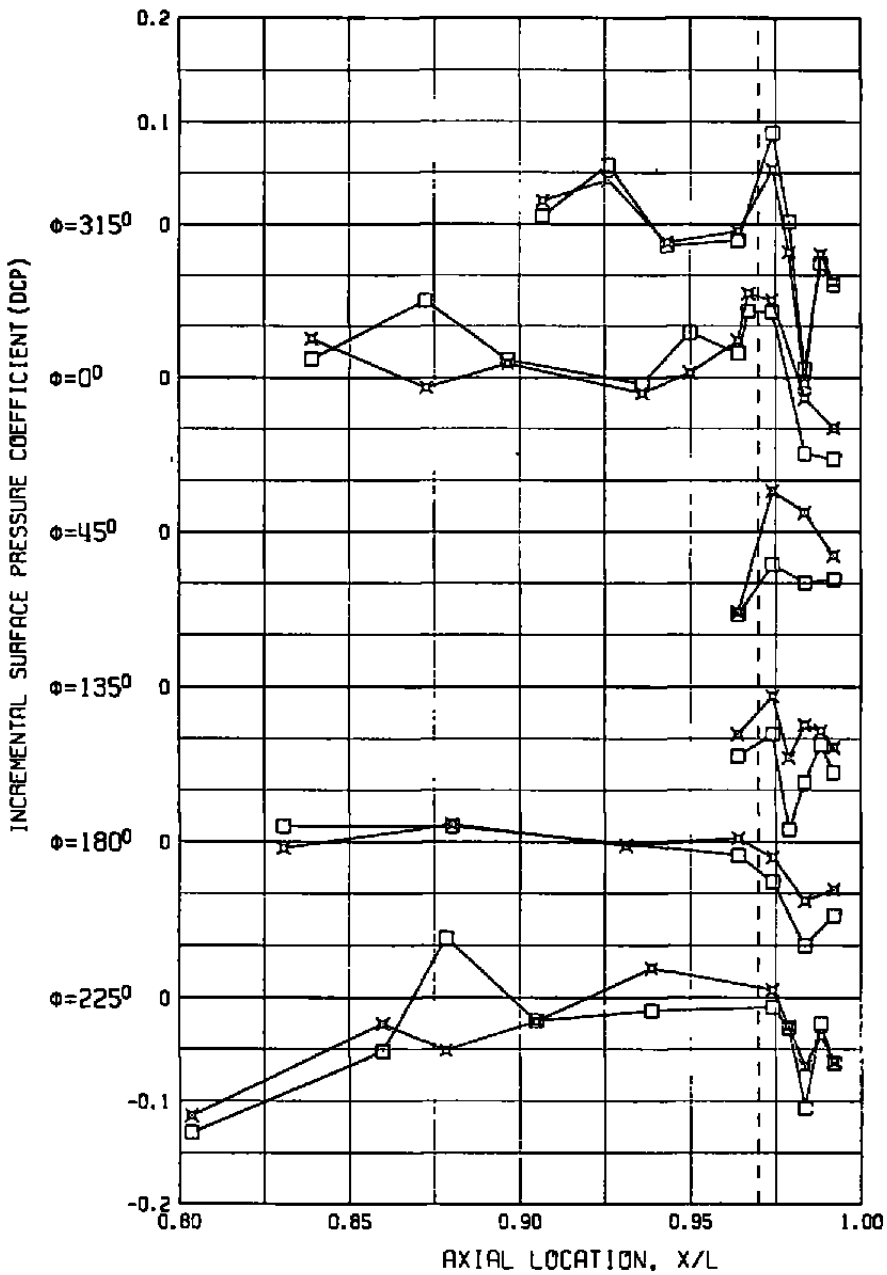

c. M = 1.2, $\alpha \sim 1$ deg, NPR ~ 6.3

Figure 46. Concluded.

Table 1. Flight Test Conditions

Data Point Number	M	H, ft	G	Q, lbf/ft^2	$Re_\ell \times 10^{-6}$	A8, in^2	NPR	α, deg	δ_H, deg
425	0.59	8,657	3.9	373.2	161.7	234	3.04	6.0	-2.3
452	0.60	7,261	3.1	409.3	164.3	204	2.17	4.6	-1.5
451	0.60	17,190	2.1	278.6	116.6	204	1.85	5.4	-2.0
450	0.60	33,197	1.0	138.4	58.3	204	2.70	5.8	-1.4
410	0.61	8,089	0.9	403.5	169.6	204	2.00	2.1	-0.5
408	0.61	24,974	0.9	207.2	106.0	205	2.00	3.4	-0.9
443	0.61	25,008	0.9	201.3	95.4	204	1.82	3.7	-1.3
437	0.61	39,868	0.9	100.9	55.7	205	2.92	8.3	-1.6
424	0.62	9,740	1.9	401.3	164.3	204	1.85	3.4	-1.1
423	0.62	25,035	1.7	207.6	108.7	205	2.51	6.6	-2.0
454	0.63	7,806	3.4	437.3	164.3	204	2.54	4.9	-2.7
439	0.64	39,793	1.0	111.9	55.7	204	3.25	6.8	-1.5
407	0.64	40,351	0.9	110.3	58.3	205	3.70	6.5	-1.8
401	0.81	19,762	1.0	450.5	161.7	205	2.55	1.5	-0.6
400	0.82	9,666	1.0	698.8	222.6	205	3.03	1.1	-0.8
417	0.88	25,234	3.9	418.2	153.7	224	5.16	4.6	-2.7
446	0.88	27,366	2.0	383.2	132.5	205	3.43	2.5	-1.5
442	0.89	49,716	1.3	137.1	55.7	235	5.63	5.9	-2.2
441	0.89	49,825	0.9	134.7	55.7	204	3.74	3.8	-1.6
413	0.90	10,495	1.0	809.5	243.8	205	3.10	0.8	-0.9
444	0.90	27,525	1.0	399.4	132.5	204	3.36	1.4	-0.9
402	0.90	27,997	0.9	391.9	132.5	205	3.13	1.5	-0.9
440	0.90	42,205	1.0	199.8	71.6	205	3.80	2.8	-1.4
422	0.90	48,702	1.2	146.6	55.7	229	5.71	4.6	-2.3
414	0.91	13,350	1.9	746.2	217.3	205	3.71	1.4	-1.6
409	0.91	18,138	1.0	606.7	190.8	204	3.20	0.9	-0.9
435	0.91	50,080	0.9	138.6	55.7	225	5.80	3.4	-2.2
458	0.92	10,500	4.1	839.0	235.9	233	4.02	2.0	-3.0
457	0.92	10,547	4.1	844.0	240.6	236	4.04	2.0	-2.9
415	0.92	12,935	3.9	775.6	233.2	233	4.23	2.5	-2.8
416	0.93	26,994	2.0	437.7	153.7	205	4.25	2.5	-2.2
403	0.93	41,921	0.9	213.7	71.6	205	4.17	2.6	-1.8
421	0.95	42,197	2.1	224.5	74.2	222	6.00	4.4	-3.0
405	0.96	49,727	1.2	156.7	58.3	220	6.06	4.6	-4.0
420	1.15	22,757	4.0	801.1	217.3	333	5.70	3.0	-4.7
432	1.17	30,458	1.0	585.1	164.3	275	6.62	1.5	-0.6
406	1.17	39,347	0.9	385.9	110.2	219	7.54	2.1	-1.6
418	1.18	25,940	0.9	736.3	201.4	295	6.28	0.9	0.1
431	1.18	41,091	2.1	364.2	108.7	308	7.41	3.7	-5.2
449	1.19	24,642	0.9	783.8	201.4	352	5.94	0.7	0.2
448	1.19	40,124	1.6	386.8	110.2	316	7.32	3.0	-3.9
419	1.20	25,790	2.1	764.6	190.8	296	6.34	2.1	-1.9
404	1.24	49,661	1.1	265.7	63.6	302	7.86	3.1	-3.3
436	1.25	49,891	1.0	266.3	66.3	302	8.04	2.8	-2.8

Table 2. 0.2-Scale Model Contours

	X/L = 0.967		X/L = 0.959		X/L = 0.946	
	-Y	+Z	-Y	+Z	-Y	+Z
1	6.550	-1.610	6.550	-2.085	7.050	-1.730
2	5.550	-2.757	5.550	-2.948	6.550	-2.557
3	4.550	-3.263	4.550	-3.389	5.550	-3.168
4	3.550	-3.425	3.550	-3.535	4.550	-3.540
5	3.400	-3.426	3.400	-3.541	3.550	-3.686
6	2.650	-3.334	2.650	-3.455	3.400	-3.684
7	1.650	-2.902	1.650	-3.045	2.650	-3.581
8	0.650	-1.920	0.650	-2.124	1.650	-3.174
9	0.150	-0.709	0.150	-1.253	0.650	-2.261
10	0.050	-0.628	0.050	-1.237	0.200	-1.703
11	0.000	-0.617	0.000	-1.218	0.000	-1.690
12	-0.050	-0.600	-0.050	-1.212	-0.200	-1.692
13	-0.150	-0.650	-0.150	-1.227	-0.650	-2.257
14	-0.650	-1.847	-0.650	-2.067	-1.650	-3.150
15	-1.650	-2.861	-1.650	-3.013	-2.650	-3.565
16	-2.650	-3.306	-2.650	-3.438	-3.550	-3.680
17	-3.550	-3.413	-3.550	-3.534	-4.550	-3.549
18	-4.550	-3.259	-4.550	-3.390	-5.550	-3.166
19	-5.550	-2.757	-5.550	-2.951	-6.550	-2.566
20	-6.550	-1.642	-6.550	-2.102	-7.050	-1.757
21	-6.950	-0.172	-7.075	-0.210	-7.200	-0.250
22	-5.156	-3.000	-5.464	-3.000	-5.932	-3.000
23	-5.871	-2.500	-6.194	-2.500	-6.611	-2.500
24	-6.326	-2.000	-6.626	-2.000	-6.950	-2.000
25	-6.622	-1.500	-6.863	-1.500	-7.133	-1.500
26	-6.802	-1.000	-7.018	-1.000	-7.186	-1.000
27	-6.909	-0.500	-7.078	-0.500	-7.195	-0.500
28	-6.941	0.000	-7.088	0.000	-7.193	0.000
29	-6.913	0.500	-7.055	0.500	-7.173	0.500
30	-6.808	1.000	-6.962	1.000	-7.108	1.000
31	-6.618	1.500	-6.791	1.500	-6.975	1.500
32	-6.329	2.000	-6.520	2.000	-6.752	2.000
33	-5.898	2.500	-6.132	2.500	-6.423	2.500
34	-5.235	3.000	-5.540	-3.000	-5.910	3.000
35	5.190	-3.000	---	---	5.970	-3.000
36	5.885	-2.500	5.489	-3.000	6.613	-2.500
37	6.319	-2.000	6.204	-2.500	6.944	-2.000
38	6.606	-1.500	6.618	-2.000	7.116	-1.500
39	6.781	-1.000	6.864	-1.500	7.164	-1.000
40	6.885	-0.500	6.999	-1.000	7.168	-0.500
41	6.911	0.000	7.052	-0.500	7.157	0.000
42	6.878	0.500	7.059	0.000	7.131	0.500
43	6.763	1.000	7.017	0.500	7.063	1.000
44	6.569	1.500	6.919	1.000	6.925	1.500
45	6.271	2.000	6.742	1.500	6.696	2.000
46	5.832	2.500	6.456	2.000	6.360	2.500
47	5.166	3.000	6.058	2.500	5.844	3.000
48	---	---	5.466	3.000	---	---

Table 2. Continued

	X/L = 0.928		X/L = 0.907		X/L = 0.872	
	-Y	+Z	-Y	+Z	-Y	+Z
1	7.050	-2.507	7.050	-3.038	6.950	-3.644
2	6.550	-3.039	6.550	-3.425	6.550	-3.735
3	5.550	3.414	5.550	-3.674	5.550	-3.911
4	4.550	-3.681	4.550	-3.840	4.550	-4.069
5	3.550	-3.796	3.550	-3.937	3.550	-4.146
6	3.400	-3.796	3.400	-3.937	3.400	-4.146
7	2.650	-3.703	2.650	-3.847	2.650	-4.059
8	1.650	-3.307	1.650	-3.466	1.650	-3.692
9	0.650	-2.443	0.650	-2.652	0.950	-3.202
10	0.400	-2.184	0.550	-2.602	0.450	-3.168
11	0.000	-2.151	0.000	-2.592	0.225	-3.498
12	-0.400	-2.171	-0.550	-2.594	0.000	-3.568
13	-0.650	-2.435	-0.650	-2.632	-0.225	-3.527
14	-6.650	-3.315	-1.650	-3.448	-0.500	-3.162
15	-2.650	-3.687	-2.650	-3.836	-0.950	-3.198
16	-3.550	-3.786	-3.550	-3.928	-1.650	-3.677
17	-4.550	-3.674	-4.550	-3.831	-2.650	-4.050
18	-5.550	-3.405	-5.550	-3.664	-3.550	-4.138
19	-6.550	-3.037	-6.550	-3.413	-4.550	-4.060
20	-7.050	-2.516	-7.050	-3.034	-5.550	-3.905
21	-7.330	-0.301	-7.435	-0.265	-6.550	-3.712
22	-6.598	-3.000	-6.355	-3.500	-6.950	-3.633
23	-7.060	-2.500	-7.078	-3.000	---	---
24	-7.262	-2.000	-7.357	-2.500	---	---
25	07.325	-1.500	-7.431	-2.000	---	---
26	-7.334	-1.000	-7.433	-1.500	---	---
27	-7.326	-0.500	---	-1.000	---	---
28	-7.320	0.000	---	-0.500	---	---
29	-7.311	0.500	---	0.000	---	---
30	-7.279	1.000	---	0.500	---	---
31	-7.184	1.500	---	1.000	---	---
32	-7.015	2.000	-7.348	1.520	---	---
33	-6.768	2.500	-7.257	2.000	---	---
34	-6.368	3.000	-7.092	2.500	---	---
35	---	---	-6.826	3.000	---	---
36	---	---	-6.371	3.500	---	---

Table 2. Concluded.

	X/L = 0.838		X/L = 0.803		X/L = 0.744	
	-Y	Z+	-Y	+Z	-y	+Z
1	6.750	-3.537	6.650	-3.361	7.050	-2.885
2	6.550	-3.616	6.550	-3.410	6.550	-3.237
3	5.550	-3.917	5.550	-3.882	5.550	-3.782
4	4.550	-4.191	4.550	-4.241	4.550	-4.093
5	3.550	-4.306	3.550	-4.365	3.550	-4.182
6	3.400	-4.308	3.400	-4.367	3.400	-4.181
7	2.650	-4.218	2.650	-4.291	2.650	-4.128
8	1.650	-3.868	1.650	-3.996	1.650	-4.032
9	1.100	-3.564	1.250	-3.813	1.400	-4.000
10	0.700	-3.556	0.850	-3.785	0.850	-3.994
11	0.350	-4.223	0.425	-4.789	0.425	-5.485
12	0.000	-4.330	0.000	-4.942	0.000	-5.771
13	-0.350	-4.229	-0.425	-4.763	-0.425	-5.480
14	-0.700	-3.552	-0.850	-3.771	-0.850	-3.998
15	-1.100	-3.568	-1.200	-3.792	-1.350	-3.996
16	-1.650	-3.866	-1.650	-3.988	-1.650	-4.030
17	-2.650	-4.210	-2.650	-4.276	-2.650	-4.146
18	-3.550	-4.296	-3.550	-4.345	-3.550	-4.179
19	-4.550	-4.177	-4.550	-4.221	-4.550	-4.079
20	-5.550	-3.895	-5.550	-3.870	-5.550	-3.771
21	-6.550	-3.587	-6.550	-2.379	-6.550	-3.211
22	-6.750	-3.521	-6.650	-3.335	-7.050	-2.860
23	-7.548	-2.900	-7.620	-2.620	-7.769	0.000
24	-7.697	-2.500	-7.669	-2.500	-7.766	0.500
25	-7.740	-2.000	-7.799	-2.000	-7.761	1.000
26	-7.740	-1.500	-7.805	-1.500	-7.748	1.500
27	-7.739	-1.000	-7.802	-1.000	-7.717	2.000
28	-7.736	-0.500	-7.798	-0.500	-7.668	2.500
29	-7.732	0.000	-7.791	0.000	-7.592	3.000
30	-7.726	0.500	-7.782	0.500	-7.465	3.500
31	-7.713	1.000	-7.771	1.000	-7.276	4.000
32	-7.695	1.500	-7.753	1.500	-7.004	4.500
33	-7.657	2.000	-7.717	2.000	-6.580	5.000
34	-7.590	2.500	-7.655	2.500	7.794	0.000
35	-7.492	3.000	-7.565	3.000	7.787	0.500
36	---	---	-7.429	3.500	7.773	1.000
37	-7.7332	3.500	-7.192	4.000	7.746	1.500
38	-7.063	4.000	-6.807	4.500	7.706	2.000
39	-6.581	4.500	---	---	7.647	2.500
40	---	---	---	---	7.558	3.000
41	---	---	---	---	7.429	3.500
42	---	---	---	---	7.250	4.000
43	---	---	---	---	6.993	4.500
44	---	---	---	---	6.585	5.000

Table 3. Flight Pressure Location and Integration Areas

Afterbody

X/L	θ, deg	A_i/S
0.964	77	0.05025
	∿ 2-in. LHS A/C	
0.927	Top C_L	---
0.964	"	0.1374
0.964	50	0.2637
0.839	0	0.1742
0.873	0	0.2035
0.896	0	0.2044
0.936	0	0.2081
0.950	0	0.1052
0.964	0	0.1418
0.964	315	0.17815
0.943	315	0.22935
0.926	315	0.3129
0.907	315	0.2969
0.964	292.5	0.1295
0.964	282	0.1876
0.964	252.8	0.1809
0.964	247.5	0.1459
0.804	225	0.43865
0.860	225	0.1799
0.878	225	0.2627
0.905	225	0.1132
0.939	225	0.51215
0.964	215	0.16745
0.831	180	0.76085
0.880	180	0.59965
0.931	180	0.63075
0.964	180	0.1709
	∿ 2-in. LHS A/C	
0.825	Bottom C_L	0.2808
0.909	"	0.3984
0.944	"	0.18775
0.964	135	0.2044
0.967	135	---
0.967	180	---
0.967	215	---
0.967	320	---
0.967	0	---
0.967	50	---

Nozzle

X/L	θ, deg	A_i/S
0.975	0	0.1977
0.985	0	0.29655
0.994	0	0.23065
0.985	22.5	0.0659
0.975	22.5	0.0659
0.975	45	0.16745
0.985	45	0.304275
0.994	45	0.293025
0.975	90	0.345975
0.994	90	0.345975
0.975	135	0.1362
0.978	135	0.1284
0.985	135	0.10995
0.988	135	0.19435
0.994	135	0.19585
0.985	157.5	0.09885
0.975	157.5	0.09885
0.975	180	0.1318
0.985	180	0.23065
0.994	180	0.2636
0.975	202.5	0.1318
0.975	182	0.1374
0.975	225	0.119725
0.978	225	0.177825
0.985	225	0.1373
0.988	225	0.32615
0.994	225	0.2288
0.975	315	0.152675
0.978	315	0.177825
0.985	315	0.2747
0.988	315	0.3591
0.994	315	0.2288

Table 4. Data Uncertainties

Wind Tunnel

M	$Re_{\ell} \times 10^{-6}$	P, psf	P_{avg}, psf	CATPW	UCP	UCATPW
0.60	14.9	701.4	713.9	0.0021	±0.02493	±0.00027
	29.6	1452.9	1487.4	0.0028	±0.01455	±0.00020
	59.6	2979.2	3029.7	0.0020	±0.00985	±0.00018
0.80	14.8	521.0	535.9	0.0019	±0.01809	±0.00018
	29.7	1046.3	1079.5	0.0021	±0.01033	±0.00013
	42.0	1478.4	1511.9	0.0015	±0.00817	±0.00011
0.90	14.8	445.7	455.9	0.0012	±0.01644	±0.00016
	29.7	891.1	928.5	0.0022	±0.00923	±0.00011
	58.8	1773.9	1841.6	0.0020	±0.00579	±0.00009
1.20	14.9	294.3	388.2	0.0094	±0.01378	±0.00013
	29.8	588.1	797.6	0.0105	±0.00757	±0.00008
	48.0	948.1	1359.9	0.0128	±0.00533	±0.00007

Flight

1-G Level Flight	UCP = ±0.01
Multi G Maneuver	UCP = ±0.02

APPENDIX A
LINEAR DATA INTERPOLATION SCHEME

Since most of the wind tunnel data were obtained before the flight test and wind tunnel testing provides matrix-type data, all parameters of the flight vehicle were not duplicated. In order to compare the wind tunnel and flight data, an interpolation scheme was devised to adjust the wind tunnel data to the flight conditions when there were significant differences. In most instances, there were enough wind tunnel data to bracket the flight conditions. The variation of the scale-model surface pressures as a function of α, NPR, and δ_H has been shown to be essentially linear in Refs. 4 and 5. It is assumed that the effect of these parameters is independent so that the superposition principle is applicable.

The interpolation matrix illustrated in Fig. A-1 was established with the following constraints:

$$\delta_{H_1} = \delta_{H_2} = \delta_{H_3} = \delta_{H_4} = \delta_{H_{13}}$$

$$NPR_1 = NPR_2$$

$$NPR_3 = NPR_4$$

$$\delta_{H_5} = \delta_{H_6} = \delta_{H_7} = \delta_{H_8} = \delta_{H_{14}}$$

$$NPR_5 = NPR_6$$

$$NPR_7 = NPR_8$$

The interpolation scheme initially operates on model attitude, α, at constant nozzle pressure ratio, NPR, horizontal tail angle, δ_H, model configuration, and Mach number as follows:

$$D(9,i) = \left[\left(C_{P_{i+1}} - C_{P_i} \right) \left(\frac{\alpha_F - \alpha_1}{\alpha_2 - \alpha_1} \right) + C_{P_i} \right]$$

likewise D(10,i), D(11,i), D(12,i) where i includes all the pressure orifices on the model.

The interpolation next calculates the nozzle pressure ratio correction using the values corrected for α:

$$D(13, i) = \left\{ \left[D(10, i) - D(9, i) \right] \left(\frac{NPR_F - NPR_1}{NPR_3 - NPR_1} \right) + D(9, i) \right\}$$

and likewise D(14,i).

Corrections were then applied for the off-condition horizontal tail setting:

$$D(15, i) = \left\{ \left[D(14, i) - D(13, i) \right] \left(\frac{\delta_{H_F} - \delta_{H_3}}{\delta_{H_7} - \delta_{H_3}} \right) + D(13, i) \right\}$$

where (D(15,i) is the corrected value of pressure coefficient $(C_{p_i})_c$ from the wind tunnel data to be compared to the flight data.

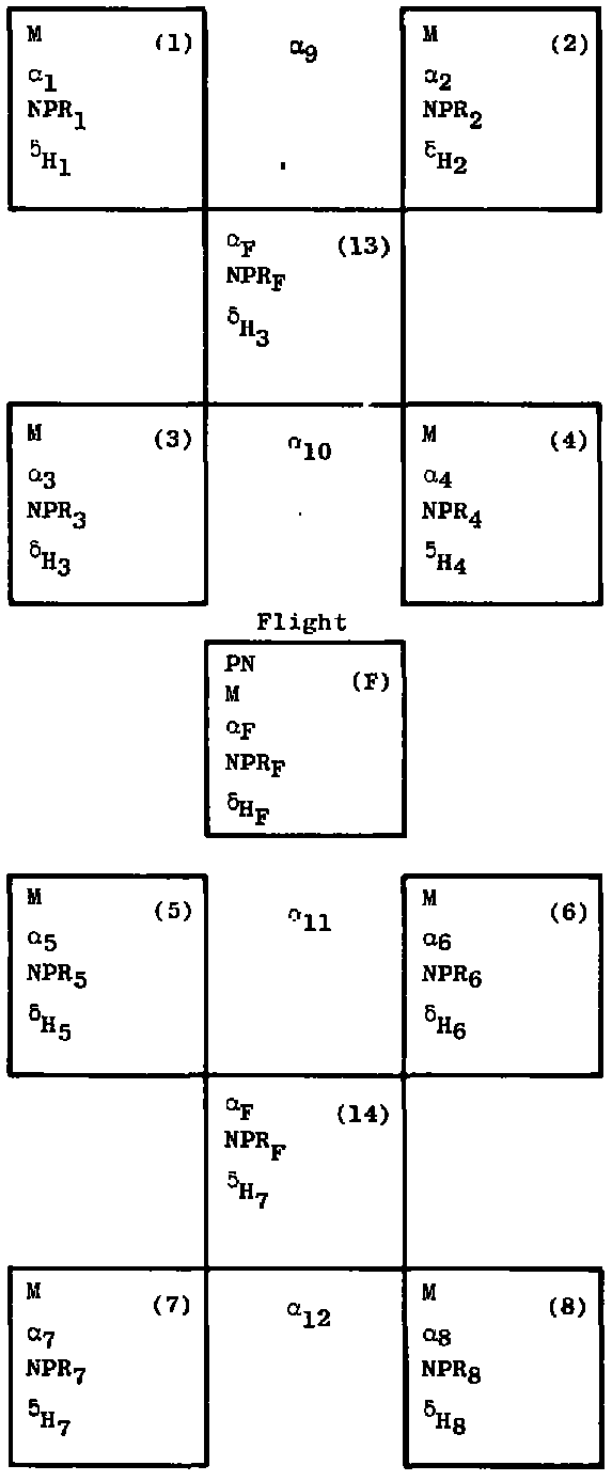

Figure A-1. Interpolation matrix.

NOMENCLATURE

A8	Full-scale nozzle throat area, in.^{2}
A_i	Incremental areas used in pressure integration, in.^{2}
AJ	Annular jet
CAABPW	Afterbody integrated-pressure axial-force coefficient, $\Sigma(C_{p_i}A_i)/S$
CATPW	Total aft-end (nozzle plus afterbody) integrated-pressure axial-force coefficient, CAABPW + CANPW
C_{p_i}	Surface pressure coefficient, $(P_i - P)/Q$
DCP	Pressure coefficient differences
F	Flight test conditions
FS	Model fuselage station, in. (see Figs. 1 and 2)
G	Aircraft load factor
H	Altitude, ft
L	Model length, 142.1 in.
ℓ	Body length, 126.6 in. (10.55 ft)
M	Free-stream Mach number
NPR	Nozzle pressure ratio (model nozzle total pressure/free-stream static pressure) or equivalent annular-jet nozzle pressure ratio (Ref. 10)
P	Free-stream static pressure, psfa
P_i	Model surface pressure, psfa
PT	Free-stream total pressure, psfa
Q	Free-stream dynamic pressure, psfa
Re	Free-stream unit Reynolds number, per foot
Re_ℓ	Characteristic Reynolds number based on body length
S	Wing + fuselage planform area (2,020 in.^{2})

TS	Wind tunnel station, in. (see Fig. 2c)
UCP_i	Uncertainty in surface pressure coefficient i
WT	Wing-tip support system
X	Model axial station, in.
Y	Lateral location of pressure orifice (see Table 2)
Z	Vertical location of pressure orifice (see Table 2)
α	Model angle of attack, deg
ΔCATPW	Incremental axial force
δ_H	Horizontal tail deflection angle, deg (positive leading edge up)
ϕ	Angular location of pressure orifice, deg (see Fig. 3)
Part Number	Data part number (a data subset containing variations of only one independent parameter)
Data Point	Data point number (a single record of all test parameters)
(i)	Indicates the wind tunnel condition being used in the interpolation scheme (Appendix A)